Ferrite Nanoparticles with Controlled Magnetic Properties for Their Applications to Magnetic Hyperthermia and Biotechnology

磁気特性を制御したフェライトナノ粒子の磁気ハイパーサーミアおよびバイオテクノロジー応用

July 2016

Shofu MATSUDA

松田　翔風

Ferrite Nanoparticles with Controlled Magnetic Properties for Their Applications to Magnetic Hyperthermia and Biotechnology

磁気特性を制御したフェライトナノ粒子の磁気ハイパーサーミアおよびバイオテクノロジー応用

July 2016

Waseda University

Graduate School of Advanced Science and Engineering

Department of Advanced Science and Engineering

Research on Applied Chemistry C

Shofu MATSUDA

松田　翔風

Referees: Prof. Toshiyuki Momma (Waseda University)
Prof. Toru Asahi (Waseda University)
Prof. Takayuki Homma (Waseda University)
Prof. Takuya Nakanishi (Waseda University)
Prof. Yoshinori Nishikitani (Waseda University)
Prof. Tetsuya Osaka (Waseda University)
Prof. Kazuaki Utsumi (Waseda University)

Contents

Contents

Contents

Chapter 1

General Introduction

1.1 What is nanoparticle?

Nanoparticles are generally defined as particles with a diameter of 1-100 nm [1-3]. Ultrafine particles with a diameter of 1-10 nm has received attention in the state-of-the-art technology. As shown in Fig. 1.1, the size of a nanoparticle are smaller than a virus but larger than a DNA. Considering the atomic radius, the number of atoms constituting a nanoparticle is very small. Hence the properties of nanoparticles are different from those of their bulk materials [4,5]. The surface area to volume ratio of particles, or the ratio of the number of surface atoms to the total number of atoms in a particle, increases if the particle size becomes smaller, which causes high reactivity (or high catalytic activity) of nanoparticles. In addition, the electronic energy levels become discrete in nanoparticles due to the small number of atoms, which is known as quantum confinement or quantum size effect, leading to unique electronic and optical properties observed in metal or semiconductor nanoparticles. Magnetic properties of nanoparticles are known to change by their size such as superparamagnetism and ferromagnetism.

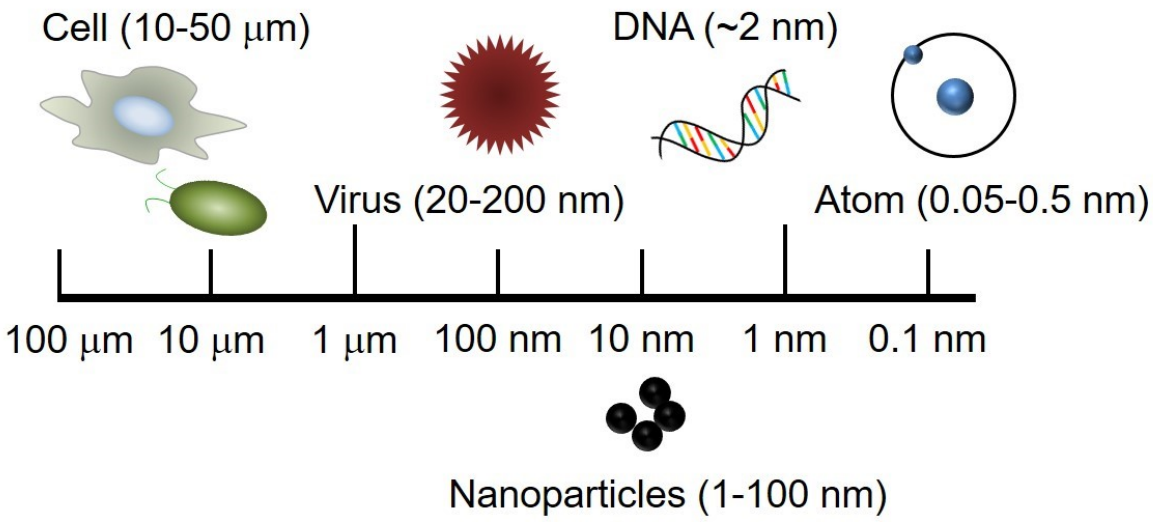

Fig. 1.1 Size of nanoparticles as compared to a cell, virus, DNA, and atom.

1.2 Ferrite nanoparticle

Ferrite means the oxides containing ferric ion Fe^{3+}, but ferrite is generally known as the magnetic oxides with a spinel structure [6]. Its chemical formula is represented as $MO{\cdot}Fe_2O_3$, where *M* is metal such as Mn, Fe, Co, Ni, Cu, Zn, Mg, etc., or their mixture. In the spinel structure, there are two crystallographic sites for *M*; the one is tetrahedrally coordinated with oxygen (A-site) and the other is octahedrally coordinated with oxygen (B-site). The unit lattice consists of eight A-sites and sixteen B-sites. When 8 A-sites are occupied by M^{2+} and 16 B-sites are occupied by Fe^{3+}, the compound is called a normal spinel type and described as $(M^{2+})_A[Fe^{3+}Fe^{3+}]_BO_4$. In the case that the A-sites are occupied by Fe^{3+} and the B-sites are occupied by M^{2+} and Fe^{3+}, the compound is called an inverse spinel type and described as $(Fe^{3+})_A[M^{2+}Fe^{3+}]_BO_4$ [6,7].

1.2.1 Magnetic property

The mechanism for appearance of magnetism in spinel ferrite nanoparticles is related to residual electrons having a spin magnetic moment in 3*d* orbital (unpaired electrons) in transition metal of Sc – Cu. The strength of magnetism, as proposed by Néel, is basically determined by two events as follows [6,7].

(i) The occupation of the tetrahedral A- and octahedral B-sites by transition metal cations (M^{2+} and Fe^{3+}).

(ii) The orientation of the magnetic moment of cations in A- and B-sites involved with interactions between magnetic cations in those sites, namely, A–B, A–A, and B–B interactions.

The strength of magnetism (the amount of magnetic moment per unit cell whose lattice constant is approximately 8.4 Å) can be estimated using a spin magnetic moment of an electron as 1 M_B of Bohr magneton, in consideration of antiparallel orientation between the magnetic moments of cations in the A-sites and those of cations in the B-sites. For example, the values of Fe_3O_4, $MnFe_2O_4$, and $NiFe_2O_4$ are calculated to be 32 M_B, 40 M_B, and 16 M_B, respectively, under

a condition of inverse spinel structure. These values are approximately consistent with their experimental values (32.8 M_B, 36.4 M_B, and 18.4 M_B for Fe_3O_4, $MnFe_2O_4$, and $NiFe_2O_4$, respectively) [8]. It should be noted that, for $CoFe_2O_4$, the experimental value of 31.5 M_B [8] is exceptionally higher than the value of 24 M_B estimated for inverse spinel from Hund's rule. This is derived from the residual orbital magnetic moment of Co^{2+} ion involved with its electronic configuration of d^7, which also causes high magnetic anisotropy in $CoFe_2O_4$ [9]. For $MgFe_2O_4$, the value depends on the distribution of Mg^{2+} ions between A- and B-sites. When all of Mg^{2+} ions occupy the B-site with half of Fe^{3+} ions to be $(Fe^{3+})_A[Mg^{2+}Fe^{3+}]_BO_4$, the magnetization of $MgFe_2O_4$ is calculated to be 0 M_B. With an increase in the ratio of Mg^{2+} occupying A-site, here denoted as δ, to a certain extent in the formula of $(Mg^{2+}{}_{\delta}Fe^{3+}{}_{1-\delta})_A[Mg^{2+}{}_{1-\delta}Fe^{3+}{}_{1+\delta}]_BO_4$, the magnetization also increases. At higher δ, the magnetization passes through a maximum value and decreases to zero. This is because the A–B interaction becomes weaker with a decrease in the number of magnetic Fe^{3+} ions being substituted by nonmagnetic Mg^{2+} ions in A-site, which causes antiparallel orientation of adjacent magnetic moments in B-sites by the B–B interaction [6].

The greatest characteristic of magnetic nanoparticles is the dependence of their magnetic properties on their diameter [7,10]. Fig. 1.2 shows the relationship between the coercivity and the diameter of nanoparticles. Small regions of uniform magnetization in magnetic materials are called magnetic domains. The magnetic-domain structure changes with the change of particle diameter. There are two states of magnetic domain structure; single- and multi-domain. Because magnetic domains have a critical or minimum size, the particles with a diameter smaller than that critical size consist of a single magnetic domain. The magnetization process of single-domain particles is the magnetization rotation type. The particles with rather large size have a multi-domain structure, in which magnetic domains are separated by domain walls. The magnetization process of multidomain particles is the domain wall motion type. Hence, magnetization reversal by domain wall motion does not occur in a particle with single-domain structure. Although the domain wall is easily moved by the applied magnetic field, stronger magnetic field is required to occur the magnetization rotation. Therefore, single-domain particles have a high coercivity. In the diameter range of single domain, the decrease in coercivity is observed as the particle size becomes smaller. This is because the influence of thermal disturbance is enhanced relatively. Then, the coercivity becomes zero, in which the orientation of magnetic moment is random. This state

is called superparamagnetic.

Fig. 1.2 also showed the example of the biomedical application of Fe_3O_4 and γ-Fe_2O_3 nanoparticles. For magnetic resonance imaging (MRI) and drug delivery system (DDS), superparamagnetic nanoparticles (with a diameter of <20 nm for Fe_3O_4 and γ-Fe_2O_3) are required or better because they are intravenously injected into human body. If ferri- or ferromagnetic nanoparticles are intravenously injected, there is a risk of forming a blood clot derived from their magnetic aggregation. Hence, many researches of superparamagnetic Fe_3O_4 and γ-Fe_2O_3 nanoparticles are reported for biomedical application. A word of "SPIONs" as an abbreviation of superparamagnetic iron oxide nanoparticles has been widely used in recent years. As a consequence, superparamagnetic γ-Fe_2O_3 nanoparticles has been clinically used as a MRI contrast agent: Feridex® and Resovist®. For hyperthermia, both superparamagnetic and ferromagnetic nanoparticles are suitable because magnetic nanoparticles are used as heat generators. Which magnetic property is more suitable for application to hyperthermia depends on the condition of applied AC magnetic field (the strength of magnetic field and the frequency). On the other hand, for cell separation, ferromagnetic nanoparticles are required because its objective is to separate cells using magnetic force from the mixture of cells and other materials.

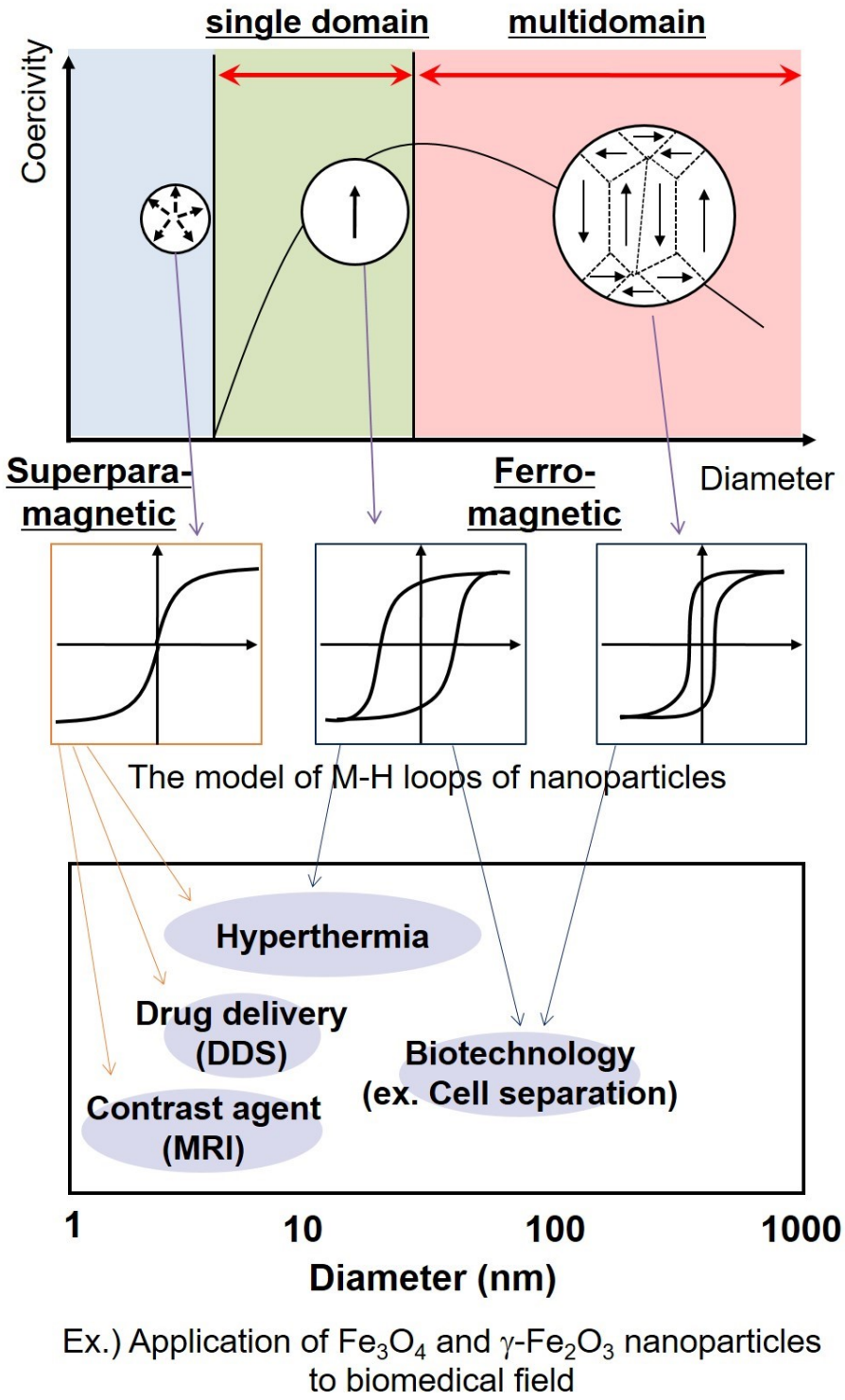

Fig. 1.2 The relationship between the coercivity (magnetic property) and the diameter of nanoparticles, with corresponding examples in biomedical application of Fe_3O_4 and γ-Fe_2O_3 nanoparticles.

1.2.2 Synthetic method

The synthesis method of nanoparticles can be divided into two types of technique roughly. One is the top-down method, and the other is the bottom-up method. In the top-down method, nanoparticles are synthesized by breaking large-sized particles but there is a lower limit of the particle size synthesized, while effective in mass production. On the other hand, in the bottom-up method, nanoparticles are formed from the nucleation and the nucleus growth. This method can produce nanoparticles with a diameter range from a few nm to several tens of nm. Additionally, it has an advantage of controlling the size and shape, hence the bottom-up method is preferable for the synthesis of nanoparticles generally. Here, two types of popular solution phase synthesis for ferrite nanoparticles are introduced below.

Co-precipitation method

In co-precipitation method, an aqueous solution containing a precipitation reagent is added to an aqueous solution of the mixture of metal (II) and (III) salts, then nanoparticles are obtained as precipitates. The formation of ferrite nanoparticles is progressed by the following reaction generally.

$$M^{2+} + 2Fe^{3+} + 8OH^{-} \rightarrow MFe_2O_4 + 4H_2O. \quad (1.1)$$

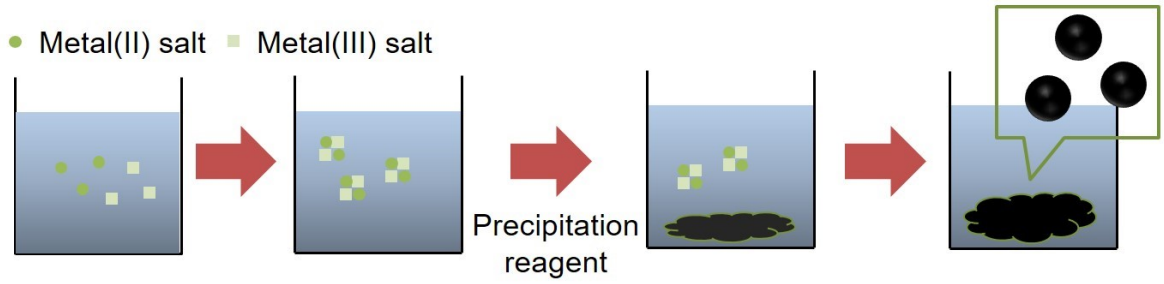

Fig. 1.3 Schematic diagram of co-precipitation method.

In this method, the size, shape, and composition of products are dependent on the concentration ratio of metal salts prepared first. The advantages of this method are following; (i) simple synthetic procedure and (ii) it can be synthesized in the atmosphere, while there is a disadvantage that the shape is difficult to control. For example, Fe_3O_4 nanoparticles were synthesized by the addition of an aqueous solution containing ammonia as a base into an aqueous solution of the mixture of $FeCl_2$ and $FeCl_3$ [11].

Thermal decomposition

In thermal decomposition, the organometallic salt is decomposed in the presence of a surfactant at a high temperature. The surfactant prevents the aggregation of metals. The organic solvent with a high boiling point is used because the decomposition occurs at very high temperature. The advantage of this synthetic method is to control the shape of particles easily with a uniform particle size, while there is a disadvantage of complex synthetic systems in an inert gas atmosphere with a high temperature reaction. For example, highly monodisperse Fe_3O_4 nanoparticles were obtained by the thermal decomposition of iron (III) acetylacetonate in phenyl ether solvent containing alcohol, oleic acid, and oleylamine at 265°C [12].

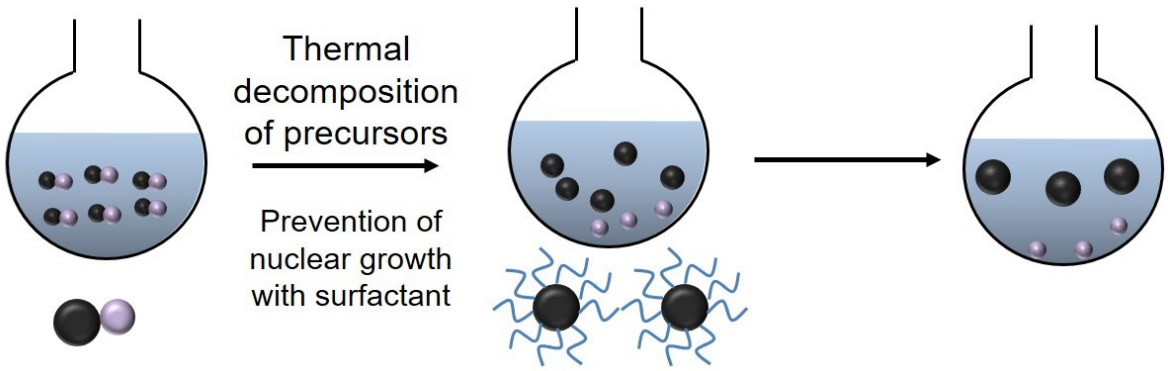

Fig. 1.4 Schematic diagram of thermal decomposition.

Considering the administration of nanoparticles synthesized into human body, those which

synthesized by co-precipitation method is more suitable for biomedical application because of its hydrophilic property and effective mass production. There is no concern of involving organic solvents.

1.2.3 Application to hyperthermia

Hyperthermia (thermotherapy), in which cancer cells are treated with heat of approximately 43°C [13-15], has recently received attentions as a fourth line of cancer therapy following surgical resection, chemotherapy, and radiation therapy. There are three very important advantages for hyperthermia: (1) it can be effectively applied to all types of cancer cells, (2) it is non-invasive, and (3) it has very few side effects. For example, the Thermotron RF-8 system (Yamamoto Vinita Co., Ltd., Osaka, Japan) has been clinically applied to kill cancer cells using heat derived from 8-MHz radio frequency (RF) irradiation [16,17]. However, achieving cancer cell-specific death is difficult in RF-induced hyperthermia because normal tissue is heated along with the cancerous tissue.

Recent investigations have focused on the biomedical applications of magnetic nanoparticles such as in drug delivery systems, magnetic resonance imaging, and magnetic hyperthermia [18-35]. In hyperthermia using magnetic nanoparticles and lower frequency (a few hundred kHz) magnetic field, just particles generate heat derived from their magnetic property. Hence, if the magnetic nanoparticles were to specifically accumulate within a tumor, cancer cells could be exclusively heated under an alternating magnetic field; this process is referred to as magnetic hyperthermia [18-20,24-28]. Iron oxides such as Fe_3O_4 or γ-Fe_2O_3 nanoparticles are generally used as heat generators as they have the advantages of high biocompatibility and relatively large magnetization.

Heating mechanism

The heating mechanism of magnetic nanoparticles under AC magnetic field is classified two types. First, superparamagnetic nanoparticles are well known to produce heat that is dependent on the amount of magnetic relaxation, consistent with the Néel and Brown relaxation theory, under an AC magnetic field [36-39], as shown in Fig. 1.5.

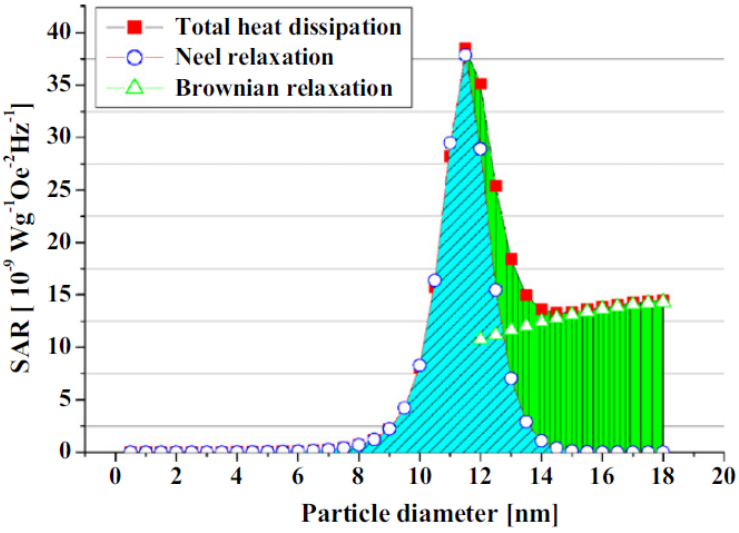

Fig. 1.5 Theoretical estimation of heating rates (total heat dissipated through Néel as well as Brownian relaxations) as a function of particle diameter. Surfactant layer thickness = 3.2 nm, anisotropy constant = 30 kJ m^{-3}, temperature = 300 K, viscosity = 0.00089 kg m^{-1} s^{-1}, applied AC magnetic field = 40 Oe and frequency = 600 kHz. Reprinted with permission from [39]. Copyright @ 2009 Elsevier B. V.

In contrast, when the ferromagnetic particles are placed under AC magnetic field, heat is generated by hysteresis loss [37,38]. For ferromagnetic nanoparticles, the amount of heat (hysteresis loss) is dependent on the hysteresis area in M-H loop of particles, as following a formula (1.2) [40].

$$\text{Area} = f \int MdH \tag{1.2}$$

Where f is frequency, M is magnetization, H is magnetic field applied.

In the latest researches, S. Ota et al. mentioned that the frequency showing highest heating efficacy of Fe_3O_4 nanoparticles was different for each concentration of particles, which suggested the involvement of dipole-dipole interaction in heat generation of nanoparticles [41].

Biocompatibility

Considering to the application of ferrite nanoparticles to hyperthermia (into human body) biocompatibility of particles is one of very significant factors. Hence, there are many reports and discussion. Of which, L. Moller et al. have carried out *in vitro* investigation of the cytotoxicity of several kinds of oxides nanoparticles in human lung adenocarcinoma epithelial A549 cells [42].

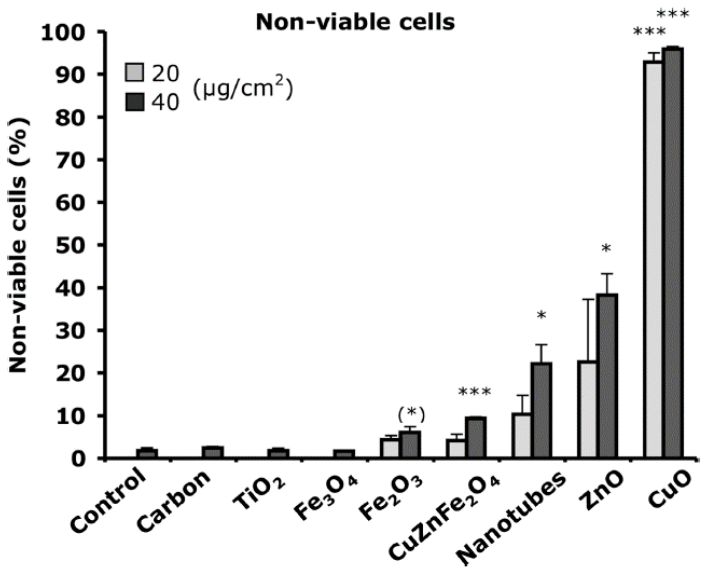

Fig. 1.6 Cytotoxicity in cultured A549 cells after exposure to 20 μg/cm^2 (40 μg/mL) and 40 μg/cm^2 (80 μg/mL) nanoparticles for 18 h, measured as percent nonviable cells by trypan blue staining. The asterisks (*, **, ***) indicate significantly higher levels compared to controls and correspond to $p < 0.05$, 0.01, 0.001, respectively. Reprinted with permission from [42]. Copyright 2008 American Chemical Society.

As shown in Fig.1.6, CuO and ZnO showed high level of cytotoxicity for A549 cells although, iron oxide nanoparticles showed much lower cytotoxicity, especially for Fe_3O_4 nanoparticles. Furthermore, the authors have also investigated the degree of DNA damage induced by the addition of nanoparticles, as evaluated by comet assay. As a result, TiO_2 showed the high level of

DNA damage but no cytotoxicity. On the other hand, Fe_3O_4 did not showed not only cytotoxicity but also induction of DNA damage in their condition, which is suggestive of high biocompatibility of Fe_3O_4 nanoparticles [42].

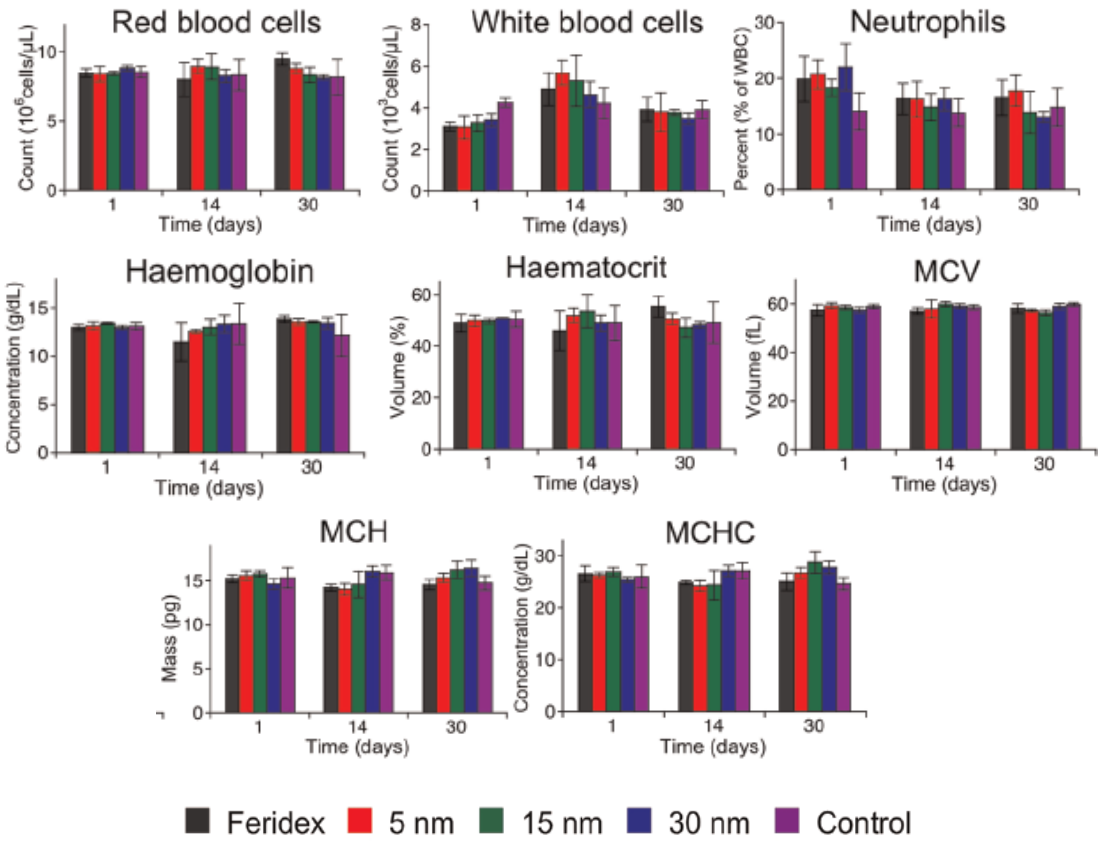

Fig. 1.7 Hematology and blood chemistry of mice following injection of iron oxide nanoparticles, prepared by thermal decomposition with sizes of ~5,~15, or ~30 nm and coated with PEG-phospholipid, or commercially obtained Feridex (as indicated). Red blood cell number, white blood cell number, percentage of neutrophils among white blood cells, hemoglobin concentration, hematocrit, mean corpuscular volume (MCV), mean corpuscular hemoglobin (MCH), and mean corpuscular hemoglobin concentration (MCHC) of mice 1, 14, and 30 days after intravenous injection with iron oxide nanoparticles (5 mgFe/kg). Statistical analyses were performed with Student's t test (*$p < 0.05$ for the difference between iron oxide nanoparticles and PBS, two-tailed, unpaired, n = 4-6, error bars = standard deviation). Reprinted with permission from [43]. Copyright 2012 American Chemical Society.

L. Gu et al. has *in vivo* evaluated the toxicity of iron oxide nanoparticles in blood and organs using mice [43]. As shown in Fig. 1.7, iron oxide nanoparticles did not show both toxicity for blood cells and damage for blood condition of mice. For organs, iron oxide nanoparticles induced no/slight damage in liver and spleen. Therefore, the safety of iron oxide nanoparticles was demonstrated *in vivo*.

In vivo *investigation of magnetic hyperthermia*

Here, an instance of *in vivo* investigation of magnetic hyperthermia is introduced as shown in Fig. 1.8.

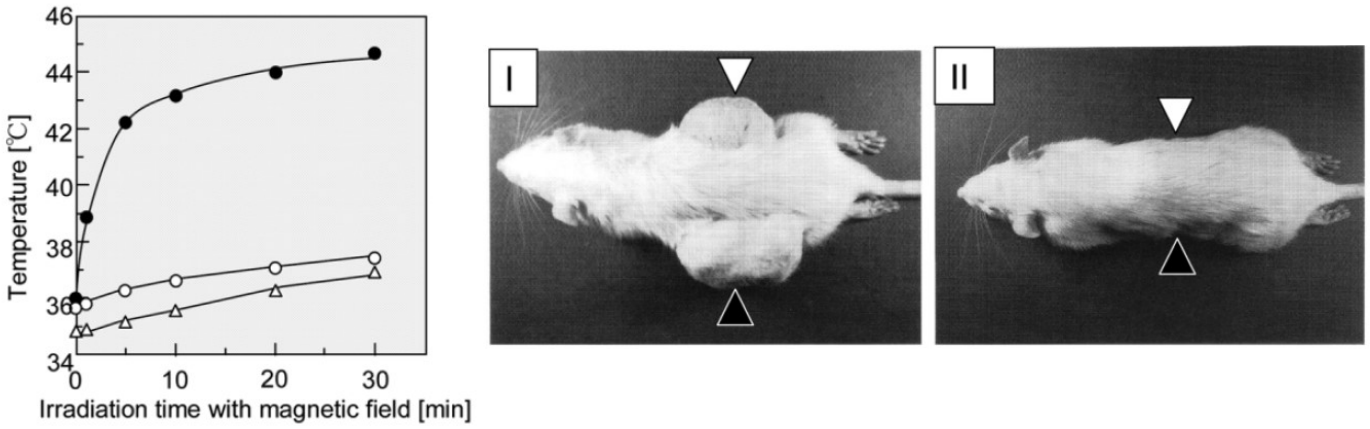

Fig. 1.8 Anti-cancer immune response induced by hyperthermia using magnetite nanoparticles. Rats with tumors on each side of the body were prepared. Particles were injected into the left tumor only and the rats were irradiated with an alternating magnetic field. The temperature of the left tumor, containing particles (closed circles), increased specifically, whereas the temperature of the right tumor (open circles) and rectum (open triangles) remained below 37°C (right panel). The tumor-specific hyperthermia treatment induced an anti-tumor immune response and both tumors disappeared on the 28th day after hyperthermia treatment. (I) Control rat without alternating-magnetic-field irradiation; (II) rat with alternating-magnetic-field irradiation. Open triangle in (I) and (II), the side without particles; closed triangle in (I) and (II), the side with particles. Adapted with permission from [44]. Copyright @ 2011 John Wiley & Sons, Inc.

T. Kobayashi reported that the tumor volume in mice was reduced with showing very high reduction rate when the tumor with Fe_3O_4 nanoparticles modified with cationic liposome were exposed to AC magnetic field [44]. Furthermore, the other side of tumor without Fe_3O_4 nanoparticles which was not observed temperature increase, has reduced because of activation of immune cells after the treatment of hyperthermia (remote effect). Therefore, ferrite nanoparticles show promise for magnetic hyperthermia [44].

1.2.4 Previous studies

T. Osaka and his group have been investigated the synthesis of Fe_3O_4 nanoparticles and their *in vitro* evaluation for magnetic hyperthermia previously.

First, they demonstrated the synthesis of Fe_3O_4 nanoparticles with the size tuned in the range of approximately 10 to 40 nm in mean diameter by chemical reaction in an aqueous solution containing iron(II) and iron(III) salts at various ratios with 1,6-hexanediamine as a base as shown Fig. 1.9 [45].

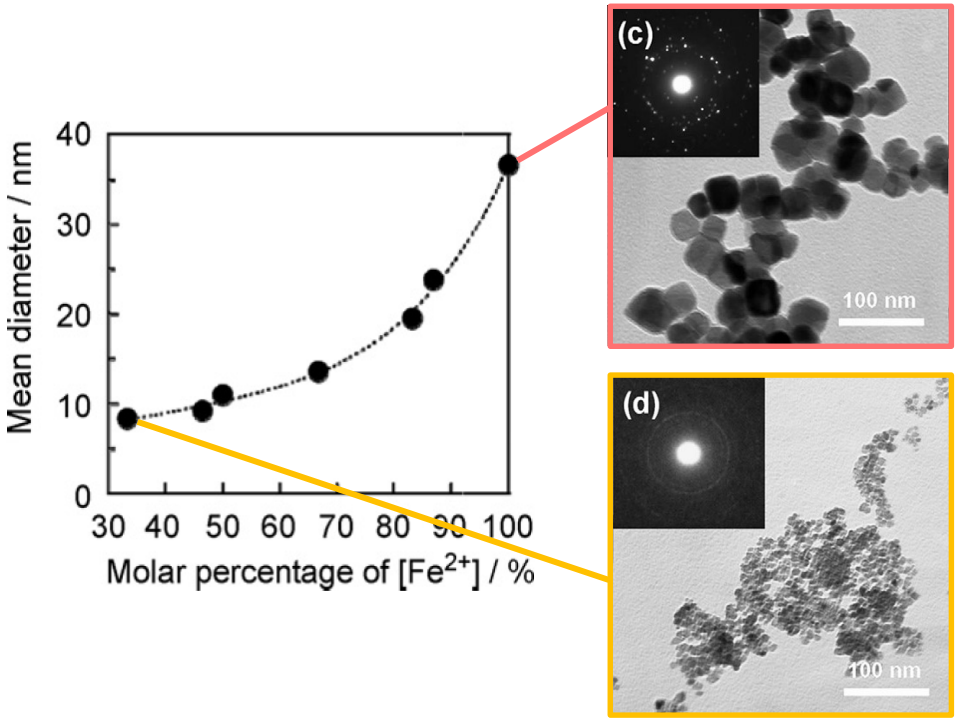

Fig. 1.9 Dependence of mean diameter of Fe_3O_4 nanoparticles on the molar percentage of ferrous ions in the total amount of iron ions. Reprinted with permission from [45]. Copyright @ 2007 Elsevier B. V.

The size of Fe_3O_4 nanoparticles was controlled by the preparation molar ratio of Fe^{2+} to Fe^{3+}. When the ratio of Fe^{2+} to Fe^{3+} was 1:2, 10-nm Fe_3O_4 nanoparticles were obtained via the famous

reaction (1.3). On the other hand, 40-nm Fe_3O_4 nanoparticles were obtained at the ratio of 1:0. In the mechanism of forming 40-nm Fe_3O_4 nanoparticles, three different reactions are suggested to be progressed as shown (1.4)-(1.6) [45-47]. Here organic amines are considered to serve not only as a base but also as a protective reagent. Magnetic properties of Fe_3O_4 nanoparticles can be controlled by the particle diameter [45].

$$Fe^{2+} + 2Fe^{3+} + 8OH^- \rightarrow Fe_3O_4 + 4H_2O. \quad (1.3)$$

$$Fe^{2+} + 2OH^- \rightarrow Fe(OH)_2. \quad (1.4)$$

$$3Fe(OH)_2 + 1/2O_2 \rightarrow Fe(OH)_2 + 2FeOOH + H_2O. \quad (1.5)$$

$$Fe(OH)_2 + 2FeOOH \rightarrow Fe_3O_4 + 2H_2O. \quad (1.6)$$

Second, they developed the synthetic method of Fe_3O_4 nanoparticles with positive charge using spermine, or *N*,*N*'-bis(3-aminopropyl)butane-1,4-diamine, as a base and a protective reagent instead of 1,6-hexanediamine [48]. Then, the percentage of breast cancer cells containing nanoparticles was compared for Fe_3O_4 nanoparticles synthesized with spermine or 1,6-hexanediamine. As a result, higher percentage was observed for Fe_3O_4 nanoparticles with spermine (positive charge) than those with 1,6-hexanediamine (negative charge) as shown in Fig. 1.10.

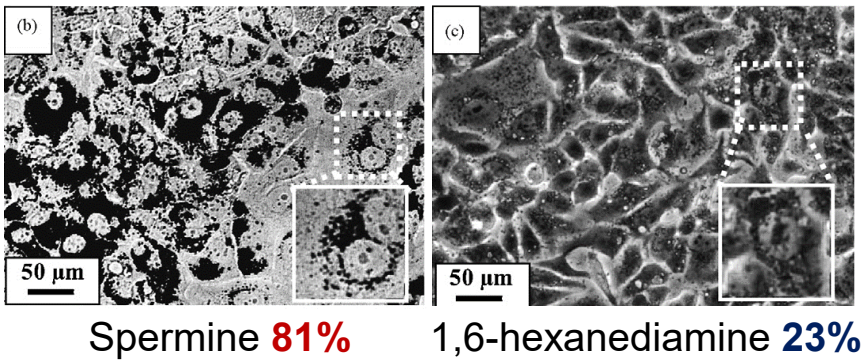

Fig. 1.10 Confocal microscopic images of human breast cancer MCF-7 cells after the incubation with two types of magnetite nanoparticles synthesized with spermine (left) and 1,6-hexanediamine (right). The indicated percentages mean the percentage of cells containing nanoparticles. Reprinted with permission from [48]. Copyright @ 2009 Elsevier B. V.

The mechanism of cellular uptake of nanoparticles is generally known to be endocytosis, whose process is classified with three steps: (i) accumulation of nanoparticles onto cell surface, (ii) invagination cell membrane with nanoparticles, and (iii) enclosing nanoparticles inside cells (forming endosome). Since cell surface is negatively charged, the adsorption of positively charged nanoparticles onto cell surface is easier than negatively charged nanoparticles in the step (i), which induced higher percentage of cells containing nanoparticles and larger uptake amount of nanoparticles per a cell [48].

Third, considering to biomedical application, Fe_3O_4 nanoparticles were evaluated for their safety by normal cells (mouse embryonic stem: mES cells) from the viewpoint of viability and damage of cell function [49]. As shown in Fig. 1.11, the viability of mES cells was approximately 100% at the dose range of 0 – 1000 μg/mL, and the ratio of undifferentiated cells was not altered when culturing with Fe_3O_4 nanoparticles. Therefore, the high safety of Fe_3O_4 nanoparticles was demonstrated using normal cells.

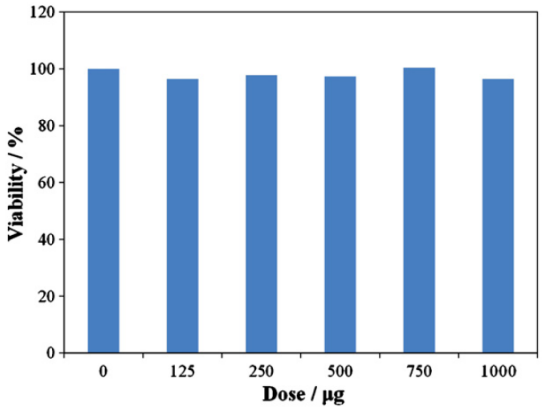

Condition	mES (%)	mES with added magnetite nanoparticles (%)
SSEA-1(+)	91.9	92.1
SSEA-1(−)	8.1	7.9

Fig. 1.11 Dose dependent of viability of mES cells.Fe_3O_4 nanoparticles were added to mES (0, 125, 250, 500, 750, 1000 μg/mL). mES cells were incubated for 24 h and stained by propidium iodide, and then viability was determined by flow cytometry (left) and the ratio of undifferentiated cells. mES and mES with added Fe_3O_4 nanoparticles were stained (right). Reprinted with permission from [49]. Copyright @ 2012 Elsevier B. V.

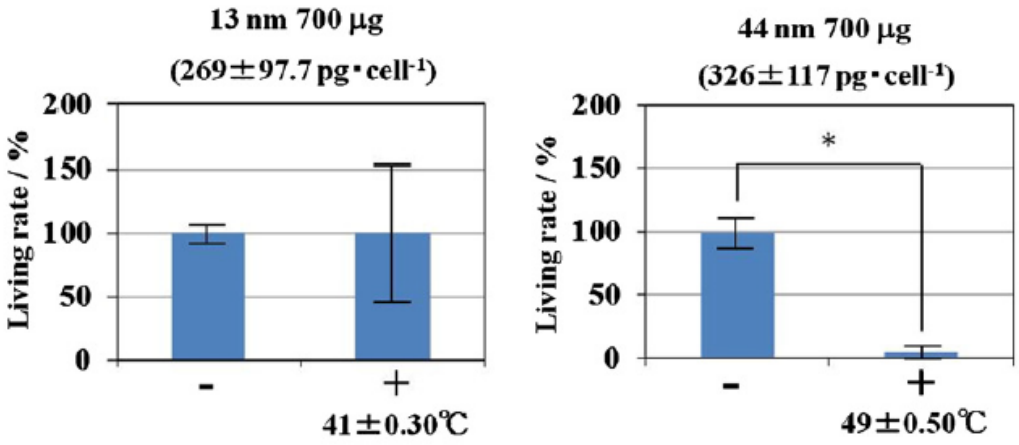

Fig. 1.12 Living rate of MCF-7 without (-) and with (+) magnetic irradiation at the dose of 700 μg. Reprinted with permission from [50]. Copyright @ 2012 Elsevier B. V.

With human breast cancer MCH-7 cells, they compared the effect of 10-nm (superparamagnetic) and 40-nm (ferromagnetic) Fe_3O_4 nanoparticles on induction of cell death under AC magnetic field. Consequently, ferromagnetic Fe_3O_4 nanoparticles showed higher cell mortality than superparamagnetic nanoparticles, as shown in Fig. 1.12 [50].

1.3 My approach of nanoparticles design for magnetic hyperthermia

There has already been a beneficent clinical report of implant magnetic hyperthermia with FePt needles for the treatment of tongue cancer in 1996 [51]. Hence, magnetic hyperthermia is expected to become a useful cancer therapy, but there is no beneficent clinical report for the treatment of cancer located in human body. For the treatment of tumor with a diameter of 5 mm, at least 650 μg/cm^3 of magnetic nanoparticles is estimated to be needed. However, accumulation of nanoparticles into tumors at the concentration of >650 μg/cm^3 is difficult. Furthermore, superparamagnetic nanoparticles such as commercial iron-oxide nanoparticles of Feridex® and Resovist® being clinically used as MRI contrast agents are suitable for the administration into human body (intravenous injection) although, they has been reported to show too low heating efficacy to induce cell death effectively [39,50,52]. Also, they are poorly taken up by cells [53].

In this situation, accumulation of nanoparticles to tumors can be achieved by a direct injection of nanoparticles into tumors on/under the human skin, and into tumors situated deep in the body using a catheter. Moreover, nanoparticles can be obtained the selectivity of cancer cells by modification with a cancer-selective material. However, there is room for improvements in the design of nanoparticles for enhancing the therapeutic effect. In particular, the control of magnetic properties of nanoparticles appropriate to the applied condition of AC magnetic field for an increase in the heating efficacy of nanoparticles is a key issue for practical use of magnetic hyperthermia.

In this background, employing ferromagnetic nanoparticles as a heat generator of magnetic hyperthermia is considered in my approach, to overcome the issue. There is little concern of forming a blood clot by directly injecting nanoparticles into tumors using a catheter.

In this thesis, taking advantages of the results found by T. Osaka and his group as mentioned in the section 1.2.4, 10- and 40-nm Fe_3O_4 nanoparticles were synthesized by co-precipitation (hydrolysis) method with an organic amine as a base and a protective reagent. 10- and 40-nm Fe_3O_4 nanoparticles were employed to obtain superpara- and ferromagnetic nanoparticles. As an organic amine, spermine was employed with expectation of an enhancement in cellular uptake of nanoparticles by their positive charge.

The applied condition of AC magnetic field is also important for the design for effective magnetic hyperthermia. In this thesis, considering to the coercivity of 40-nm Fe_3O_4 nanoparticles

which has been reported to be approximately 100-200 Oe [45,50], the strength of applied magnetic field on the induction-heating device was set to 536 Oe. In this case, the effective strength of magnetic field is assumed to be around 200-300 Oe. The applied condition of AC magnetic field for medical care was defined by the International Commission on Non-Ionizing Radiation Protection, which is $< 5 \times 10^9\ A \cdot m^{-1} \cdot s^{-1}$ of a product of magnetic field amplitude and frequency. Generally, higher frequency induces larger heat generation in magnetic hyperthermia. Considering to the effective strength of magnetic field in this thesis (200-300 Oe), the maximum frequency in the range of the definition is estimated to be around 300 kHz. Therefore, 325 kHz of frequency was employed in this thesis.

In the design of nanoparticles for effective magnetic hyperthermia, there are two major significant points to achieve the objective.

(i) To understand the interactions (influence) between nanoparticles and cells

(ii) To control magnetic and surface properties of nanoparticles

Based on the point (i), using synthesized 10-nm and 40-nm Fe_3O_4 nanoparticles (MNPs) with positive charge, induction of cell death by MNPs in mesothelioma cells was investigated in Chapter 2. Malignant mesothelioma is a tumor situated deep part of human body with little effective treatment. Then, taking advantages of the findings of Chapter 2, surface design of MNPs and their effect on melanoma tumor in mice was also investigated in Chapter 3. Melanoma was employed because the method of making tumor into mice has been established and magnetic hyperthermia can be easily applied to tumors located on/under human skin, in principle.

Based on the point (ii), control of magnetic properties of MFe_2O_4 (M = Co, Mg) nanoparticles for increase in heating efficacy was focused in Chapter 4, as a study leading to the future technology. Furthermore, through the investigation of the effect of MFe_2O_4 nanoparticles synthesized on breast cancer cells, the advantages of each ferrite nanoparticles was compared and discussed. Breast cancer cells were also employed because magnetic hyperthermia can be easily applied to tumors located on/under human skin.

As an example of applications of ferrite nanoparticles, magnetic cell separation using 40-nm ferromagnetic Fe_3O_4 nanoparticles and microalgae was discussed in Chapter 5. Microalgae were employed because effective cell separation is required for practical commercialization of

microalgal biomass production.

Overall, from the viewpoint of control of magnetic properties, this thesis aimed to contribute as a recipe to material engineering approach for the practical use of ferrite nanoparticles to magnetic hyperthermia.

Reference

[1] M. Auffan et al., "Towards a definition of inorganic nanoparticles from an environmental, health and safety perspective", *Nat. Nanotechnol.*, 4, 634 (2009).

[2] C. B. Murray et al., "Synthesis and characterization of monodisperse nanocrystals and close-packed nanocrystal assemblies", *Annu. Rev. Mater. Sci.*, 30, 545 (2000).

[3] M.-C. Daniel and D. Astruc, "Gold Nanoparticles: Assembly, Supramolecular Chemistry, Quantum-Size-Related Properties, and Applications toward Biology, Catalysis, and Nanotechnology", *Chem. Rev.*, 104, 293 (2004).

[4] I. L. Medintz et al., "Quantum dot bioconjugates for imaging, labelling and sensing", *Nat. Mater.*, 4, 435 (2005).

[5] Q. Sun et al., "Bright, multicoloured light-emitting diodes based on quantum dots", *Nat. Photonics*, 1, 717 (2007).

[6] E. W. Gorter, "Magnetization in ferrites ~Saturation magnetization of ferrites with spinel structure~", *Nature*, 165, 798 (1950).

[7] D. S. Mathew and R.-S. Juang, "An overview of the structure and magnetism of spinel ferrite nanoparticles and their synthesis in microemulsions", *Chem. Eng. J.*, 129, 51 (2007).

[8] T. Tsushima, T. Teranishi, K. Ohta, in *Jiseitai Handbook -Handbook of Magnetic Materials-* (Ed. S. Chikazumi, Asakura Shoten, Tokyo, 1975), p. 612 (in Japanese).

[9] J. C. Slonczewski, "Origin of Magnetic Anisotropy in Cobalt-Substituted Magnetite", *Phys. Rev.*, 110, 1341 (1958).

[10] J. Carrey et al., "Simple models for dynamic hysteresis loop calculations of magnetic single-domain nanoparticles: Application to magnetic hyperthermia optimization", *J. Appl. Phys.*, 109, 083921 (2011).

[11] R. Massart, "Magnetic fluids and process for obtaining them", *United States Patent* 4,329,241, May 11 (1982).

[12] S. Sun and H. Zeng, Size-Controlled Synthesis of Magnetite Nanoparticles, *J. Am. Chem. Soc.*, 124, 8204 (2002).

[13] P. Wust et al., "Hyperthermia in combined treatment of cancer", *Lancet Oncol.*, 3, 487 (2002).

[14] J. van der Zee, "Heating the patient: a promising approach?", *Ann. Oncol.*, 13, 1173 (2002).

[15] J. Overgaard, "Effect of hyperthermia on malignant cells *in vivo* – A review and a hypothesis", *Cancer*, 39, 2637 (1977).

[16] M. Abe et al., "Multi-Institutional studies on hyperthermia using an 8-MHz radiofrequency capacitive heating device (Thermotron RF-8) in combination with radiation for cancer therapy", *Cancer*, 58, 1589 (1986).

[17] C. W. Song et al., "Capacitive heating of phantom and human tumors with an 8 MHz radiofrequency applicator (Thermotron RF-8)", *Int. J. Radiat. Oncol. Biol. Phys.*, 12, 365 (1986).

[18] S. Mornet et al., "Magnetic nanoparticle design for medical diagnosis and therapy", *J. Mater. Chem.*, 14, 2161 (2004).

[19] A. K. Gupta and M. Gupta, "Synthesis and surface engineering of iron oxide nanoparticles for biomedical applications", *Biomaterials*, 26, 3995 (2005).

[20] A. Ito et al., "Medical application of functionalized magnetic nanoparticles", *J. Biosci. Bioeng.*, 100, 1 (2005).

[21] C. Sun et al., "Magnetic nanoparticles in MR imaging and drug delivery", *Adv. Drug Deliv. Rev.*, 60, 1252 (2008).

[22] T. Fuchigami et al., "A magnetically guided anti-cancer drug delivery system using porous FePt capsules", *Biomaterials*, 33, 1682 (2012).

[23] F. Y. Cheng et al., "Characterization of aqueous dispersions of Fe_3O_4 nanoparticles and their biomedical applications", *Biomaterials*, 26, 729 (2005).

[24] Q. A. Pankhurst et al., "Applications of magnetic nanoparticles in biomedicine", *J. Phys. D: Appl. Phys.*, 36, R167 (2003).

[25] C. S .S. R. Kumar and F. Mohammad, "Magnetic nanomaterials for hyperthermia-based therapy and controlled drug delivery", *Adv. Drug Deliv. Rev.*, 63, 789 (2011).

[26] W.-H. Chiang et al., "Superparamagnetic hollow hybrid nanogels as a potential guidable vehicle system of stimuli-mediated MR imaging and multiple cancer therapeutics", *Langmuir*, 29, 6434 (2013).

[27] A. Jordan et al., "Inductive heating of ferrimagnetic particles and magnetic fluids: physical evaluation of their potential for hyperthermia", *Int. J. Hyperthermia*, 9, 51 (1993).

[28] R. Hergt et al., "Magnetic particle hyperthermia: nanoparticle magnetism and materials development for cancer therapy", *J. Phys. Condens. Matter*, 18, S2919 (2006).

[29] R. Rastogi et al., "Evaluation of folate conjugated pegylated thermosensitive magnetic nanocomposites for tumor imaging and therapy", *Colloids Surf. B Biointerfaces*, 82, 160

(2011).

[30] Y. Xu et al., "Multifunctional Fe_3O_4 Cored Magnetic-Quantum Dot Fluorescent Nanocomposites for RF Nanohyperthermia of Cancer Cells", *J. Phys. Chem. C*, 114, 5020 (2010).

[31] T. Chen et al., "Smart Multifunctional Nanostructure for Targeted Cancer Chemotherapy and Magnetic Resonance Imaging", *ACS Nano*, 5, 7866 (2011).

[32] M. N. Luwang et al., "Dendrimer facilitated synthesis of multifunctional lanthanide based hybrid nanomaterials for biological applications", *J. Mater. Chem.*, 22, 3395 (2012).

[33] A. Tomitaka et al., "Heat dissipation and magnetic properties of surface-coated Fe_3O_4 nanoparticles for biomedical application", *J. Magn. Magn. Mater.*, 324, 3437 (2012).

[34] Y. Jiao et al., "Tumor-Targeting Multifunctional Rattle-Type Theranostic Nanoparticles for MRI/NIRF Bimodal Imaging and Delivery of Hydrophobic Drugs", *Small*, 11, 1962 (2015).

[35] A. Espinosa et al., "Duality of Iron Oxide Nanoparticles in Cancer Therapy: Amplification of Heating Efficacy by Magnetic Hyperthermia and Photothermal Bimodal Treatment", *ACS Nano*, 10, 2436 (2016).

[36] R. Hergt et al., "Physical limits of hyperthermia using magnetite fine particles", *IEEE Trans. Magn.*, 34, 3745 (1998).

[37] R. E. Rosensweig, "Heating magnetic fluid with alternating magnetic field", *J. Magn. Magn. Mater.*, 252, 370 (2002).

[38] M. Ma et al., "Size dependence of specific power absorption of Fe_3O_4 particles in AC magnetic field", *J. Magn. Magn. Mater.*, 268, 33 (2004).

[39] M. Suto et al., Heat dissipation mechanism of magnetite nanoparticles in magnetic fluid hyperthermia, *J. Magn. Magn. Mater.*, 321, 1493 (2009).

[40] R. Ghosh et al., "Induction heating studies of Fe_3O_4 magnetic nanoparticles capped with oleic acid and polyethylene glycol for hyperthermia", *J. Mater. Chem.*, 21, 13388 (2011).

[41] S. Ota et al., "Dipole-dipole interaction and its concentration dependence of magnetic fluid evaluated by alternating current hysteresis measurement", *J. Appl. Phys.*, 117, 17D713 (2015).

[42] H. L. Karlsson et al., "Copper Oxide Nanoparticles Are Highly Toxic: A Comparison between Metal Oxide Nanoparticles and Carbon Nanotubes", *Chem. Res. Toxicol.*, 21, 1726 (2008).

[43] L. Gu et al., "*In Vivo* Clearance and Toxicity of Monodisperse Iron Oxide Nanocrystals", *ACS Nano*, 6, 4947 (2012).

[44] T. Kobayashi, "Cancer hyperthermia using magnetic nanoparticles", *Biotechnol. J.*, 6, 1342 (2011).

[45] H. Iida et al., "Synthesis of Fe_3O_4 nanoparticles with various sizes and magnetic properties by controlled hydrolysis", *J. Colloid Interface Sci.*, 314, 274 (2007).

[46] P.H. Refait and J.-M. R. Génin, "The Oxidation of Ferrous Hydroxide in Chloride-containing Aqueous Media and Pourbaix Diagrams of Green Rust One", *Corros. Sci.*, 34, 797 (1993).

[47] A. A. Olowe and J.-M. R. Génin, "The Influence of Concentration on the Oxidation of Ferrous Hydroxide in Acidic Sulphated Aqueous Medium: Particle Size Analysis of Lepidocrocite", *Corros. Sci.*, 32, 965 (1991).

[48] T. Osaka et al., "Effect of surface charge of magnetite nanoparticles on their internalization into breast cancer and umbilical vein endothelial cells", *Colloids Surf. B Biointerfaces*, 71, 325 (2009).

[49] C. Shundo et al., "Cytotoxicity evaluation of magnetite (Fe_3O_4) nanoparticles in mouse embryonic stem cells", *Colloids Surf. B Biointerfaces*, 97, 221 (2012).

[50] D. Baba et al., "Effect of magnetite nanoparticles on living rate of MCF-7 human breast cancer cells", *Colloids Surf. B Biointerfaces*, 95, 254 (2012).

[51] I. Tohnai et al., "Preoperative thermochemotherapy of oral cancer using magnetic induction hyperthermia (Implant Heating System: IHS)", *Int. J. Hyperthermia*, 12, 37 (1996).

[52] Y. Oh et al., "*In vitro* study on apoptotic cell death by effective magnetic hyperthermia with chitosan-coated $MnFe_2O_4$", *Nanotechnology*, 27, 115101 (2016).

[53] I. Raynal et al., "Macrophage endocytosis of superparamagnetic iron oxide nanoparticles: mechanisms and comparison of ferumoxides and ferumoxtran-10", *Invest. Radiol.*, 39, 56 (2004).

Chapter 2

Induction of cell death by Fe_3O_4 nanoparticles in mesothelioma cells

2.1 Introduction

The objective and motivation of this chapter is to understand the interactions (influence) between nanoparticles and cells in detail, using mesothelioma cells.

With regard to a magnetic design of MNPs, 10-nm superparamagnetic and 40-nm ferromagnetic MNPs were employed in this study to compare magnetic properties of MNPs for effective induction of cell death. The 40-nm ferromagnetic MNPs were reported to have higher heating capacity under AC magnetic field rather than 10-nm MNPs [1]. As for surface design of MNPs, spermine which possess positively charged moiety was employed as a base and a protective reagent in the synthetic process of MNPs in co-precipitation (hydrolysis) [2], in order to enhance MNPs incorporation into cells [3].

Malignant pleural or peritoneal mesothelioma is an aggressive tumor that develops after asbestos exposure [4-7]. The mechanism of mesothelioma development is still unknown, but it has been newly suggested that iron overload in the mesothelial tissue is a key in asbestos (chrysotile, crocidolite, and amosite)-induced mesothelial carcinogenesis [8]. There are three histological subtypes (epithelioid, sarcomatoid, and biphasic) in mesothelioma from the differences of cell morphology and surface proteins [7,9]. Around 60% of total mesothelioma patients are categorized as “epithelioid”, 20% are “sarcomatoid” patients, and the others are classified as “biphasic” [9]. In mesothelioma diagnosis, according to a report from the National Cancer Institute, physical exam and history, chest X-ray, CT scan, and biopsy are generally used [10].

The World Health Organization (WHO) has reported that 92,253 people mesothelioma deaths were recorded in 83 countries for the period of 1994 to 2008 [11]. It should be emphasized here that mesothelioma treatment still have a major worldwide problem [5,8,9-15]. Primary treatment

of mesothelioma is surgical resection [5,8,9,16], radiation therapy [5,8], and chemotherapy [5,8,9,17]. However, survival rates are very low because mesothelioma is usually situated deep in the body and is resistant to chemotherapeutic agents. The median overall survival of mesothelioma patients with no treatment was 4.1 months (95% confidence interval, 3.4-4.8). But even if those were treated, the median overall survival was still low such as 15.1 (12.0-19.0) with both radical surgery and systemic chemotherapy, 8.6 (6.6-10.5) with radical surgery but no systemic chemotherapy, and 9.3 (8.4-10.2) with systemic chemotherapy but no radical surgery [9]. Moreover, surgical removal is invasive and chemotherapy has negative side effects. Although multimodal therapy combining two or more treatments, is proposed to improve the survival rate and quality of life [3,16-18], the most effective combination is still contested. Therefore, more effective treatments for mesothelioma, for prolonging survival or effecting a cure, are strongly required.

To overcome the issue, nanoparticle uptake and cell death induced by the addition of MNPs were evaluated in three histological types of human mesothelioma cells, i.e. NCI-H28 (epithelioid), NCI-H2052 (sarcomatoid), and MSTO-211H (biphasic) cells, and the future application of MNPs to mesothelioma treatment is considered in this chapter. This study described here represents the first investigation of cellular uptake and cytotoxicity of MNPs in three histological cell types, in addition to their cell death induced by MNPs subjected to alternating magnetic field.

2.2 Experimental

Cell culture

Human mesothelioma NCI-H28, NCI-H2052, and MSTO-211H cells (American Type Culture Collection) were maintained in RPMI-1640 medium (Sigma-Aldrich, St. Louis, MO) containing 10% fetal bovine serum (FBS; ThermoFisher Scientific, Waltham, MA) and 1% penicillin-streptomycin (Sigma-Aldrich). Human breast cancer MCF-7 cells were cultured in Eagle's minimum essential medium (EMEM; Sigma-Aldrich) with 10% FBS, 5% L-glutamine (Invitrogen, Life Technologies, Grand Island, NY), 1% MEM non-essential amino acid (Gibco, Life Technologies), and 1% antibiotic-antimycotic (Gibco). All cells were incubated at 37°C under a 5% CO_2 atmosphere. Cell condition of MSTO-211H was evaluated by analysis of incubation-time dependence of cell productivity and by fluorescence-observation of actin-staining cells using an F-Actin Visualization Biochem Kit™ (Cytoskeleton, Inc.) according to the manufacturer's protocol.

Synthesis and characterization of magnetite nanoparticles (MNPs)

MNPs were synthesized by hydrolysis of an aqueous solution containing ferrous chloride ($FeCl_2 \cdot 4H_2O$) and ferric chloride ($FeCl_3 \cdot 6H_2O$), using essentially the same procedure as described in a literature [2], except for the use of spermine, or *N*,*N*'-bis(3-aminopropyl)butane-1,4-diamine, as a base instead of 1,6-hexanediamine. Iron salts and spermine were purchased from Kanto Chemical Co. Ltd. (Tokyo, Japan) and Sigma-Aldrich Japan, respectively. 50 mL of an aqueous solution containing ferrous chloride and ferric chloride at a molar ratio of 2:1 (for 10-nm MNPs) or 1:0 (for 40-nm MNPs), the total amount of which was 0.05 mol dm^{-3}, was mixed with 50 mL of an aqueous solution containing 0.125 mol dm^{-3} of spermine, and the mixture was stirred at room temperature. After stirring for 24 h (for 10-nm MNPs) or 4 h (for 40-nm MNPs), the black precipitate was separated using a permanent magnet and washed several times with ultrapure water and ethanol. The final products were obtained, in the form of a black powder, after drying in a desiccator at room temperature. The shape and size of the products were observed by transmission electron microscopy (TEM) with a JEOL JEM-1011 microscope (Tokyo, Japan) or

a Hitachi H-7650 microscope (Tokyo, Japan) operated at an acceleration voltage of 100 kV. The mean diameter of products were calculated using a following equation after counting and measuring diameters (D_n) of one hundred nanoparticles in TEM images.

$$\text{Mean diameter} = \frac{(D_1+D_2+D_3+\cdots+D_{100})}{100} \quad (1)$$

The crystal structure of the products was characterized by X-ray diffraction (XRD) patterns recorded using a RINT ULTIMA III diffractometer (Rigaku, Tokyo, Japan) with Cu Kα radiation (1.5418 Å). The zeta potential and hydrodynamic diameter of the specimens dispersed in water at around pH 7 were evaluated using an Otsuka Electronics ELS-8000 light-scattering photometer (Osaka, Japan).

Evaluation of cytotoxicity and cellular uptake

NCI-H28, NCI-H2052, MSTO-211H, and MCF-7 cells were cultured in 6-well plates at a density of 5×10^5 cells per 3 mL of medium in each well, and then incubated without or with 10-nm MNPs at 200, 400, 600, and 800 μg per well. After incubation for 24 h, the cells were washed with Dulbecco's phosphate buffered saline (DPBS; Gibco) to remove excess MNPs. The morphology of MSTO-211H and MCF-7 cells was observed using a Nikon TE2000-U microscope (Tokyo, Japan). Cell pellets were obtained by centrifugation at 1200 rpm for 5 min, and suspended in 1 mL of DPBS supplemented with 6% FBS, followed by staining with 2 μL of 42 μM thiazole orange (TO) in dimethyl sulfoxide and 1 μL of 4.3 mM propidium iodide (PI) in water. TO and PI were purchased from BD Biosciences, Becton, Dickinson and Co. (Franklin Lakes, NJ) as part of the BD Cell Viability Kit. Immediately following this treatment, the cells were analyzed with a BD FACSCanto II flow cytometer. PI stains dead cells only, whereas TO stains both living and dead cells. Dead cells were recognized by their PI-positive response and cells were distinguished from MNPs by TO positive staining. Cellular uptake of MNPs was measured using side scatter (SSC) section. The ratio of cells containing MNPs to the total number of cells was determined in the following way. In a flow cytometer, light scattering occurs when a cell deflects incident laser light. The scattered light is collected as forward scatter (FSC) and SSC. The SSC depends on the inner complexity of the cell because SSC measures refracted and reflected light at a side angle to

the laser path. Therefore, high values along the SSC axis would indicate that the cells contained MNPs. To discuss the cellular uptake of MNPs, TEM observation of NCI-H28, NCI-H2052, and MSTO-211H incubated with 800 μg of MNPs was performed at the Hanaichi UltraStructure Research Institute Co., Ltd. (Aichi, Japan) with a JEOL JEM1200EX at an acceleration voltage of 80 kV. To prepare specimens for TEM observation, cells were washed with 0.1 M phosphate buffer, fixed with 2% osmium tetroxide, dehydrated with 50–100% ethanol, embedded in EPON812, and finally sectioned using an ultramicrotome. The amount of MNPs incorporated into a NCI-H28, NCI-H2052, or MSTO-211H cell was evaluated using a literature-described procedure [16,19]. HCl, trichloroacetic acid solution, H_2O_2, and potassium thiocyanate solution were used to dissolve cells with MNPs, to precipitate the cellular proteins, to oxidize Fe^{2+} into Fe^{3+}, and to form a thiocyanate-iron(III) complex; finally, the absorbance at 480 nm was measured using a JASCO V-550 spectrophotometer (JASCO International Co. Ltd., Tokyo, Japan).

Detection of DNA fragmentation in apoptotic cells

MSTO-211H cells were cultured at a density of 5×10^5 per well in the presence of 800 μg of 10-nm MNPs as described above. After 24-h incubation, a DNA fragmentation assay was performed using a Quick Apoptotic DNA Ladder Detection Kit (Invitrogen) according to the manufacturer's protocol. After extraction of chromosomal DNA, DNA fragmentation was analyzed by agarose gel electrophoresis. The DNA fragments were viewed under UV light and photographed.

Microarray analysis

NCI-H28, NCI-H2052, and MSTO-211H cells were cultured for 24 h at the density of 5×10^5 per well in the presence of 800 μg MNPs as described above. Total RNA isolation and gene expression microarrays were performed at Cell Innovator Inc. The total RNA was isolated from cerebellums of each individual animal using TRIzol Reagent (Invitrogen) and purified using SV Total RNA Isolation System (Promega) according to the manufacturer's instructions. Gene expression microarray was performed using Agilent SurePrint G3 Human Gene Expression Microarray 8 × 60K v2. The cRNA was amplified and labeled using Agilent Low Input Quick

Amp Labeling Kit, and hybridized to a 60K Agilent 60-mer oligomicroarray according to the manufacturer's instructions. All hybridized microarray slides were scanned by an Agilent scanner. Relative hybridization intensities and background hybridization values were calculated using Agilent Feature Extraction Software (9.5.1.1). Microarray data of samples were normalized by quantile algorithm.

Evaluation of cell death with MNPs subjected to alternating magnetic field.

MNPs with a diameter of 40 nm, such as ferromagnetic MNPs, were employed here.

Prior to the experiments using MNPs and cells, heating capacity of MNPs was investigated. To evaluate the heating capacity of MNPs, a sample which contains 1.0 mg of MNPs dispersed in 500 μL of water or fixed in 500 μL of 1% agarose gel was subjected to AC magnetic field induced using a device of EASYHEAT (Alonics, Ltd., Tokyo, Japan) including a 3-turn coil with an outside diameter of 40 mm, at a frequency of 325 kHz with a current of 569.1 A for 20 min. By making use of above values for estimation of the strength of magnetic field, that is calculated to be 536 Oe. During exposure, the temperature of sample was recorded every a second with an Anritsu FL-2000 fiber thermometer (Tokyo, Japan), and cooling water was circulated in the coil using a DC inverter chiller RKE1500B1-V (Nagano, Japan) to prevent the influence of the heat from coil to the temperature of a sample. Specific adsorption rates (SARs) were determined from the slope between 0 and 100 s in the recorded temperature curves using parameters of specific heat capacity (C_{pi}) and mass for each substance (m_{i}) or MNPs (m_{MNPs}), by a following equation.

$$\mathrm{SAR} = \frac{\sum_i C_{pi} m_i}{m_{MNPs}} \cdot \frac{\Delta T}{\Delta t} \tag{2}$$

A magnetization curve at the magnetic field of -10000 to 10000 Oe at 300 K was measured using a BHV-35 vibrating sample magnetometer (VSM; Riken Denshi Co. Ltd., Tokyo, Japan).

In this section, 5×10^5 or 1×10^5 of NCI-H28 and MSTO-211H cells or NCI-H2052 cells, which were cultured to adhere for 24 h in advance, were incubated for further 24 h with MNPs at concentrations of 0, 133, 267 μg/mL, respectively. Cell numbers cultured with MNPs were determined considering cell condition such as viability and density of cells after 48-h cultivation.

The MNPs-containing 5×10^5 cells collected by magnetic separation were dispersed in 500 μL of medium and then subjected to 20 min of AC magnetic field (325 kHz, 500 Oe) with measuring the sample temperature every a second. Cell mortality immediately after exposure to AC magnetic field was evaluated by cell counting with trypan blue (TB; Gibco) staining. Prior to the exposure also, cell mortality of samples was evaluated. Live cells are TB negative, whereas dead cells are TB positive, hence cell mortality was calculated by a following formula.

$$\text{Cell mortality (\%)} = \frac{Counts\ of\ TB\ positive\ cells}{Counts\ of\ all\ cells} \times 100 \quad (3)$$

The percentage of non-viable cells, which was evaluated by cell counting after the 20 min of exposure to AC magnetic field, was compared with that evaluated after 20-min heating using a THERMAL ROBO TR-1A thermostatic water bath (AS ONE Corporation, Osaka, Japan). Temperatures in thermostatic bath were set on the average temperatures between 800 and 1200 s obtained from the temperature curves of samples exposed to AC magnetic field.

Time course of cell mortality after the exposure of cells containing MNPs to AC magnetic field was also investigated. After exposure, the cells were incubated for further 24 h at 37°C under a 5% CO_2 atmosphere. Same experiment was performed on the cells containing MNPs without exposure to AC magnetic field. Cell morphology after the 24-h incubation was observed using a Nikon TE2000-U microscope (Tokyo, Japan). The mode of cell death was evaluated by flow cytometric analysis using a PE Annexin V Apoptosis Detection Kit I (BD Pharmingen) according to the manufacturer's protocol.

2.3 Characterization of Fe_3O_4 nanoparticles

Fig 2.1 shows TEM images, histograms of particle size distribution, and XRD patterns of the MNPs employed in this study. TEM observation showed that particle shape and size were consistent with a previous report [16-19]. One hundred nanoparticles were counted to determine their size distribution; the mean particle diameters were 10.3 ± 1.7 and 42.7 ± 8.9 nm, shown in Fig. 2.1B and D, respectively. The XRD patterns of the samples (Fig. 2.1E) matched the standard pattern of Fe_3O_4 (JCPDS# 19-629) and the *d* value of the lattice spacing of (311) was calculated to be 2.528 and 2.534 Å for (a) and (b), respectively, using the Bragg equation for the peak observed at $2\theta \sim 36°$. The calculated values were concordant with the standard value for Fe_3O_4 of 2.532 Å (JCPDS# 19-629), not with the value for γ-Fe_2O_3 of 2.518 Å (JCPDS# 39-1346), similar to a previous report [2]. The zeta potentials of 10-nm and 40-nm MNPs, measured in water at around pH 7, were +10.7 and +16.8 mV, respectively, which is attributable to the cationic form of the amine groups in spermine adsorbed on the surface of the nanoparticles as a protecting reagent [3]. To consider the state dispersed in solution, the size distribution of MNPs in ultrapure water was evaluated by the light scattering method. The size distribution of 10-nm and 40-nm MNPs in ultrapure water suggests the formation of an aggregation or secondary particle with a hydrodynamic diameter of approximately 1 μm. The interaction among the protecting agent, spermine in the present study, may contribute to form secondary particles in water. Additionally, from TG analysis, the contribution of spermine molecules to the weight of samples was evaluated as much as 9.6 weight percent for each specimen, which was comparable to the mass fraction (5 wt%) calculated from the model for monolayer adsorption of spermine on 10-nm MNPs by using values of theoretical surface-to-volume ratio, density, and formula weight.

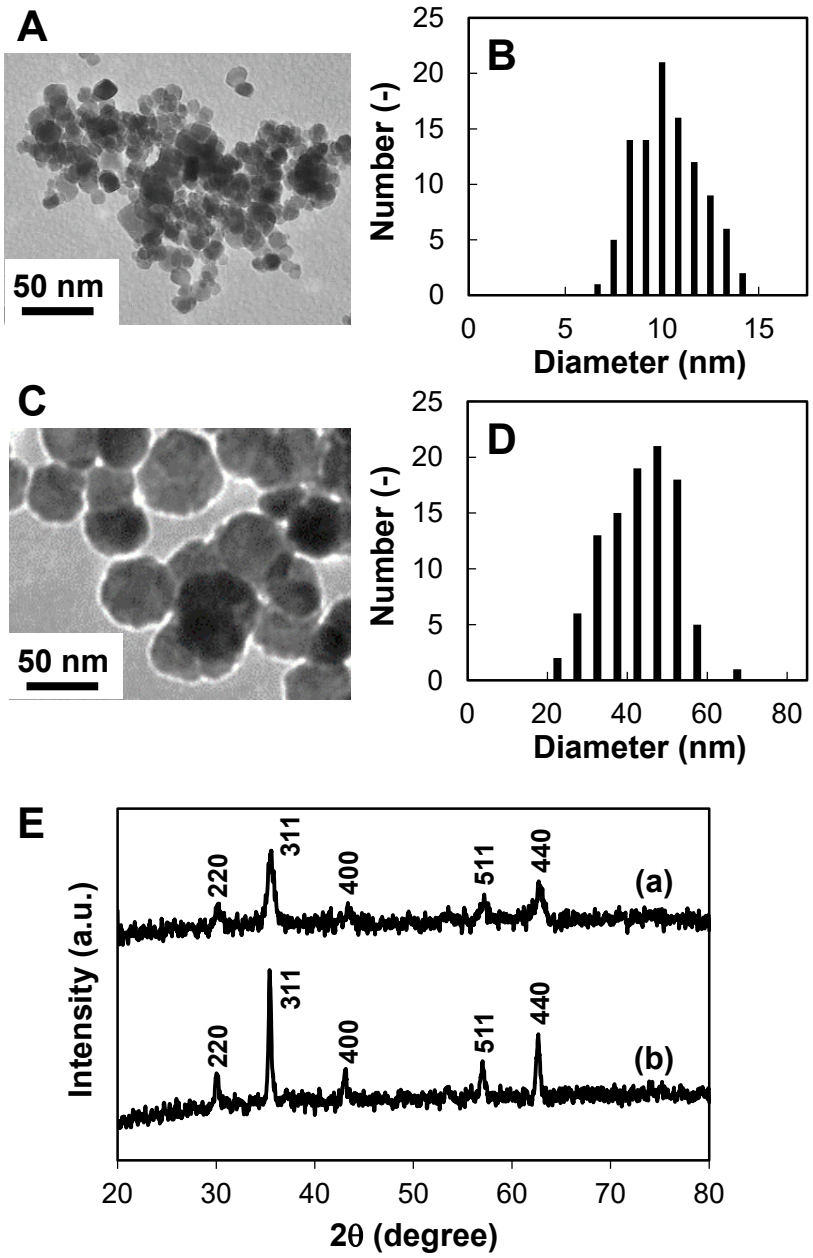

Fig. 2.1 Characterization of the MNPs employed in this study. TEM images (A,C) and size distribution (B,D) of "10-nm" MNPs (A,B) and "40-nm" MNPs (C,D). XRD patterns with Cu Kα radiation (E) of "10-nm" MNPs (a) and "40-nm" MNPs (b). Reprinted with Permission. Copyright 2015 American Chemical Society.

2.4 Effect of addition of nanoparticles on cellular uptake and cell death

First, the morphology of MSTO-211H and MCF-7 cells cultured without and with the addition of 10 nm MNPs was observed.

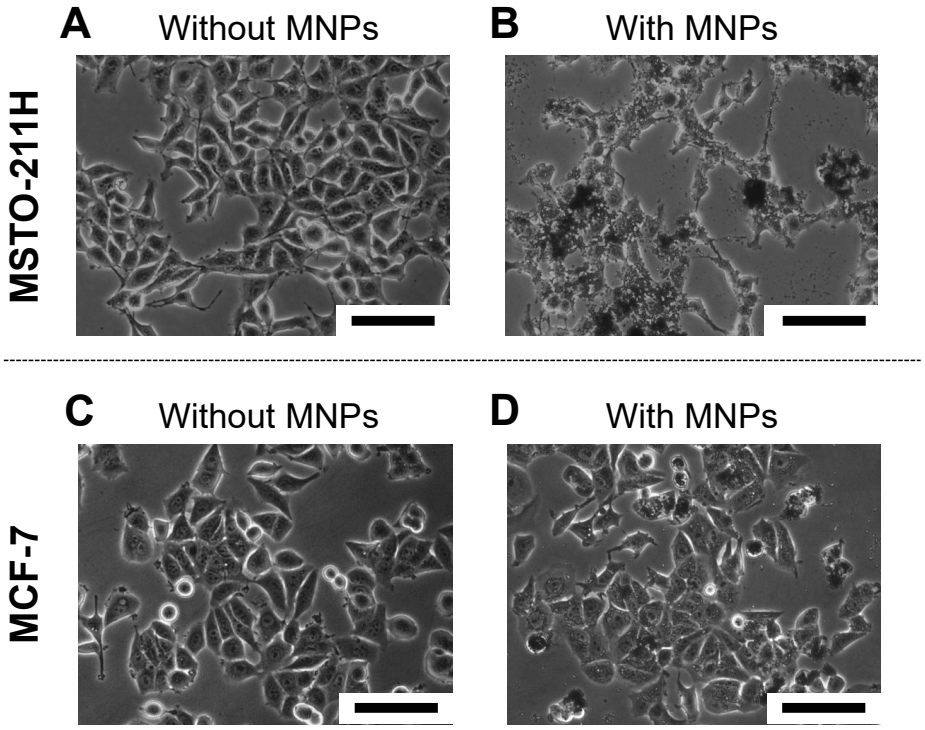

Fig. 2.2 Cell morphology of MSTO-211H (A, B) and MCF-7 (C, D) cells after incubation for 24 h without (A, C) and with (B, D) MNPs. In B and D, 200 μg of 10-nm MNPs were administered to 5×10^5 cells. Scale bar: 50 μm. Reprinted with Permission. Copyright 2015 American Chemical Society.

Fig. 2.2 shows an optical microscopic image of MSTO-211H cells incubated for 24 h without MNPs. A mixture of spindle-like cells (mainly in Fig. 2.2A) and polygonal cells (partly in Fig. 2.2A), which is characteristic of biphasic mesothelioma MSTO-211H cells, was observed. The spindle-like cells formed multilayers and were in cell-cell contact. In contrast, after 24 h of incubation with 200 μg of MNPs, some of the MSTO-211H cells shrunk to a needle like shape. MSTO-211H cells treated with MNPs were confirmed to have lower adhesive capacity than the

control cells (Fig. 2.2B). In contrast, no morphological differences were observed between MCF-7 cells incubated without (Fig. 2.2C) and with 200 μg of MNPs (Fig. 2.2D). At a high dose (800 μg) of MNPs, more MSTO-211H cells appeared shrunken than at a dose of 200 μg, although the large number of MNPs rendered observation difficult. It should be noted that, prior to the addition of MNPs, the MSTO-211H cells were in satisfactory condition for experiments, based on the results shown in Fig. 2.3. The number of MSTO-211H cells was kept almost constant at the incubation time from 0 to 24 h, then increased drastically at the incubation time between 24 and 48 h (Fig. 2.3A). This cell-growth behavior suggests that these cells were normal and healthy and the experiment was carried out at the proper period in the cell cycle. As shown Fig. 2.3B, the actin stress fibers existed throughout the cell before the addition of MNPs, suggesting that the cell condition is preferable to the experiment.

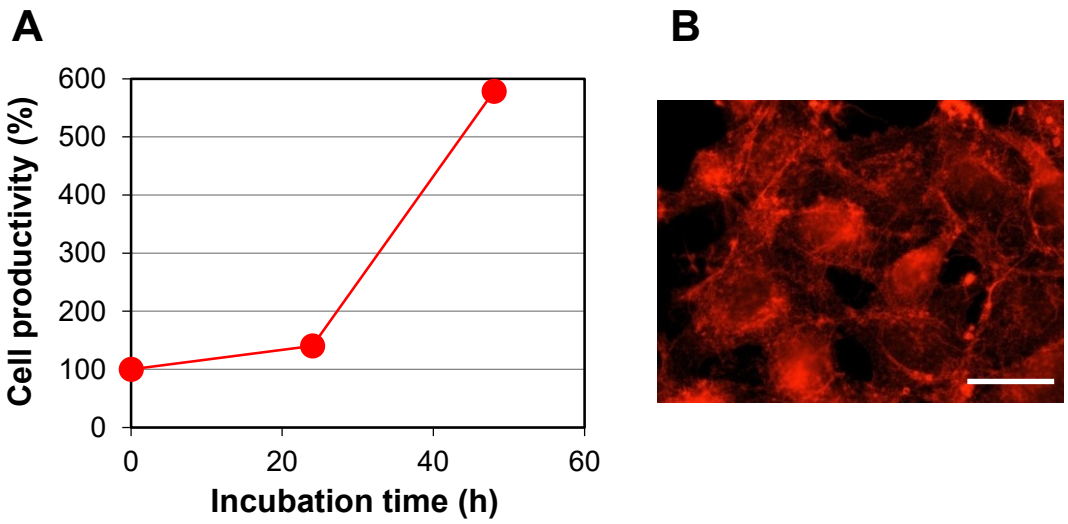

Fig. 2.3 Characterization of MSTO-211H cells without the addition of MNPs: the incubation time-dependence of cell productivity (A) and the fluorescent image of rhodamine phalloidin stained cells (B). Scale bar 25 μm.

Since the shrinkage of human mesothelioma MSTO-211H cells following the addition of MNPs was observed, unlike other cell types in the previous studies [1,2,19], the specific cytotoxic effect of MNPs on mesothelioma cells was then investigated. Fig. 2.4A shows the dose dependence of the percentage of non-viable cells, as evaluated by flow cytometry, with the

addition of 0, 200, 400, 600, and 800 μg of MNPs to mesothelioma NCI-H28, NCI-H2052, and MSTO-211H cells and breast cancer MCF-7 cells (5×10^5 cells for each treatment). Dose-dependent cell death was observed in MSTO-211H cells; at a dose of 200 μg, 20% non-viable cells were observed, reaching 50% at a dose of 800 μg. In contrast, the percentage of non-viable MCF-7 cells remained constant (4%) at doses ranging from 0 to 800 μg. It should be noted here that, among the mesothelioma cells, the response of epithelioid NCI-H28 and sarcomatoid NCI-H2052 cells differed from that of biphasic MSTO-211H cells. The percentage of non-viable NCI-H28 cells remained almost constant, as low as 10%, at doses ranging from 0 to 800 μg, whereas the percentage of non-viable NCI-H2052 cells slightly but gradually increased with the dose, from 5% at a dose of 200 μg to 15% at doses of 600 μg and 800 μg. As mentioned in detail in next chapter, cellular uptake of MNPs induces slight cell damage such as the change of intracellular ROS and cell cycle distribution, which caused a little higher cell mortality of NCI-H2052 cells than NCI-H28 and MCF-7 cells. The dependence of cell death on the incubation time was also investigated in MSTO-211H cells, at a dose of 800 μg MNPs as shown in Fig. 2.5. The percentage of non-viable MSTO-211H cells gradually increased with the incubation time, from 5% at 2 h to 50% at 24 h; the percentage of non-viable control cells, without MNPs, remained below 8% with incubation times ranging from 2 h to 24 h.

Fig. 2.4B shows the ratio of the number of cells containing MNPs to the total number of cells, as evaluated by flow cytometry, under conditions similar to those in Fig. 2.4A. The percentage of cells containing MNPs was shown to increase gradually as the MNPs dose increased for both MSTO-211H and MCF-7 cells; it reached 70% and 90% for MSTO-211H and MCF-7 cells, respectively, at a dose of 800 μg of MNPs. The percentage of NCI-H28 and NCI-H2052 cells containing MNPs, in contrast, reached 80% even at a dose as low as 200 μg.

As a check of the interaction between MNPs and normal cells, the effect of addition of MNPs on human umbilical vein endothelial cells (HUVEC) was also investigated. As a result, although the percentage of uptake was 80%, no more than 10% cell mortality wad observed at doses ranging from 0 to 800 μg. Therefore, it was suggested the possibility that MNPs are safe to normal cells.

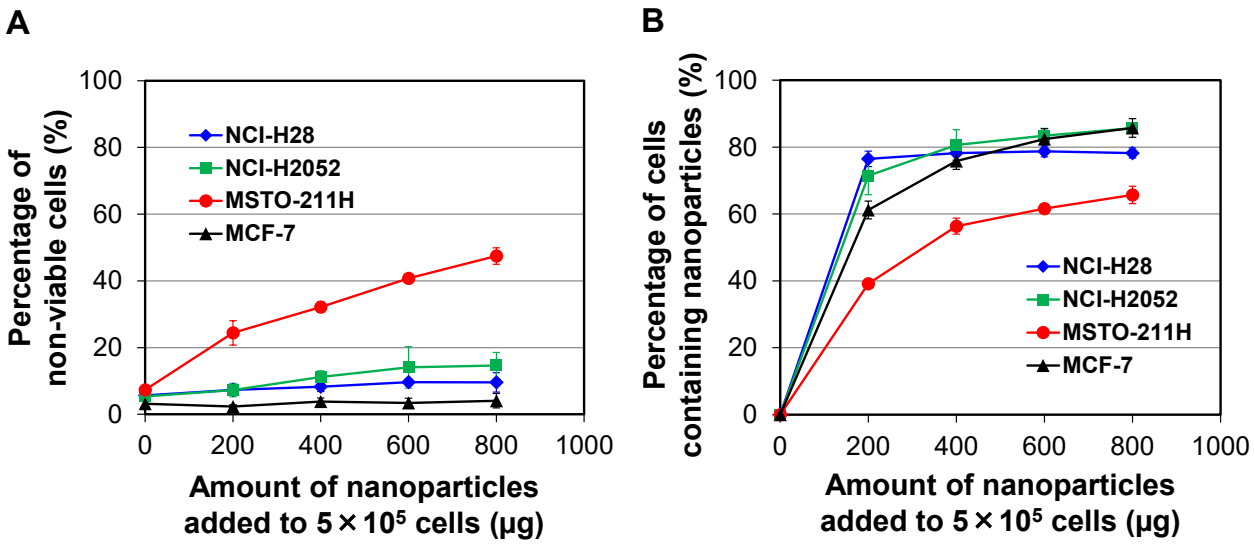

Fig. 2.4 Dependence of the percentage of non-viable cells (A) and the percentage of cells containing MNPs (B) on the amount of 10-nm MNPs added to 5 × 10^5 NCI-H28 cells (diamonds), NCI-H2052 cells (squares), MSTO-211H cells (circles), and MCF-7 cells (triangles). Reprinted with Permission. Copyright 2015 American Chemical Society.

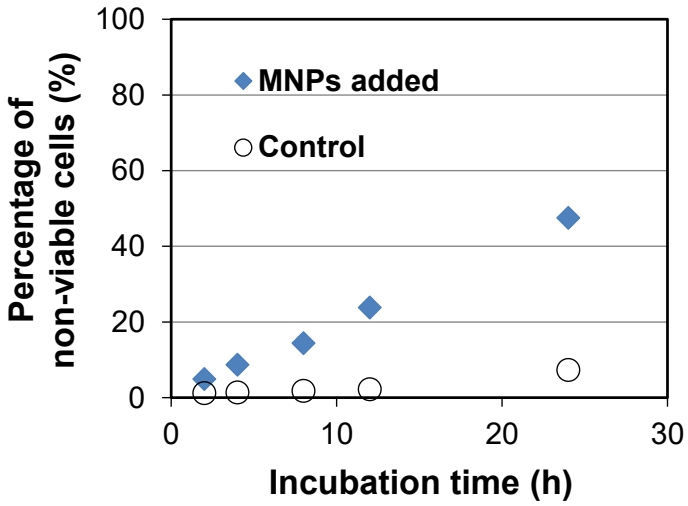

Fig. 2.5 Dependence of the percentage of non-viable MSTO-211H cells on the incubation time at a dose of 800 μg of MNPs (diamonds) and without MNPs (circles) in 5 × 10^5 cells.

To understand the cellular uptake of MNPs in more detail, the state and amount of MNPs incorporated in a single cell for the three types of mesothelioma cells were examined. TEM images (Fig. 2.6) revealed that (i) MNPs were incorporated into cells as aggregates and (ii) MNPs were not present in the nucleus but were present in the cytoplasmic endoplasmic reticulum in all three types (A: epithelioid NCI-H28, B: sarcomatoid NCI-H2052, and C: biphasic MSTO-211H cells). The images shown in Fig. 2.6 are representative of multiple TEM images not shown here for each cell types. These results are similar to previous observations for human breast cancer MCF-7 cells [3]. On the other hand, several differences were observed among the three histological types, e.g. in the size of the vesicles (endosomes) containing the MNPs and the density of MNPs in these vesicles. Fig. 2.7 shows the dose dependence of the uptake of MNPs by mesothelioma cells. In all three mesothelioma cell types, the quantity of MNPs incorporated per cell increased linearly with the dose of MNPs; 150 pg and 650 pg of MNPs were incorporated per cell at doses of 200 μg and 800 μg, respectively.

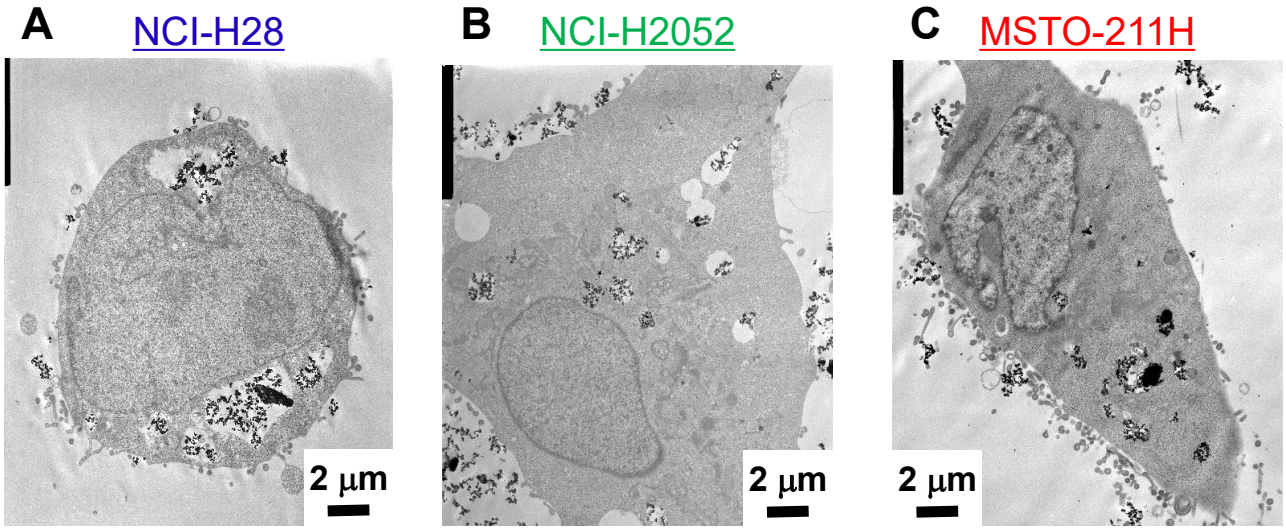

Fig. 2.6 TEM images of a NCI-H28 cell (A), a NCI-H2052 cell (B), and a MSTO-211H cell (C) containing MNPs. Reprinted with Permission. Copyright 2015 American Chemical Society.

It should be noted that the percentage of cells containing MNPs increased with the MNPs dose not only in MSTO-211H but also in MCF-7, NCI-H28, and NCI-H2052 cells (Fig. 2.4), and the

amount of MNPs incorporated per cell increased linearly with the dose for all three types of mesothelioma cells (Fig. 2.7). Thus, the cytotoxic effect of MNPs appears to be specific to biphasic mesothelioma cells. Brunner et al. investigated the *in vitro* cytotoxicity of oxide nanoparticles using MTT and Hoechst assays, and showed that MSTO-211H cells were highly sensitive to Fe_2O_3, while 3T3 cells were not greatly affected [20]. Although they speculated that the high sensitivity of MSTO compared to 3T3 cells could be attributed to a higher phagocytotic activity of MSTO cells than that of 3T3 cells, the reasons for this cell type-specific response remain unclear. This study is the first to find that MNPs show distinct *in vitro* cytotoxicity in MSTO-211H (biphasic) cells, among three histologic mesothelioma subtypes. From Fig. 2.4A and B, although the percentage of non-viable cells tended to be lower than that of MNPs-containing cells, both percentages gradually increased as the dose increased, suggesting a certain relationship between cell death and cellular uptake of MNPs.

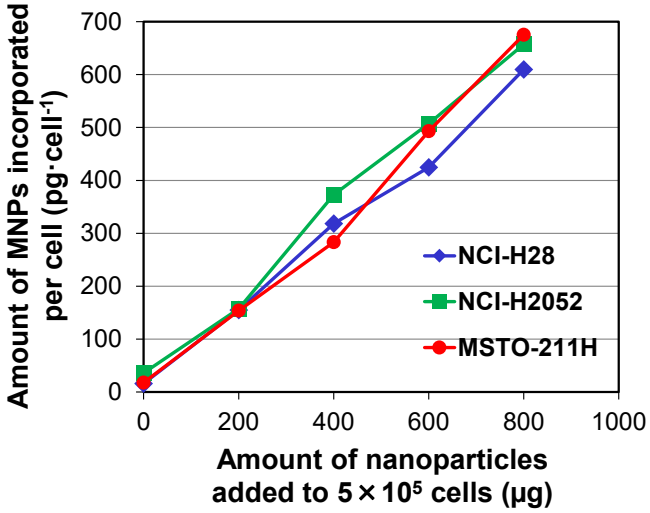

Fig. 2.7 Dependence of the amount of MNPs incorporated per cell on the amount of 10-nm MNPs added to 5 × 10^5 NCI-H28 cells (diamonds), NCI-H2052 cells (squares), and MSTO-211H cells (circles). Reprinted with Permission. Copyright 2015 American Chemical Society.

Next, the mode of cell death was investigated. Fig. 2.8 shows the results of the DNA fragmentation assay. Following agarose gel electrophoresis, DNA laddering was observed for

MSTO-211H cells incubated with MNPs (Lane 3), whereas control MSTO-211H cells without addition of MNPs did not show either laddering or smearing (Lane 2). This result provides evidence for the occurrence of apoptotic DNA fragmentation in MSTO-211H cells after incubation with MNPs. The appearance of DNA ladders is related to the endonuclease activation with subsequent cleavage of DNA into nucleosomal fragments.

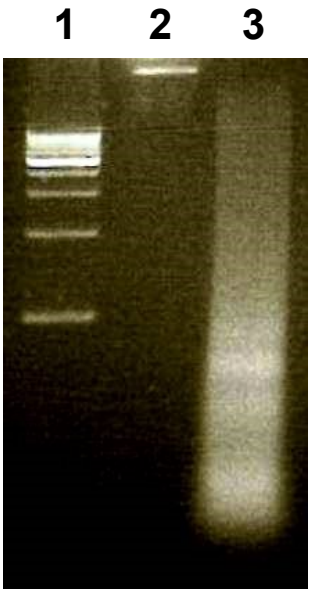

Fig. 2.8 DNA fragmentation analyzed by 1.2% agarose gel electrophoresis: the 1-kb DNA ladder marker (Lane 1), control MSTO-211H cells without addition of MNPs (Lane 2), and MSTO-211H cells after 24 h of incubation with 10-nm MNPs (Lane 3). Reprinted with Permission. Copyright 2015 American Chemical Society.

To consider why only MSTO-211H cells showed high rates of cell death, differences in gene expression between without and with the addition of MNPs in three types of mesothelioma cells were examined. As shown in Fig. 2.9, transforming growth factor-beta2 (TGF-β2) was observed to overexpress specifically in MSTO-211H cells; 43-fold up-regulation of TGF-β2 was observed in MSTO-211H cells treated with MNPs, whereas TGF-β2 expression was unaltered by addition of MNPs in NCI-H28 and NCI-H2052 cells. TGF-β2 is reported to have physiological activities including induction of apoptosis, involving generation of reactive oxygen species (ROS) [21,22].

Schuster et al. explained that the apoptotic process is accompanied by two phases of generation of ROS: a rapid and a delayed phase after TGF-β administration, in the reference [21] and Yao et al. demonstrated experimentally that TGF-β2-induced apoptosis in human lens epithelial cells is preceded by an enhancement in ROS production in the reference [22]. Therefore, the specific cell death to MSTO-211H is considered to associate with the ROS generation. Hence detecting ROS using a Total ROS Detection Kit (Enabling Discovery in Life Science®) was carried out in this study, but failed; valid data to discuss the difference in ROS generation among cell types have not been obtained yet unfortunately. It should be noted that the mode of cellular uptake and the intracellular location and state of incorporated MNPs, observed by TEM (Fig. 2.6), were similar in all three histological types. Therefore, the overexpression of TGF-β2 caused by the addition of MNPs is suggested to result in the induction of apoptosis specific to MSTO-211H cells. Although the reason for cell-type specific overexpression of TGF-β2 has not been elucidated, it is interesting to note that Khan et al. reported that uptake of MNPs affects the TGF-β signaling pathway in HeLa cells [23]. There is else a literature that iron oxide nanoparticles induce ROS formation, which disrupts the actin cytoskeleton and alters endothelial cell morphology and mechanics, as well as induction of cell death [24]. In this study also, the decrease in the amount of actin stress fiber and the change of their morphology were observed for MNPs-added cells (Fig. 2.10), as compared with control cells as shown in Fig. 2.3B.

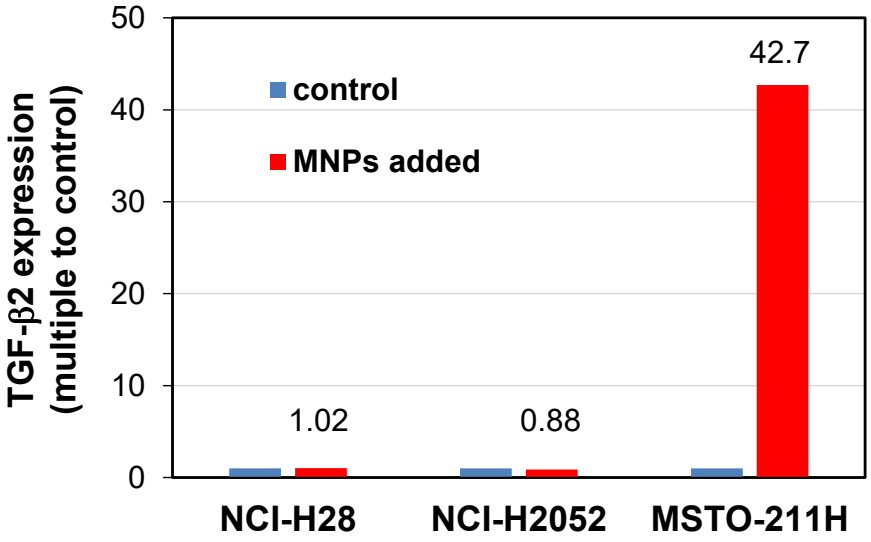

Fig. 2.9 Expression level of TGF-β2 in all three histological types of human mesothelioma cells (NCI-H28, NCI-H2052, and MSTO-211H) cultured without and with 10-nm MNPs. The control signal intensity was set to "1." Reprinted with Permission. Copyright 2015 American Chemical Society.

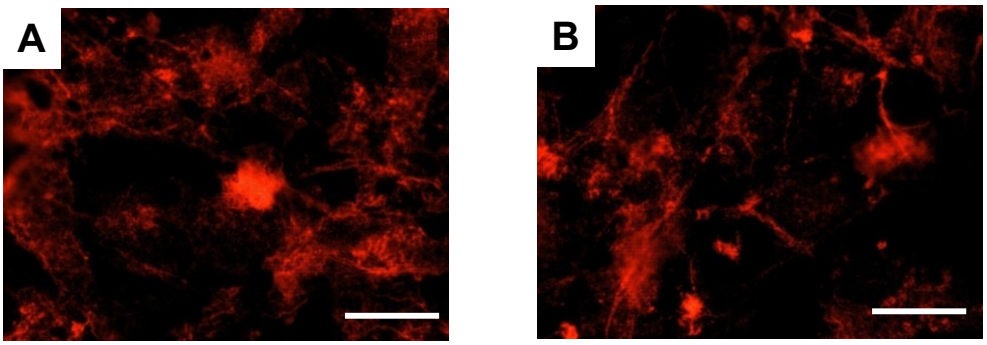

Fig. 2.10 Rhodamine Phalloidin stained mesothelioma MSTO-211H cells after 24-h incubation with MNPs at the dose of 200 μg (A) and 800 μg (B). Scale bar 25 μm.

2.5 Exposure of cells containing nanoparticles to alternating magnetic field

40-nm MNPs were employed here because ferromagnetic MNPs with a diameter of 40 nm were shown to be much more effective for inducing cell death of MCF-7 cells, by their heat generation under an AC magnetic field (325 kHz, 500 Oe), than superparamagnetic MNPs with a diameter of 10 nm in the previous paper [1].

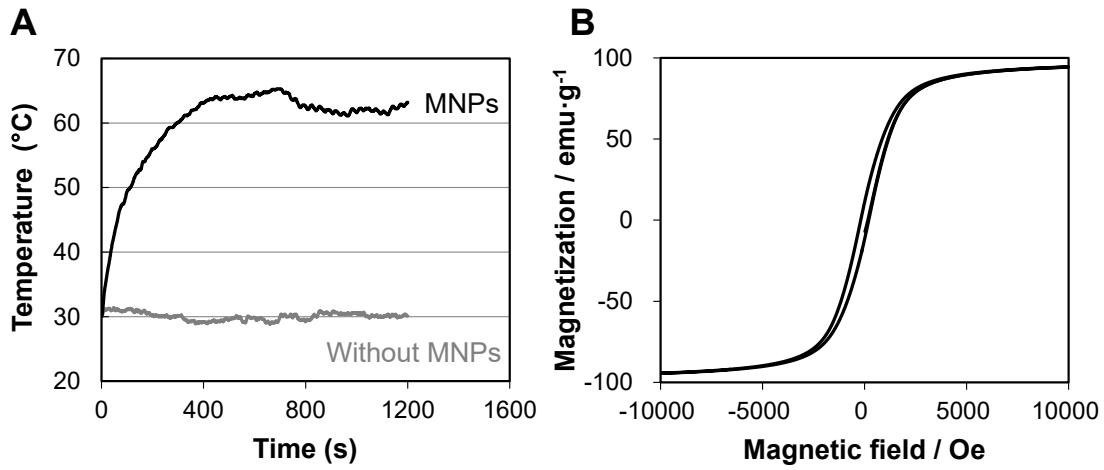

Fig. 2.11 Time dependence of the temperature curve of 1 mg MNPs dispersed in 500 μL of water under an AC magnetic field (325 kHz, the strength was calculated to be 500 Oe) (A) and a magnetization curve of MNPs at the magnetic field of -10000 to 10000 Oe at 300 K (B).

At first, characterization of 40-nm MNPs in terms of heating capacity was investigated. Fig. 2.11A shows the time dependence of temperature reached under AC magnetic field and the field dependence of magnetization at 300 K. Average temperature reached at the exposure time during 800 – 1200 s and the SAR at the time of 100 s were calculated to be 63°C and 792 W/g for a liquid sample. From the magnetization curve as shown in Fig. 2.11B, 40-nm MNPs was observed to show ferromagnetic behavior with a magnetization at 10000 Oe of approximately 90 emu/g and a coercivity of 200 Oe. The temperature rise of 40-nm MNPs in solid matrix under alternating magnetic field was also investigated. In solid condition, physical rotation of nanoparticles is restricted, consequently occurs no Brownian relaxation. However, the SAR of solid sample at the

time of 100 s, which was calculated to be 1076 W/g, is similar to that of liquid sample. Therefore, it is suggested that this MNPs generate heat steadily in a solid such as intracellular environment because the heat is produced by hysteresis loss, not Brownian relaxation.

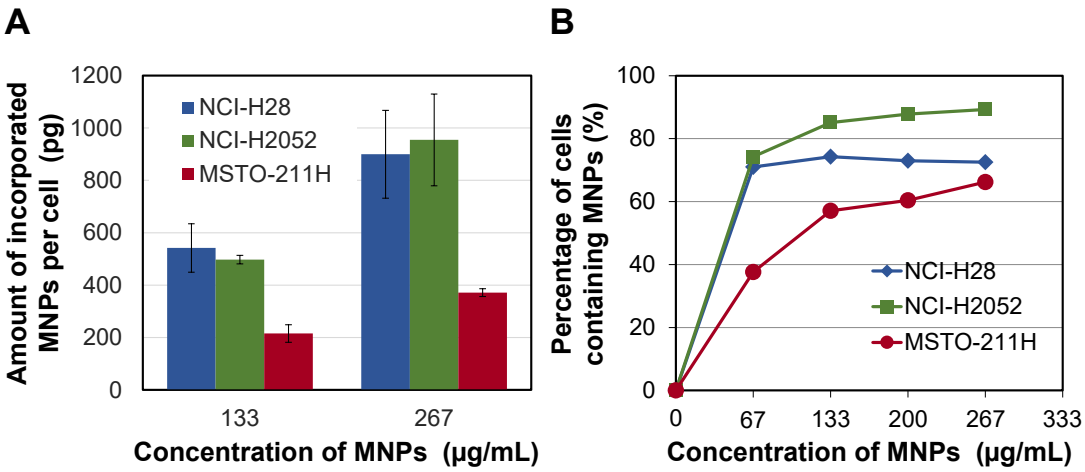

Fig. 2.12 Amount of MNPs incorporated by a NCI-H28 (blue), NCI-H2052 (green), and MSTO-211H (red) cell at the MNPs concentrations of 133 and 267 μg/mL (A), and the percentage of cells containing MNPs at the concentrations of 67, 133, 200, and 267 μg/mL (B).

Fig. 2.12A shows uptake amount of MNPs into a cell. The dependence on MNPs concentration was observed in all types of mesothelioma cells, but those values were different among each types. At the concentration of 133 or 267 μg/mL, 500 or 900 pg of MNPs was incorporated into a NCI-H28 and NCI-H2052 cell, whereas 200 or 400 pg was incorporated into a MSTO-211H cell, respectively. Referring to the previous paper [3], cellular uptake seems to occur via the adsorption of nanoparticles onto cells with attractive forces between positive charge of MNPs (the zeta potential was +16.8 mV) and negative charge of cell surface. Fig. 2.12B shows the percentage of cells containing MNPs analyzed with flow cytometry. Uptake percentage increased with an increase in MNPs concentration for MSTO-211H, it was 40% at 67 μg/mL and reached 70% at 267 μg/mL. On the other hand, 70% of NCI-H28 and NCI-H2052 cells contained MNPs at the concentration of 67 μg/mL. At 267 μg/mL, uptake percentage showed 70% for NCI-H28 and

90% for NCI-H2052, respectively. This tendency, which is the dose dependence of uptake percentage, corresponded with not only the tendency of uptake amount shown in Fig. 2.12A but also the tendency of the percentage of cells containing 10-nm MNPs as shown in Fig. 2.4B.

Next, the cells containing MNPs were subjected to AC magnetic field whose strength of magnetic field was calculated to be 500 Oe at a frequency of 325 kHz for 20 min in all cell types of mesothelioma. The average temperature during 800 – 1200 s in the vicinity of the cells containing MNPs was shown in Table 2.1. Although the temperatures of cells cultured without MNPs maintained 30°C in whole exposure time, the dose dependence of temperature rise was observed in all types of mesothelioma cells containing MNPs, suggesting intracellular heating by 40-nm MNPs. The reached temperature was different among histological types because the intracellular amount of MNPs was also different for each cell types as shown in Fig. 2.12A.

Table 2.1 Average temperature between 800 and 1200 s in the vicinity of the cells containing MNPs under AC magnetic field (325 kHz, 500 Oe) for 20 min.

Dose (μg/mL)	Average Temperature(°C)		
	NCI-H28	NCI-H2052	MSTO-211H
0	31±1	32±1	31±1
133	42±1	46±1	35±1
267	51±1	56±1	40±1

To investigate the effect of intracellular heating by MNPs on death of mesothelioma cells, the cell mortality induced by heat generated from MNPs was compared with that induced by thermostatic bath. In thermostatic water bath, cell death was induced by extracellular heating. Fig. 2.13 shows the comparison of cell mortality induced by intracellular heating with extracellular heating in three types of mesothelioma cells. At the MNPs concentration of 267 μg/mL, the percentage of non-viable cells containing MNPs with alternating magnetic field was approximately 95% for NCI-H28, 100% for NCI-H2052, and 90% for MSTO-211H, respectively. On the other hand, at the same condition except for the use of thermostatic bath instead of

alternating magnetic field, cell mortality was lower: approximately 40% for NCI-H28, 50% for NCI-H2052, and 30% for MSTO-211H. At 133 μg/mL, the mortality was lower than those for 267 μg/mL although, higher cell mortality was also observed for intracellular heating than extracellular heating in all cell types. There is a literature that "intracellular" is effective because the cell membrane works as an excellent thermal barrier and a very poor thermal conductor [25], which suggested that the temperature in the cells is higher than the observed temperature (temperature of suspension). As mentioned in the section 2.4, cellular uptake of MNPs causes slight cell damage such as the change of intracellular ROS and cell cycle distribution. Consequently, the cells then become more sensitive to intracellular heat. It should be noted that intracellular heating by MNPs internalized into cells was found to induce cell death effectively in all cell types of mesothelioma.

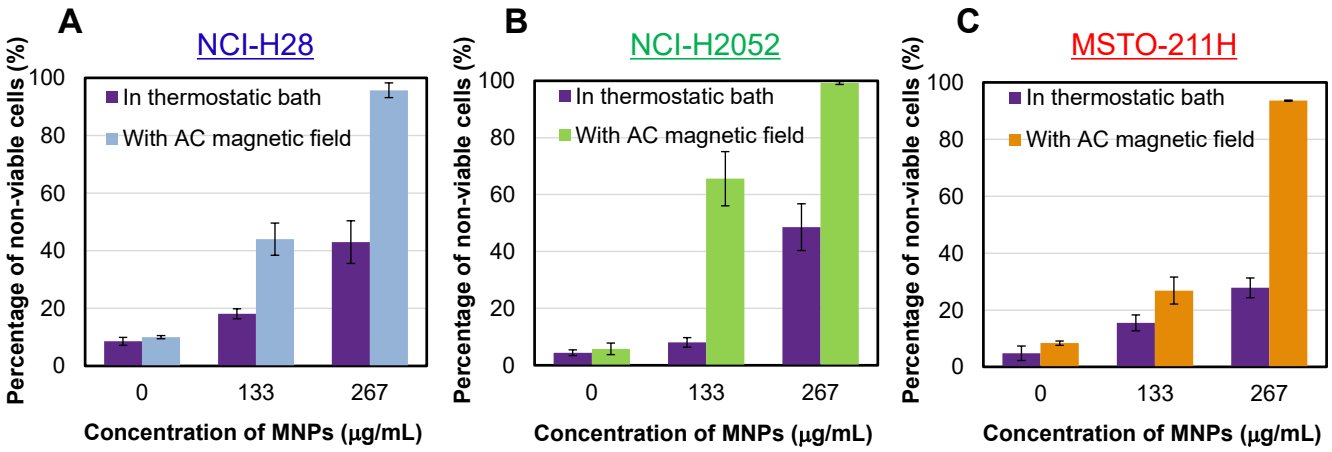

Fig. 2.13 The percentage of non-viable NCI-H28 (A), NCI-H2052 (B), and MSTO-211H (C) at the MNPs concentrations of 0, 133, and 267 μg/mL. "In thermostatic bath (purple bars)" means without AC magnetic field, but those temperatures are set on the average temperature between 800 and 1200 s shown in Table 2.1 using a water bath. Other bars indicate the data obtained with AC magnetic field (325 kHz, 500 Oe). The cell mortalities in all samples were evaluated immediately after heating.

To further study the cell death with MNPs and alternating magnetic field, the mortality at 24-

h time interval of incubation at 37°C was investigated in all histological types of mesothelioma cells as shown in Fig. 2.14. Here, Fig. 2.14A, B, and C show the percentage of non-viable cells containing MNPs without alternating magnetic field. As observed in Fig. 2.4A, dose-dependent cell death was observed in MSTO-211H cells but not in NCI-H28 and NCI-H2052 cells even after just magnetic separation in Fig. 2.14A-C. The cell-type-specific cell death should also be related to the overexpression of transforming growth factor β2 induced by MNPs as shown in Fig. 2.9.

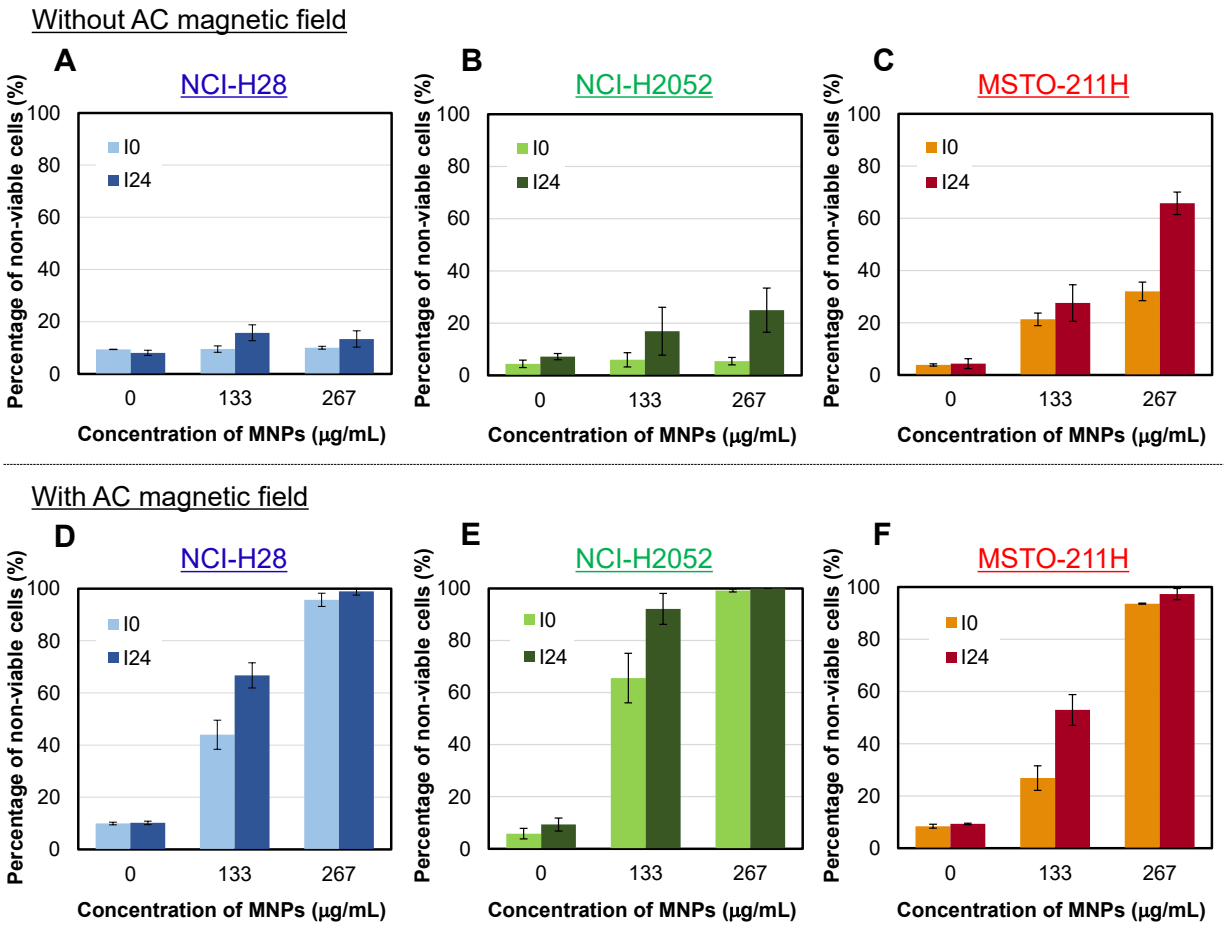

Fig. 2.14 The percentage of non-viable NCI-H28 (A,D), NCI-H2052 (B,E), and MSTO-211H (C,F) at the MNPs concentrations of 0, 133, and 267 μg/mL without (A-C) or with (D-F) an AC magnetic field (325 kHz, 500 Oe). The data shown as "I0" and "I24" means the cell mortalities measured immediately or after 24 h of incubation at 37°C following just magnetic separation (A-C) or exposure to alternating magnetic field (D-F).

Following further 24-h incubation, 1.5 – 2 times of increase in mortality was observed in NCI-H28 and MSTO-211H, whereas the mortality of NCI-H2052 cells was increased by 3 – 5 times. High sensitivity of mesothelioma cells to incorporated MNPs could induce higher mortality. As shown in Fig. 2.4A, the percentage of non-viable cells in the presence of MNPs was compared for three types of mesothelioma cells and human breast cancer MCF-7 cells, resulting that the percentage of all types of mesothelioma cells was >2 times higher than MCF-7 cells.

When the cells after subjecting to alternating magnetic field were further incubated at 37°C for 24 h, the cell mortalities in all condition except for with no MNPs increased as shown in Fig. 2.14D, E, and F, it reached approximately 100% in all three histological types of mesothelioma cells at the MNP concentration of 267 μg/mL.

At the time, cell morphology at the different concentrations of MNPs in three types of mesothelioma cells was also observed by an optical microscopy as shown in Fig. 2.15. With no MNPs, NCI-H28 cells were adhered with elongated spindle shape, NCI-H2052 were adhered with cubic-like or polygonal shape, and MSTO-211H cells were adhered with a mixture of those shapes. On the other hand, cells with MNPs were not adhered and its rate increased with a dose amount in all types of mesothelioma, which corresponded approximately to the percentages of cell death (Fig. 2.13D-F). At 267 μg/mL, approximately 100% of cells were floating with a small spherical shape. In mesothelioma therapy, it is a very significant issue that surviving cancerous cells or tumors resume their proliferation soon after a treatment. However, no standard treatment approaches have been proven to improve survival or control symptoms for a prolonged period of time [26]. Notably, the results from Figs. 2.14 and 2.15 demonstrated that the treatment of exposure of the cells containing MNPs to AC magnetic field has a potential to inhibit the secondary cancer-cell proliferation in all three histological subtypes of mesothelioma *in vitro*, which is suggestive of the recurrence prevention in mesothelioma treatment.

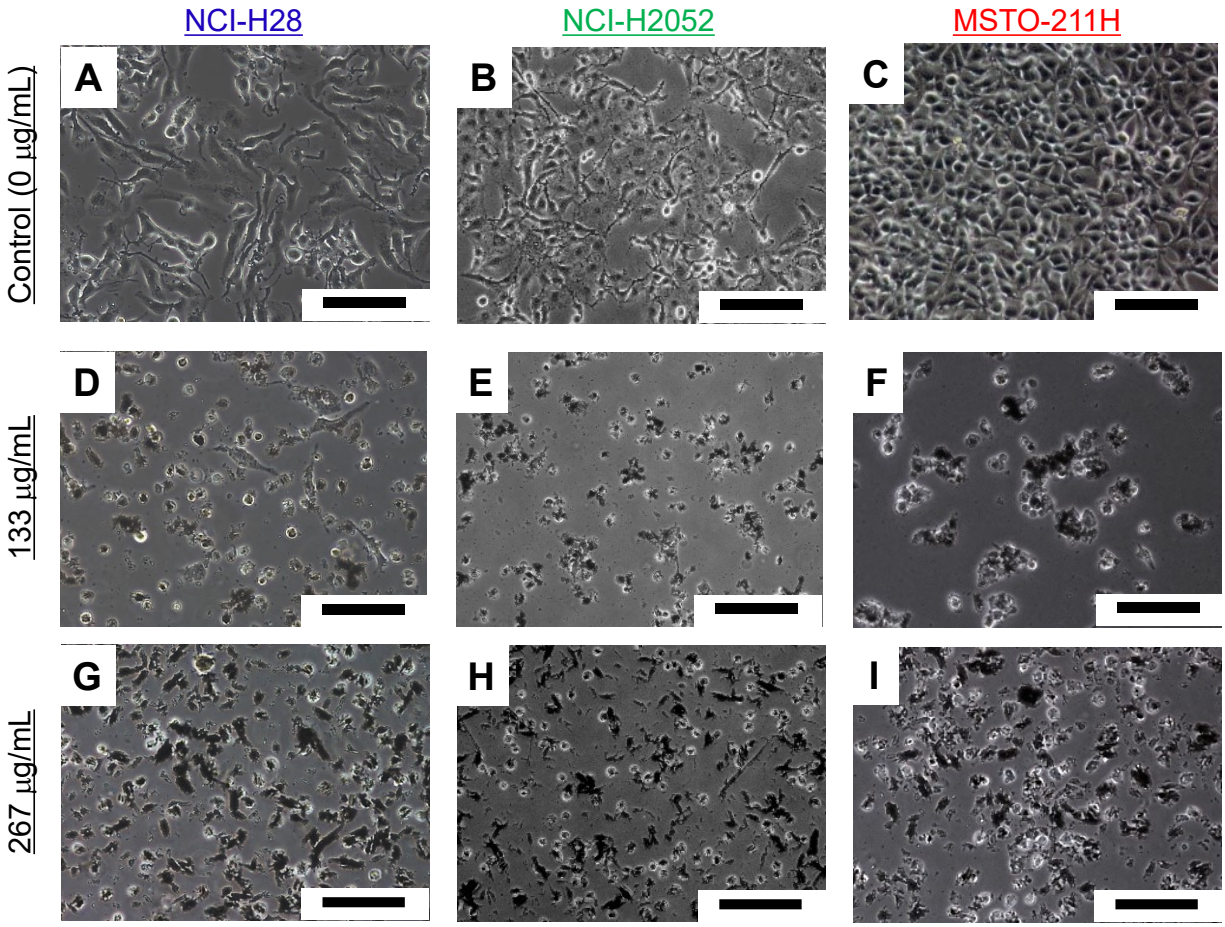

Fig. 2.15 Microscopic images of NCI-H28 (A,D,G), NCI-H2052 (B,E,H), and MSTO-211H (C,F,I) cells with the MNPs concentrations of 0 (A,B,C), 133 (D,E,F), and 267 (G,H,I) μg/mL incubated for 24 h under the condition of 37°C and 5% CO_2 after exposure to alternating magnetic field (325 kHz, 500 Oe). Scale bar: 200 μm.

To consider the influence of intracellular heating with incorporated MNPs on cell death in mesothelioma, the mode of cell death of NCI-H2052 with MNPs subjected to alternating magnetic field was discussed. Fig. 2.16 shows the cell dot plots with PE Annexin V on the x-axis and 7-AAD on the y-axis, as evaluated by flow cytometry. In the plot, viable cells are PE Annexin V and 7-AAD negative (lower left quadrant, Q3), cells that are in early apoptosis are PE Annexin V positive and 7-AAD negative (lower right quadrant, Q4), and cells are in late apoptosis or are already dead are PE Annexin V and 7-AAD positive (upper right quadrant, Q2). Almost all NCI-

H2052 cells without MNPs (Fig. 2.16A,D) located in Q3. NCI-H2052 cells with MNPs immediately after the magnetic field exposure located in Q3 and Q2, which is indicative of the induction of necrosis (Fig. 2.16B,C). In general, cell death by heating is known to be induced by both apoptosis and necrosis via DNA damage in a temperature-dependent manner [27,28]. Compared Fig. 2.16B with E, it was understood that the cell group located in Q3 in Fig. 2.16B right transferred to Q4, which should suggested that apoptosis was undergone in 24-h incubation at 37°C following exposure to alternating magnetic field, but the location of cell group in Q3 in control (Fig. 2.16D) was not altered after 24-h incubation. For NCI-H2052 cells at the concentration of 267 μg/mL, all cells were categorized already dead cells, which is equivalent to the percentages of cell death (Fig. 2.14D-F).

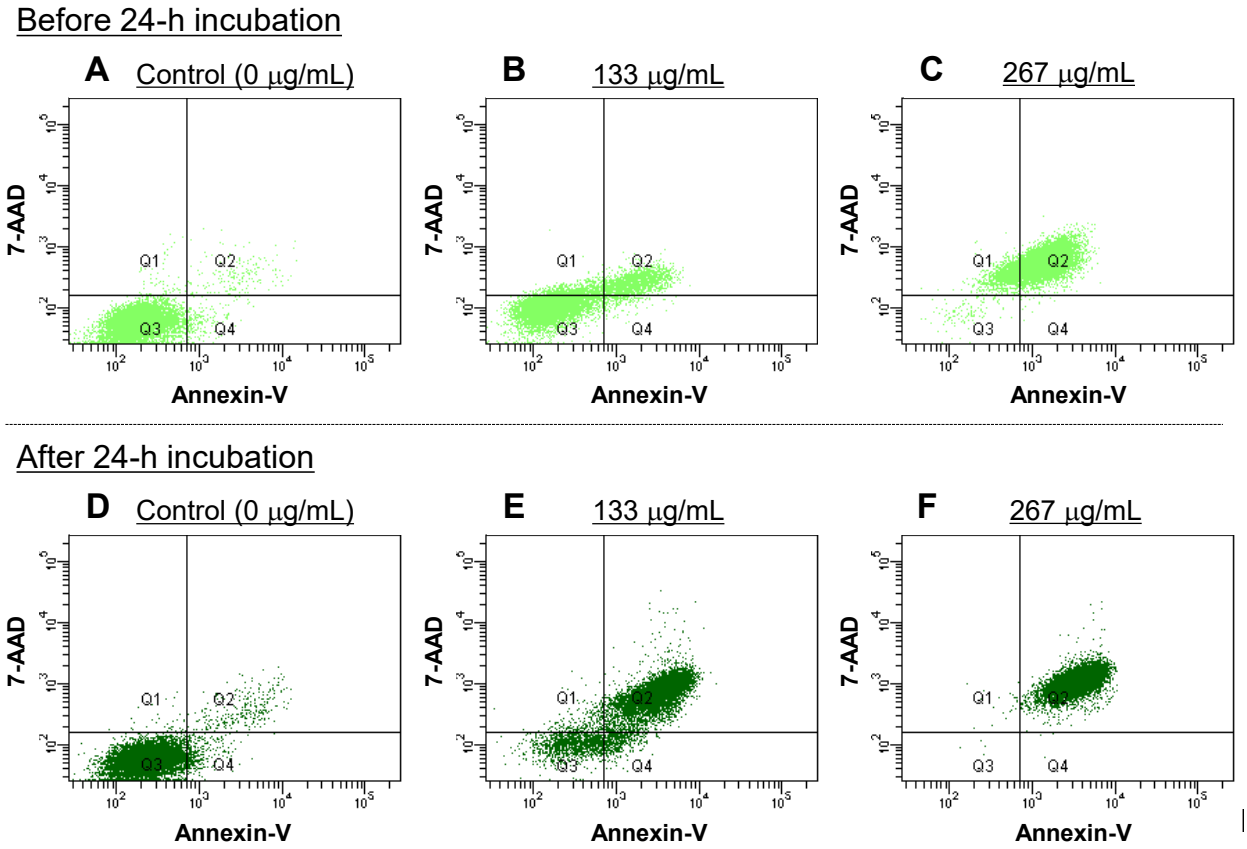

A	Almost all cells are viable.
B	Viable cells and necrotic cells are mixed.
C	Almost all cells are necrotic cells.
D	Almost all cells are viable.
E	Viable cells, necrotic cells, and early apoptotic cells are mixed.
F	All cells are already dead cells.

Fig. 2.16 Detection of apoptotic NCI-H2052 cells with MNPs and with alternating magnetic field (325 kHz, 500 Oe), as evaluated by flow cytometry: upper and lower dot plots shows the data measured immediately (A-C) or after 24 h of incubation at 37°C (D-F) following exposure to alternating magnetic field. The inserted table is the summary of flow cytometric results.

2.6 Conclusion

With an objective to understand the interactions (influence) between nanoparticles and mesothelioma cells, cellular uptake and cytotoxicity of MNPs in three histological types of mesothelioma cells (i.e. epithelioid NCI-H28, sarcomatoid NCI-H2052, and biphasic MSTO-211H), in addition to their cell death induced by MNPs subjected to AC magnetic field were investigated and discussed in this chapter.

As a new finding, cell death by the addition of MNPs was observed in MSTO-211H cells without applying AC magnetic field. Both NCI-H28 and NCI-H2052 cells were not induced death by MNPs. Cellular uptake of MNPs was observed in all cell types. The ratio of the number of cells containing MNPs to the total number of cells was shown to depend on the dose of MNPs, which for MSTO-211H was lower than that for other three cell types. DNA fragmentation and microarray analyses suggested that MNPs induced transforming growth factor-beta2-related apoptosis in MSTO-211H cells.

When AC magnetic field was applied to NCI-H28, NCI-H2052, and MSTO-211H cells containing MNPs, temperature rose under the AC magnetic field, and high rates of cell death were observed in all three histological types of mesothelioma. Furthermore, cell viabilities became much lower (approximately 0%) by letting the cells containing MNPs incubate at 37°C for 24 h after exposure to alternating magnetic field in all cell types. Because higher cell mortality was observed when cells are heated by incorporated MNPs with an alternating magnetic field as compared to thermostatic-bath heating, significance of cellular uptake of MNPs to induce cell death efficiently in mesothelioma has been demonstrated.

The results of the *in vitro* experiments performed in this study demonstrated the potential of MNPs for future application to mesothelioma treatment via the following two approaches: (i) the use of the specific apoptotic effect of MNPs on MSTO-211H cells and (ii) use of heat generation by MNPs subjected to an AC magnetic field, which induced a high degree of cell mortality in all three major histologic subtypes of mesothelioma cells. The 10-nm MNPs could be applied to the former approach, whereas the 40-nm MNPs show particular promise for the latter.

Reference

[1] D. Baba et al., "Effect of magnetite nanoparticles on living rate of MCF-7 human breast cancer cells", *Colloids Surf. B Biointerfaces*, 95, 254 (2012).

[2] H. Iida et al., "Synthesis of Fe_3O_4 nanoparticles with various sizes and magnetic properties by controlled hydrolysis", *J. Colloid Interface Sci.*, 314, 274 (2007).

[3] T. Osaka et al., "Effect of surface charge of magnetite nanoparticles on their internalization into breast cancer and umbilical vein endothelial cells", *Colloids Surf. B Biointerfaces*, 71, 325 (2009).

[4] I. J. Selikoff et al., "Relation between exposure to asbestos and mesothelioma", *N. Engl. J. Med*, 272, 560 (1965).

[5] C. Boutin et al., "Malignant pleural mesothelioma", *Eur. Respir. J.*, 12, 972 (1998).

[6] B. W. S. Robinson et al., "Malignant mesothelioma", *Lancet*, 366, 397 (2005).

[7] M. Kobayashi et al., "Establishment of three novel human malignant pleural mesothelioma cell lines: morphological and cytogenetical studies and EGFR mutation status", *Anticancer Res.*, 28, 197 (2008).

[8] L. Jiang et al., "Iron overload signature in chrysotile-induced malignant mesothelioma", *J. Pathol.*, 228, 366 (2012).

[9] K. Gemba et al., "Treatment and survival analysis of malignant mesothelioma in Japan", *Acta Oncol.*, 52, 803 (2013).

[10] National Cancer Institute, "Malignant Mesothelioma Treatment (PDQ®)–Patient Version".

[11] V. Delgermaa et al., "Global mesothelioma deaths reported to the World Health Organization between 1994 and 2008", *Bull. World Health Organ.*, 89, 716 (2011).

[12] L. Stayner et al., "The Worldwide Pandemic of Asbestos-Related Diseases", *Annu. Rev. Public Health*, 34, 4.1 (2013).

[13] N. Kurumatani and S. Kumagai et al., "Mapping the Risk of Mesothelioma Due to Neighborhood Asbestos Exposure", *Am. J. Respir. Crit. Care Med.*, 178, 624 (2008).

[14] T. Murayama et al., "Estimation of Future Mortality From Pleural Malignant Mesothelioma in Japan Based on an Age-Cohort Model", *Am. J. Ind. Med.*, 49, 1 (2006).

[15] T. Myojin et al., "Future Trends of Mesothelioma Mortality in Japan Based on a Risk Function", *Ind. Health*, 50, 197 (2012).

[16] G. A. DeLaria et al., "Surgical management of malignant mesothelioma", *Ann. Thorac. Surg.*,

26, 375 (1978).

[17] N. J. Vogelzang et al., "Phase III study of pemetrexed in combination with cisplatin versus cisplatin alone in patients with malignant pleural mesothelioma", *J. Clin. Oncol.*, 21, 2636 (2003).

[18] G. Pasello et al., "An overview of neoadjuvant chemotherapy in the multimodality treatment of malignant pleural mesothelioma", *Cancer Treat. Rev.*, 39, 10 (2013).

[19] C. Shundo et al., "Cytotoxicity evaluation of magnetite (Fe_3O_4) nanoparticles in mouse embryonic stem cells", *Colloids Surf. B Biointerfaces*, 97, 221 (2012).

[20] T. J. Brunner et al., "In vitro cytotoxicity of oxide nanoparticles: comparison to asbestos, silica, and the effect of particle solubility", *Environ. Sci. Technol.*, 40, 4374 (2006).

[21] N. Schuster and K. Krieglstein, "Mechanisms of TGF-β-mediated apoptosis", *Cell Tissue Res.*, 307, 1 (2002).

[22] K. Yao et al., "Reactive oxygen species mediates the apoptosis induced by transforming growth factor β2 in human lens epithelial cells", *Biochem. Biophys. Res. Commun.*, 354, 278 (2007).

[23] J. A. Khan et al., "Magnetite (Fe_3O_4) nanocrystals affect the expression of genes involved in the TGF-beta signalling pathway", *Mol. BioSyst.*, 7, 1481 (2011).

[24] K. Buyukhatipoglu and A. M. Clyne, "Superparamagnetic iron oxide nanoparticles change endothelial cell morphology and mechanics via reactive oxygen species formation", *J. Biomed. Mater. Res. A.*, 96, 186 (2010).

[25] R. T. Gordon et al., "Intracellular hyperthermia. A biophysical approach to cancer treatment via intracellular temperature and biophysical alterations", *Med. Hypotheses*, 5, 83 (1979).

[26] National Cancer Institute, "Malignant Mesothelioma Treatment (PDQ®)–Health Professional Version".

[27] B. V. Harmon et al., "Cell death induced in a murine mastocytoma by 42–47°C heating *in vitro*: evidence that the form of death changes from apoptosis to necrosis above a critical heat load", *Int. J. Radiat. Biol.*, 58, 845 (1990).

[28] B. Hildebrandt et al., "The cellular and molecular basis of hyperthermia", *Crit. Rev. Oncol. Hematol*., 43, 33 (2002).

Chapter 3

Effect of cellular uptake of Fe_3O_4 nanoparticles (MNPs) on breast cancer cell death *in vitro* and surface design of MNPs for *in vivo* application in melanoma

3.1 Introduction

In section 3.2, to confirm the importance of cellular uptake for effective magnetic hyperthermia, the influence of the location of nanoparticles (i.e., intracellular or extracellular) on cell condition was investigated in breast cancer cells. In section 3.3, surface design (functionalization) as well as control of magnetic properties of Fe_3O_4 nanoparticles to show therapeutic effect to melanoma tumors was discussed. Breast cancer and melanoma were employed since magnetic hyperthermia can, in principle, be easily applied to tumors located on/under the human skin. Melanoma was used into mice because the method of making tumor has been established.

In 1979, Gordon et al. demonstrated *in vivo* for the first time that the intracellular heating using submicron iron oxide particles was more effective than extracellular heating in magnetic hyperthermia because the cell membrane works as an excellent thermal barrier and a very poor thermal conductor [1]. After that, the effectiveness of intracellular heating with the use of magnetic nanoparticles that were internalized by cells has been further discussed *in vitro* [2-5]. Although the ref. [2] and [3] said that there was no difference in the thermal sense between two systems of heating methods, the intracellular heating led to enhanced reduction in cell viability rather than the extracellular heating in the ref. [4] and [5]. Also in the chapter 2, the intracellular heating by magnetite nanoparticles induced death of three histological subtypes of mesothelioma cells effectively. In this situation, two systems consisting of human breast cancer MCF-7 cells and 40-nm magnetite nanoparticles (MNPs) was investigated in the section 3.2: the one is the cells with MNPs addition, and the other is the cells pre-cultivated for 24 h in the presence of MNPs. The former essentially contains extracellular MNPs, and the latter contains both intracellular and extracellular MNPs. A comparison of the two systems should be meaningful considering actual

situation. By comparing two systems, the effect of intracellular and extracellular MNPs on MCF-7-cells condition was examined, in view of influence associated with cellular uptake of MNPs. In addition, the effect of the heating with MNPs exposed to alternating magnetic field on cell death was compared with that of the heating by thermostatic water bath.

From the results of chapter 2 and section 3.2, the significance of cellular uptake of MNPs to induce cell death efficiently has been demonstrated *in vitro*. In section 3.3, taking advantage of the *in vitro* results, *in vivo* application of MNPs with designed surface property and controlled magnetic property was investigated. This study is the collaboration research with Catholic University of Korea (Prof. Kun Na group).

In the control of magnetic property of MNPs, considering to using AC magnetic field with a frequency of 112 kHz with a strength of magnetic field of 250 Oe, superparamagnetic 10-nm MNPs were employed in this study. If ferromagnetic 40-nm MNPs are used as a heat generator at this applied condition, heat could not be generated efficiently. Because the coercivity of 40-nm MNPs is higher than the strength of effective magnetic field applied, their magnetization reversal rarely occurred.

In the surface design of MNPs, to increase of therapeutic efficacy associated with increase in cellular uptake, the selectivity to cancer cells were modified on the surface of MNPs. Recently, there are many reports of surface modification of MNPs with a cancer-selective molecule [6-18]. R. Rastogi et al. reported folate conjugated iron oxide nanoparticles for targeting cancer cells [8]. Folate receptor is known to be overexpressed on many of cancer tumor cells [6-8]. However, folate conjugated nanoparticles are incorporated into normal cells because normal cells also possess folate receptor. On the other hand, T. Chen et al. reported the aptamer conjugated Fe_3O_4 nanoparticles [11], of which aptamer (single-oligonucleotide chain) can specifically bind to the receptor located on cancer cells [11-13]. Although specific to cancer cells, there is a concern of ambiguous *in vivo* kinetics. Based on these backgrounds, hyaluronic acid (HA) was employed in this study, since HA has advantages of (i) high biocompatibility [14], (ii) high hydrophility [15], and (iii) high cancer tumor targeting efficacy [16,17]. HA can bind specifically bind to the HA receptor (CD44) located on cancer cells such as melanoma. In this study, HA was acetylated in

order to become lower its solubility [15].

Furthermore, to increase in therapeutic efficacy, pheophorbide-a (a photodynamic therapeutic agent; PheoA) was modified onto MNPs. PheoA generates reactive oxygen species when exposed to the light with a wavelength of 671 nm [15]. In this study, magnetic hyperthermia combined with photodynamic therapy discussed. Although drug delivery system is generally selected as the other therapy in magnetic hyperthermia combined with other therapy [8,11], this study focused on photodynamic therapy due to their ability of not only treatment but also imaging using fluorescence of PheoA.

Overall, superparamagnetic 10-nm MNPs which modified with PheoA-conjugated acetylated hyaluronic acid (AHP@MNPs) were designed to achieve effective treatment of cancer.

3.2 Influence of intracellular and extracellular nanoparticles *in vitro*

3.2.1 Experimental

Synthesis of magnetite nanoparticles

MNPs with a diameter of 40 nm were synthesized from ferrous chloride ($FeCl_2 \cdot 4H_2O$) and 1,6-hexanediamine ($H_2N(CH_2)_6NH_2$) as reported in the paper [18]. Both chemicals were purchased from Kanto Chemical Co., Inc. Briefly, 100 mL of an aqueous solution containing 0.05 mol/L of ferrous chloride was mixed with 100 mL of an aqueous solution containing 0.25 mol/L of 1,6-hexanediamine, and the mixture was stirred for 24 h at room temperature. Afterwards, the black precipitates were washed with ultrapure water and ethanol, and vacuum dried to make them powder before use in other experiments.

MCF-7 cell cultivation

MCF-7 cells were cultured in Eagle's minimum essential medium (EMEM; Sigma-Aldrich) with 10% fetal bovine serum (FBS; Thermo Fisher Scientific), 5% L-glutamine (Invitrogen), 1% MEM non-essential amino acid (Gibco), and 1% antibiotic-antimycotic (Gibco). The cells were incubated at 37°C in an atmosphere with 5% CO_2.

Preparation of two systems consisting of cells and MNPs for comparison

Two systems consisting of MCF-7 cells and MNPs were prepared: the one is the cells with MNPs addition (hereinafter referred to as "simply-added" system), and the other is the cells pre-cultivated for 24 h in the presence of MNPs (hereinafter referred to as "pre-cultivated" system).

Regarding the "simply-added" system, a 500-μL suspension containing a mixture of cells and MNPs was prepared with adding 0, 125, or 250 μg of MNPs to 5×10^5 MCF-7 cells suspended in the medium using the 1.5-mL microtube.

As for the "pre-cultivated" system, MCF-7 cells were seeded in a 6-well dish at a density of 5×10^5 cells per 3 mL of medium in each well and then cultivated with MNPs at the dose of 0,

125, or 250 μg per well for 24 h at 37°C. After the pre-cultivation with MNPs, cells were harvested by a treatment with 0.25 % trypsin-EDTA. It should be noted that basically neither aspiration nor rinse were performed to avoid the loss of MNPs; the amount of MNPs in this "pre-cultivated" system should be the same as that in the "simply-added" system for comparison. After centrifugation, the whole of MNPs and cells collected was resuspended in 500 μL of medium using the 1.5-mL tube.

Cell cycle analysis and detection of reactive oxygen species after cellular uptake of MNPs

Cell proliferation in the "pre-cultivated" system was investigated by using FlowCellect Bivariate Cell Cycle Kit for DNA Replication Analysis (Millipore) and DNase I reagent (Sigma Aldrich) for flow cytometric analysis. Cells were labeled and stained with bromodeoxyuridine (5-bromo-2'-deoxyuridine, BrdU) and propidium iodide (PI) according to essentially the same protocol as provided by manufacturer (Millipore). BrdU incorporated in newly synthesized DNA in cells was stained with anti-BrdU antibodies conjugated to Alexa Fluor 488 and total DNA in cells was stained by PI/RNase solution. Flow cytometric analysis was performed with a BD FACSCanto II flow cytometer.

The generation of reactive oxygen species (ROS) was detected by using CellROX Green Reagent (Thermo Fisher Scientific). For the evaluation of "pre-cultivated" system, 5×10^5 MCF-7 cells were cultivated with 0, 125, or 250 μg of MNPs for 24 h at 37°C. After removing unincorporated MNPs, 0.5 μL of 2.5 mmol/L CellROX Green Reagent was added. Cells were incubated for 30 min followed by washing three times with DPBS, and then observed with an Olympus BX51 fluorescence microscope. *N*-acetyl-L-cysteine as the ROS inhibitor and pyocyanin as the ROS inducer were used for negative and positive controls, respectively. In contrast, for evaluating "simply-added" system, a 200-μL portion of the 500-μL suspension containing a mixture of 5×10^5 MCF-7 cells and 0, 125, or 250 μg of MNPs was dispensed to a cuvette with slide glass and they were centrifuged (600 rpm, 3 min) with a Thermo Scientific Cytospin 4 cytocentrifuge. The cells on the slide glass were treated with 0.5 μL of 2.5 mmol/L CellROX Green Reagent for 30 min, followed by washing three times with DPBS. The sample on the slide glass was observed with the fluorescence microscope.

Exposure cells with MNPs to an alternating magnetic field

Samples in the 1.5-mL microtubes, which were prepared as described above, were exposed to an alternating magnetic field (AMF) with an output power of 4.3 kW and an electric current of 569.1 A at a frequency of 325 kHz for 20 min, using an Alonics EASYHEAT induction-heating device equipped with a 3-turn coil with an outer diameter of 40 mm. The strength of magnetic field was calculated to be 536 Oe. During the 20-min exposure to the alternating magnetic field, sample temperature was measured with an Anritsu FL-2000 fiber thermometer by inserting the head of an FS600-2M fiber probe into the sample (cell suspension) in the 1.5-mL tube.

Samples in the 1.5-mL microtubes, which were prepared as described above, were also treated at constant temperature for 20 min by being placed in an AS ONE Corporation THERMAL ROBO TR-1A water bath.

Cell mortality immediately or after 24 h of incubation at 37°C following exposure to AMF was evaluated by cell counting with trypan blue (TB; Gibco) staining.

3.2.2 Influence associated with cellular uptake of nanoparticles

To consider how cellular uptake of MNPs affects cellular condition, cell cycle distribution was examined in the "pre-cultivated" system. As shown in Fig. 3.1, the increase and decrease in the percentage of cells in the G1 and S phase, respectively, was observed when incubated in the presence of MNPs. At higher dose of MNPs, the change in the percentage was greater. Thus this change in cell cycle distribution seems to be associated with cellular uptake of MNPs. The cell cycle arrest in the G1 phase, often accompanied by cellular uptake of nanoparticles, has been reported for MNPs in L929 murine fibroblast cells [19] and in A549 human lung adenocarcinoma cells [20].

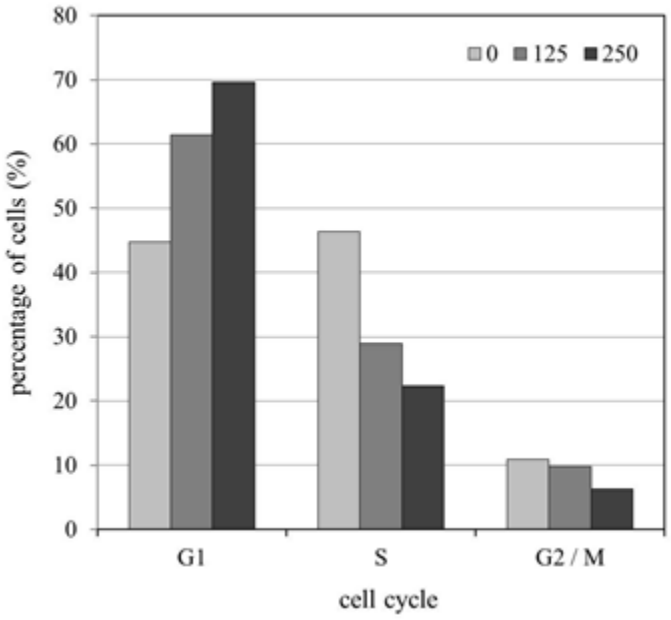

Fig. 3.1 Percentages of cells in G1, S, and G2/M phases for the MCF-7 cells cultivated for 24 h in the presence of 0, 125, and 250 μg MNPs. G1 is the phase of preparation for DNA synthesis (growth), S is the phase of DNA replication, G2 is the phase of preparation for mitosis (growth), and M is the phase of cell division.

Next, intracellular ROS was examined by fluorescence microscopy; the samples for observation were treated with the cell-permeable reagent, which is essentially non-fluorescent

while in a reduced state but exhibits a strong fluorogenic signal upon oxidation. Fig. 3.2 shows bright field (A-C) and fluorescence (D-F) microscopic images of the MCF-7 cells pre-cultivated for 24 h in the presence of MNPs, corresponding to the "pre-cultivated" system. From Fig. 3.2D-F, a change (an increase) in fluorescence intensity was observed for the samples cultivated with MNPs, particularly at higher dose of MNPs. Similar tendency was reported for J774 murine macrophage [21] and for A549 cells [22] with iron oxide nanoparticles.

The change in intracellular ROS as well as cell cycle distribution described above could be evidences for cell injury or damage to some degree resulting from cellular uptake of MNPs.

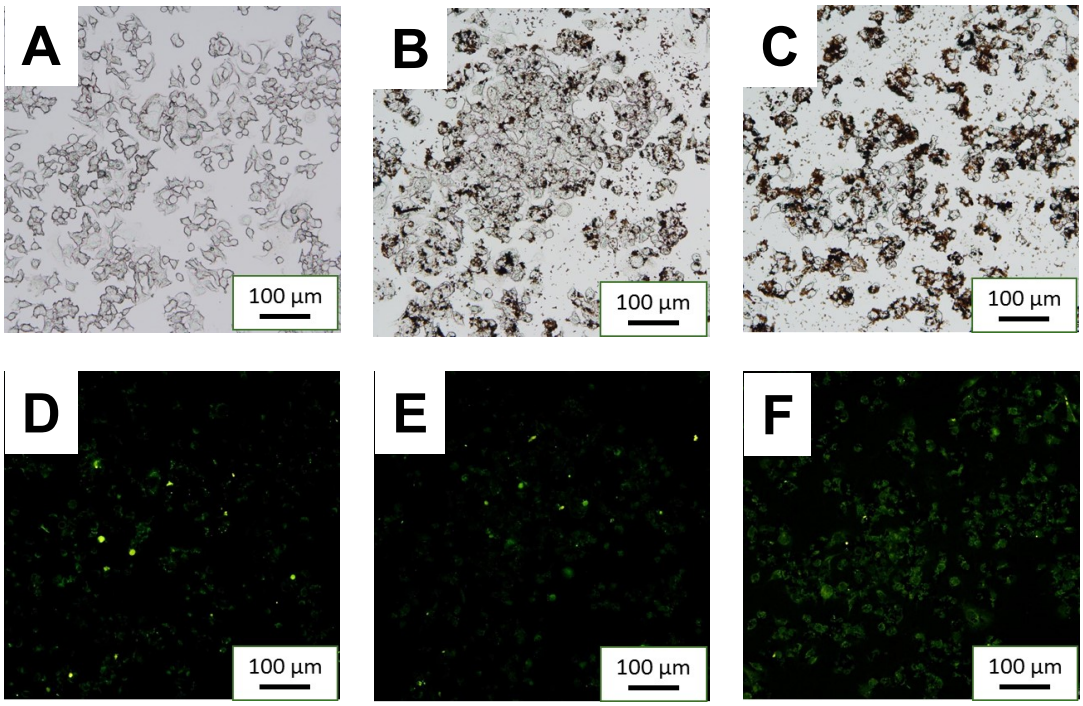

Fig. 3.2 Bright field (A-C) and fluorescence (D-F) microscopic images of MCF-7 cells pre-cultivated for 24 h in the presence of (A,D) 0, (B,E) 125, and (C,F) 250 µg of MNPs.

3.2.3 Cell death induced by intracellular or extracellular heating

Fig. 3.3 shows the ratios of the number of viable cells measured at 0 and 24 h after 20-min exposure to an alternating magnetic field to the initial number of viable cells. Here "AMF" represents the time immediately after the magnetic field application and "AMF+I24" indicates the time after 24-h incubation at 37°C subsequent to the magnetic field application. The initial number of viable cells, $N_{vc,initial}$, was measured just before the magnetic field application.

For the sample in the absence of MNPs (control), of which temperature remained at apprximately 37°C under the alternating magnetic field, only a slight decrease and 1.4-fold increase in the number of viable cells were observed at "AMF" and "AMF+I24", respectively, in both systems. It should be mentioned here that the difference between two systems in the absence of MNPs is simply the difference in the incubation period. The increments in viable cell counts at "AMF+I24" were slightly smaller than the results after 24-h incubation in the preceding section, which were contributable to a certain damage caused by the operation for magnetic field application.

In contrast, for the samples in the presence of MNPs, the decrease in the number of viable cells was observed at "AMF" and a further decrease was observed at "AMF+I24". With 125 μg of MNPs, with the temperature rise to 45°C under the alternating magnetic field, the reduction in the viable cell count to approximately 0.8 times of the initial count was observed at "AMF" in both systems. At "AMF+I24", the ratio of $N_{vc}/N_{vc,initial}$ decreased to 0.5 and 0.4 in "simply-added" and "pre-cultivated" systems, respectively. With 250 μg of MNPs, with the temperature rising to 52°C, a decrease in the number of viable cells to 0.6 and 0.1 times of the initial number was observed at "AMF" and "AMF+I24", respectively, in the "simply-added" system. More clearly in the "pre-cultivated" system, the ratio of $N_{vc}/N_{vc,initial}$ was reduced to 0.1 even at "AMF" and to as low as 0.05 at "AMF+I24".

The cell death induced by MNPs subjected to the alternating magnetic field was found to appear earlier in "pre-cultivated" system than in "simply-added" system. Considering the results described in the section 3.2.2, there is a possibility that the presence of intracellular MNPs or the cellular uptake of MNPs causes (slight) cell damage, and then MCF-7 cells internalizing MNPs become sensitive to heat (temperature rise).

Through this chapter and the section 2.5, significance of cellular uptake of MNPs to induce

cell death efficiently has been demonstrated.

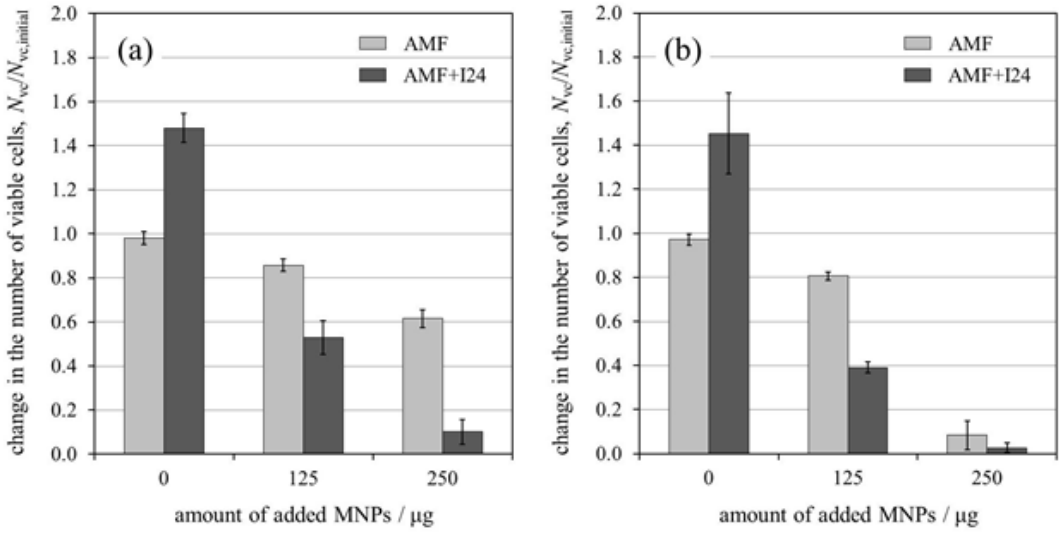

Fig. 3.3 Ratios of the number of viable cells measured at 0 and 24 h after 20-min exposure to an alternating magnetic field to the initial number of viable cells for (a) "simply-added" and (b) "pre-cultivated" systems. "AMF" represents the time immediately after the exposure to alternating magnetic field and "AMF+I24" indicates the time after 24-h incubation at 37°C subsequent to the magnetic field application.

3.3 Surface design of MNPs suitable for *in vivo* application

3.3.1 Experimental

This study is the collaboration research with Catholic University of Korea (Prof. Kun Na group) [23].

Synthesis of AHP@MNPs

MNPs with a diameter of 10 nm were synthesized by the same method described in the chapter 2. AHP was prepared according to a report [15]. Those MNPs an AHP were mixed and sonicated in water at a weight ratio of 1 to 1. The molecular weight of HA (obtained from Bioland Co., Cheonan, Korea) is 5.8 kDa. PheoA was purchased from Frontier Scientific (Logan, UT).

Cellular uptake and cell death study in vitro

Mouse embryonic fibroblast NIH3T3 and murine melanoma K1735 cells (American Type Culture Collection, USA) were used. AHP@MNPs at the concentration of 3-50 μg/mL were added to 1×10^5 NIH3T3 and K1735 cells. After washing with PBS, cellular uptake of AHP@MNPs was observed by a fluorescent microscope. Nuclei of cells were stained with DAPI (colored blue). AHP@MNPs was colored red derived from PheoA.

When AHP@MNPs at MNPs concentration of 12 μg/mL were added to 2×10^4 NIH3T3 and K1735 cells, the samples after washing with PBS were exposed to He-Ne laser with a wavelength of 671 nm and AC magnetic field with a frequency of 112 kHz with a strength of magnetic field of 250 Oe. Cell viability was evaluated by MTT assay.

In vivo *study of accumulation to tumor and therapeutic effect of AHP@MNPs*

For the melanoma tumor developed after the injection of K1735 cells into mice, AHP@MNPs at the amount of 0.01 mmol/kg of MNPs were intravenously injected into the mice. Then, the accumulation of AHP@MNPs to tumor was observed by a fluorescent microscope, and the tumors were exposed to He-Ne laser with a wavelength of 671 nm at 200 mW/cm^2 for 500 s and

AC magnetic field with a frequency of 112 kHz with a strength of magnetic field of 250 Oe for 30 min. Therapeutic effect was evaluated by measuring tumor size before/after the exposure. It should be noted here that all animal experiments were approved by the Institutional Animal Care and Use Committee (IACUC) of the Catholic University of Korea (Republic of Korea) in accordance with the "Principles of Laboratory Animal Care", NIH publication no. 85-23, revised in 1985, according to K. S. Kim et al. [23].

3.3.2 Results and discussion

The schematic diagram of this study was shown in Fig. 3.4.

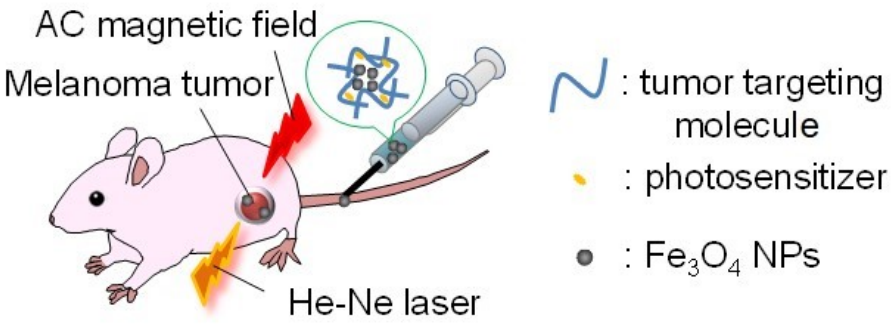

Fig. 3.4 Schematic diagram of this study. Hyaluronic acid is used as a tumor targeting molecule and pheophorbide-a is used as a photosensitizer.

First of all, it should be noted here that AHP was successfully modified on the surface of MNPs with attractive electrostatic interaction between positive charge of spermine and negative charge of hyaluronic acid with pheophorbide-a. The AHP@MNPs showed high dispersibility in water because of their high hydrophility derived from HA [23].

Using NIH3T3 and K1735 cells, cellular uptake of AHP@MNPs was evaluated. NIH3T3 cells are normal cells, whereas K1735 cells are cancer cells. Hence, CD44 is overexpressed on K1735 cells not on NIH3T3 cells. After the addition of AHP@MNPs to the medium containing cells, cellular uptake of AHP@MNPs was observed in CD44-positive K1735 cells, while CD44-negative NIH3T3 cells did not take up AHP@MNPs, according to the fluorescent images reported by K. S. Kim et al. [23]. Hence, AHP@MNPs was suggested to be incorporated into cells through CD44 receptor-mediated endocytosis, and the ability of cancer targeting of AHP@MNPs was expected.

As a result, when cells incubated with AHP@MNPs were exposed to He-Ne laser with a wavelength of 671 nm and AC magnetic field with a frequency of 112 kHz with a strength of

magnetic field of 250 Oe, viability was remained >90% for NIH3T3 cells, but the viability of K1735 cells was decreased to 24%, according to the results from MTT assay reported by K. S. Kim et al. [23].

Using melanoma-tumor bearing mice, tumor-accumulation efficacy of AHP@MNPs was evaluated by the fluorescent intensity of tumor derived from PheoA. After 6 h from the intravenous injection of AHP@MNPs, high fluorescent intensity was observed at tumor, which indicative of accumulation of AHP@MNPs to tumor. Furthermore, the red fruorescence (PheoA of AHP@MNPs) was observed just around the nucleus (colored blue) of tumor cells, which is suggestive of cellular uptake of AHP@MNPs. From these results (reported by K. S. Kim et al. [23]), high tumor accumulation and internalization efficacy of AHP@MNPs was demonstrated *in vivo*.

At the point, the tumors were exposed to He-Ne laser at 200 mW/cm^2 for 500 s and AC magnetic field for 30 min. As a result, one third or a half of smaller tumor volume was observed at 14 days after magnetic hyperthermia combined with photodynamic therapy than the tumor volume with no NPs (just injection of PBS) or with just hyperthermia treatment after 14 days from the exposure treatment, according to the *in vivo* results reported by K. S. Kim et al. [23], which suggestive of the potential of practical use of magnetic hyperthermia combined with photodynamic therapy using AHP@MNPs.

3.4 Conclusion

Surface design of MNPs with considered the enhancement of cellular uptake and therapeutic effect with another therapy as well as controlled magnetic property showed high potential of practical use of MNPs in magnetic hyperthermia.

In section 3.2, the cellular uptake of MNPs was indicated to induce a slight cell damage, which was reflected as an increase in generation of reactive oxygen species as well as an inhibition of cell proliferation, and to cause a high degree of cell death at the raised temperatures. A significant decrease in cell viability observed in the presence of intracellular MNPs under AC magnetic field may be originated from the combined or synergistic effect of intracellular heating and cellular damage by MNPs.

In section 3.3, design of surface and magnetic property of MNPs for *in vivo* application was investigated. To obtain the targeting ability to cancer cells, hyaluronic acid was modified onto MNPs. Hyaluronic acid has an advantage of specific binding to hyaluronic-acid receptor (CD44) overexpressed on cancer cells. To increase in therapeutic effect, pheophorbide-a was modified onto MNPs as a photosensitizer. Because pheophorbide-a generates reactive oxugen species when exposed to the light, increase in therapeutic effect by magnetic hyperthermia combined with photodynamic therapy is expected. Considered to the applied condition of AC magnetic field, superparamagnetic MNPs were employed. As a result, the designed MNPs was accumulated specific to tumor in mice, and then tumor growth was inhibited by magnetic hyperthermia combined with photodynamic therapy [23].

References

[1] R. T. Gordon et al., "Intracellular hyperthermia. A biophysical approach to cancer treatment via intracellular temperature and biophysical alterations", *Med. Hypotheses*, 5, 83 (1979).

[2] D.C.F. Chan et al., "Synthesis and evaluation of colloidal magnetic iron oxides for the site-specific radiofrequency-induced hyperthermia of cancer", *J. Magn. Magn. Mater.*, 122, 374 (1993).

[3] A. Jordan et al., "Cellular uptake of magnetic fluid particles and their effects on human adenocarcinoma cells exposed to AC magnetic fields *in vitro*", *Int. J. Hyperthermia*, 12, 705 (1996).

[4] A. Jordan et al., "Endocytosis of dextran and silan-coated magnetite nanoparticles and the effect of intracellular hyperthermia on human mammary carcinoma cells in vitro", *J. Magn. Magn. Mater.*, 194, 185 (1999).

[5] H.L. Rodriguez-Luccioni et al., "Enhanced reduction in cell viability by hyperthermia induced by magnetic nanoparticles", *Int. J. Nanomedicine*, 6, 373 (2011).

[6] E.-K. Park et al, "Folate-conjugated methoxy poly(ethylene glycol)/poly(ε-caprolactone) amphiphilic block copolymeric micelles for tumor-targeted drug delivery", *J. Controlled Release*, 109, 158 (2005).

[7] C. P. Leamon and J. A. Reddy, "Folate-targeted chemotherapy", *Adv. Drug Delivery Rev.*, 56, 1127 (2004).

[8] R. Rastogi et al., "Evaluation of folate conjugated pegylated thermosensitive magnetic nanocomposites for tumor imaging and therapy", *Colloids Surf. B Biointerfaces*, 82, 160 (2011).

[9] A. Lo et al., "Hepatocellular carcinoma cell-specific peptide ligand for targeted drug delivery", *Mol.Cancer Ther.*, 7, 579 (2008).

[10] N. Zhang et al., "PLGA nanoparticle-peptide conjugate effectively targets intercellular cell-adhesion molecule-1", *Bioconjugate Chem.*, 19, 145 (2007).

[11] T. Chen et al., "Smart Multifunctional Nanostructure for Targeted Cancer Chemotherapy and Magnetic Resonance Imaging", *ACS Nano*, 5, 7866 (2011).

[12] Z. Cao et al., "Reversible cell-specific drug delivery with aptamer-functionalized liposomes", *Angew. Chem., Int. Ed.*, 48, 6494 (2009).

[13] Y.-A. Shieh et al., "Aptamer-based tumor-targeted drug delivery for photodynamic therapy",

ACS Nano, 4, 1433 (2010).

[14] W. Richter, "Non-immunogenicity of purified hyaluronic acid preparations tested by passive cutaneous anaphylaxis", *Int. Arch. Allergy Immunol.*, 47, 211, (1974).

[15] F. Li et al., "Acetylated Hyaluronic Acid/Photosensitizer Conjugate for the Preparation of Nanogels with Controllable Phototoxicity: Synthesis, Characterization, Autophotoquenching Properties, and in vitro Phototoxicity against HeLa Cells", *Bioconjugate Chem.*, 21, 1312 (2010).

[16] C-S Lee and K. Na, "Photochemically triggered cytosolic drug delivery using pH-responsive hyaluronic acid nanoparticles for light-induced cancer therapy", *Biomacromolecules*, 15, 4228 (2014).

[17] W. Park et al., "Cancer cell specific targeting of nanogels from acetylated hyaluronic acid with low molecular weight", *Eur. J. Pharm. Sci.*, 40, 367 (2010).

[18] H. Iida et al., "Synthesis of Fe_3O_4 nanoparticles with various sizes and magnetic properties by controlled hydrolysis", *J. Colloid Interface Sci.*, 314, 274 (2007).

[19] M. Mahmoud et al., "Cytotoxicity of uncoated and polyvinyl alcohol coated superparamagnetic iron oxide nanoparticles", *J. Phys. Chem. C*, 113, 9573 (2009).

[20] M. Könczöl et al., "Cell-cycle changes and oxidative stress response to magnetite in A549 human lung cells", *Chem. Res. Toxicol.*, 26, 693 (2013).

[21] S. Naqvi et al., "Concentration-dependent toxicity of iron oxide nanoparticles mediated by increased oxidative stress", *Int. J. Nanomedicine*, 5, 983 (2010).

[22] M. I. Khan et al., "Induction of ROS, mitochondrial damage and autophagy in lung epithelial cancer cells by iron oxide nanoparticles", *Biomaterials*, 33, 1477 (2012).

[23] K. S. Kim et al., "Stimuli-responsive magnetic nanoparticles for tumor-targeted bimodal imaging and photodynamic/hyperthermia combination therapy", *Nanoscale*, 8, 11625 (2016).

Chapter 4

Synthesis of MFe$_2$O$_4$ nanoparticles and their effect on breast cancer cell death under alternating magnetic field

4.1 Introduction

For the development of effective magnetic hyperthermia, design of magnetic nanoparticles as a heat generator is focused in this chapter, as a study leading to the future technology. To increase the therapeutic effect of magnetic hyperthermia, this chapter describes the increase in heating capacity of nanoparticles with controlled magnetic properties considering the occupation of the A- and B-sites by transition metal cations (M^{2+} and Fe^{3+}) in spinel structure. Many recent researches reported that the substitution of Fe^{2+} with other metal ions (MFe$_2$O$_4$; M = Ni, Co, Mn) improves the magnetic property and heating efficacy [1-3]. Therefore in this chapter, synthesis of cobalt and magnesium ferrite ($CoFe_2O_4$ and $MgFe_2O_4$) nanoparticles and their effect on death in human breast cancer MCF-7 cells under alternating magnetic field were investigated. Breast cancer was used as a cancer cells because magnetic hyperthermia can, in principle, be easily applied to tumors located on/under the human skin.

First, $CoFe_2O_4$ was selected owing to its potential of having greater magnetic anisotropy than iron-oxide nanoparticles [2,4]. High coercivity is expected from their large magneto-crystalline anisotropy (K), which should produce sufficient heat to induce cancer cell death under alternating magnetic field. When single-domain state and ferromagnetic property, coercivity (H_c) is estimated by the Stoner-Wohlfarth model based theory [5,6]:

$$H_C = 0.98 \times K/M_S \quad (1)$$

According to ref [2], the magnetic anisotropy of bulk $CoFe_2O_4$ is one-order larger than that of Fe_3O_4, whereas the saturation magnetization (M_s) of $CoFe_2O_4$ is almost 90% of Fe_3O_4. From the equation (1) and the information mentioned above, H_c of $CoFe_2O_4$ is estimated to be 10 times

larger than Fe_3O_4. Considering the M_s value also, approximately 9 times of enhancement in hysteresis area for $CoFe_2O_4$, as compared to Fe_3O_4. Because it can be suggested that heating capacity including the temperature rise and the specific absorption rate (SAR) is approximately proportional to the hysteresis area [7], 9-times enhancement of heating capacity is expected for $CoFe_2O_4$ nanoparticles, as compared to Fe_3O_4 nanoparticles with a same diameter. $CoFe_2O_4$ nanoparticles were reported to have a potential of larger hysteresis area among other spinel ferrite nanoparticles [5]. Additionally, the amount of energy converted into heat per unit time and mass has been reported to be greater for $CoFe_2O_4$ nanoparticles than for other spinel ferrites of the same size, such as iron oxide [2]. The $CoFe_2O_4$ nanoparticles also maintain excellent chemical stability [8]. Therefore, in this study, the synthesis of $CoFe_2O_4$ nanoparticles by applying the synthetic method developed for Fe_3O_4 nanoparticles on the basis of hydrolysis in an aqueous solution containing iron(II) and iron(III) salts, in which organic amine plays significant role as a base and also as a protective reagent, was investigated, and their effect on cell death was examined.

However, even if $CoFe_2O_4$ nanoparticles have higher heating capacity and excellent chemical stability, administration of $CoFe_2O_4$ nanoparticles to human body has also a risk because Co^{2+} ions eluted from $CoFe_2O_4$ nanoparticles are toxic.

Hence in the next section, as a candidate of nanoparticles with high safety and high heating efficacy, $MgFe_2O_4$ was selected. $MgFe_2O_4$ nanoparticles are composed of non-toxic elements, suggesting that they have greater biocompatibility as compared to other ferrite nanoparticles. Furthermore, $MgFe_2O_4$ nanoparticles have been receiving attention as a new heat source because of their frequency-dependence of heating efficiency. Around 300 kHz, which corresponds to the frequency generally used for magnetic hyperthermia, the temperature rise of $MgFe_2O_4$ powder was reported to be highest among other kinds of ferrite powder [9]. When estimated the heating capacity using the difference of ΔT reported in Ref. 9, 8-times enhancement of heating capacity is expected for $MgFe_2O_4$, as compared to Fe_3O_4. Also, the SAR of $MgFe_2O_4$ nanoparticles was reported to be 297 W/g under safe strength and frequency of magnetic field [10], while the value was 20-40 W/g for superparamagnetic Fe_3O_4 nanoparticles under the same magnetic-field condition [11]. Hence, there are many reports regarding the synthesis of $MgFe_2O_4$ nanoparticles as shown in Table 4.1. However, a limited number of studies of the influence of $MgFe_2O_4$

nanoparticles on cells have been reported; especially the cell mortality associated with cellular uptake of $MgFe_2O_4$ nanoparticles is yet to be clearly discussed. In this study, synthesis of $MgFe_2O_4$ nanoparticles and the effect of their cellular uptake on the death under alternating magnetic field in MCF-7 cells were investigated.

Table 4.1 Magnetic behavior and particle size of $MgFe_2O_4$ synthesized in various methods

Synthetic method	Magnetization ($emu \cdot g^{-1}$)	Particle size (nm)	Coercivity (Oe)	Reference
combustion	33.83	10 - 30	53	[12]
co-precipitation	4 (at 1 kOe)	-	-	[13]
microemulsion	1 (at 100 Oe)	20	-	[14]
sol-gel	15.3	6	-	[15]
co-precipitation	5.8	6	-	[15]
combustion	31.56	40	182	[16]
hydrothermal	-	3	-	[17]
ultrasound assisted ball-milling	54.8	20	-	[18]

4.2 $CoFe_2O_4$ nanoparticles

4.2.1 Experimental

Synthesis and characterization of nanoparticles

A 50-mL aqueous solution containing 0.017 mol·L^{-1} cobalt(II) chloride ($CoCl_2·4H_2O$) and 0.033 mol·L^{-1} iron(III) chloride ($FeCl_3·6H_2O$) was prepared, and a 50-mL aqueous solution containing 0.123 mol·L^{-1} spermine, or *N*,*N*'-bis(3-aminopropyl)butane-1,4-diamine (pH 12.1) was also prepared as a base. After the aqueous solution containing spermine was heated at 90°C, the cobalt(II) and iron(III) chloride aqueous solution was added slowly to the aqueous spermine solution, which was followed by stirring for 12 h at 90°C. Finally, a black powder was obtained after washing the precipitate with water and ethanol several times and drying in a desiccator at room temperature. Fe_3O_4 nanoparticles with a diameter of 10 nm were also synthesized with the same procedure described in chapter 2, using iron(II) chloride ($FeCl_2·4H_2O$) and iron(III) chloride at a molar ratio of 2:1, and spermine as a base.

The shape and size of $CoFe_2O_4$ nanoparticles were observed by field-emission transmission electron microscopy (FE-TEM) with a Hitachi HF-2200 microscope (Tokyo, Japan) at 200 kV and their composition and elemental mapping were analyzed by energy dispersive X-ray (EDX) analysis in FE-TEM. The shape and size of Fe_3O_4 nanoparticles were observed by TEM with a JEOL JEM-1011 microscope (Tokyo, Japan) at 100 kV. The mean diameters of those products were calculated using a following equation after counting and measuring diameters (D_n) of one hundred nanoparticles in the TEM images.

$$\text{Mean diameter} = \frac{(D_1+D_2+D_3+\cdots+D_{100})}{100} \quad (2)$$

The crystal structure of the products was characterized by X-ray diffraction (XRD) patterns recorded using a SmartLab diffractometer (Rigaku, Tokyo, Japan) with Co Kα radiation (1.7890 Å). The magnetic field dependence of the magnetization curves of samples was measured by an MPMS 3 or MPMS 7 superconducting quantum interference device (SQUID; Quantum Design, Ltd., San Diego, CA) at 300 K, in which the applied range was from −10 kOe to 10 kOe. The zeta

potential and hydrodynamic diameter of the specimens dispersed in water at around pH 7 were evaluated with an Otsuka Electronics ELS-8000 electrophoretic light-scattering spectrophotometer (Osaka, Japan).

MCF-7 cell cultivation

Human breast cancer MCF-7 cells were cultured in Eagle's minimum essential medium (EMEM, Sigma-Aldrich, St. Louis, MO) with 10% fetal bovine serum (FBS, ThermoFisher Scientific, Waltham, MA), 5% L-glutamine (Invitrogen, Life Technologies, Grand Island, NY), 1% MEM non-essential amino acid (Gibco, Life Technologies), and 1% antibiotic-antimycotic (Gibco) under culture conditions of 37°C and 5% CO_2.

Cytotoxicity and cellular uptake study

MCF-7 cells were seeded in a 6-well dish at a density of 5×10^5 cells per 3 mL of medium in each well. $CoFe_2O_4$ or Fe_3O_4 nanoparticles in amounts of 0, 200, 400, 600, or 800 μg were added to each well and then incubated at 37°C at 5% CO_2 for 24 h. After removing excess nanoparticles by three washes with Dulbecco's phosphate buffered saline (DPBS; Gibco) followed by centrifugation at 1200 rpm for 5 min, the cells were dispersed in 1 mL of DPBS with 6% FBS. We used a BD Cell Viability Kit (BD Biosciences, Becton, Dickinson and Co., Franklin Lakes, NJ) to discriminate live cells, dead cells, and nanoparticles: 2 μL of 42 μM thiazole orange (TO) in dimethyl sulfoxide and 1 μL of 4.3 mM propidium iodide (PI) in water were added to 1 mL of cells suspended in DPBS, and then analyzed with a BD FACSCanto II flow cytometer. Live cells are PI negative and TO positive, dead cells are both PI and TO positive, and nanoparticles are both PI and TO negative.

Cellular viability as well as cellular uptake of nanoparticles can be analyzed via flow cytometry because increased side scatter (SSC), which is indicative of intracellular complexity, can be measured when the laser light crosses the cell in the flow cytometer, as described in the chapter 2. Hence, the SSC intensity of a cell that has incorporated nanoparticles is greater than that of a cell that has not incorporated nanoparticles. In the present study, the cellular uptake of $CoFe_2O_4$ and Fe_3O_4 nanoparticles was measured based on SSC intensity.

The amount of nanoparticles contained per cell was also evaluated for both $CoFe_2O_4$ and Fe_3O_4 nanoparticles as described in the chapter 2. Intracellular Fe was formed into a thiocyanate-iron(III) complex by using HCl, trichloroacetic acid solution, H_2O_2, and potassium thiocyanate solution, followed by measurement of absorbance at 480 nm using a JASCO V-550 spectrophotometer (JASCO International Co. Ltd., Tokyo, Japan).

To observe cellular uptake of nanoparticles with an optical microscope, prussian blue staining was performed using an Iron Stain Kit (Sigma-Aldrich), by which iron-containing nanoparticles turned blue and cells were stained red. Iron stain solution including potassium ferrocyanide solution and hydrochloric acid solution at a ratio of 1:1 was added to DPBS-washed cells at a particle dose of 200 μg in a 6-well dish. After 10 min, the residues were rinsed away with DPBS. Then, pararosaniline solution was added for staining cells, and after 5 min, the residues were rinsed away with DPBS. The cells were then observed under a Nikon TE2000-U microscope (Tokyo, Japan).

Evaluation of the dissolution of Co^{2+} from $CoFe_2O_4$ nanoparticles in water

$CoFe_2O_4$ nanoparticles (1 mg) were dispersed in 3 mL of water in a polypropylene tube (around pH 7). After a 24-h or 72-h incubation at 37°C and 5% CO_2, the supernatants of both samples were collected by centrifugation, and the concentration of Co^{2+} in the sample was measured by a Thermo Scientific iCAP Qc inductively coupled plasma-mass spectrometer (ICP-MS). Before measurements, a calibration curve of Co^{2+} concentration was made using a cobalt standard solution (Co in 0.1 mol/L HNO_3; Kanto Chemical Co. Ltd., Tokyo, Japan). The concentration of Co^{2+} in the samples was calculated using the calibration curve.

Evaluation of cell death with nanoparticles under alternating magnetic field

To test cell viability, 5×10^5 MCF-7 cells were cultured per well in the presence of $CoFe_2O_4$ or Fe_3O_4 nanoparticles (0, 200, 400, 600, or 800 μg per well). After washing the cells three times with DPBS, the cells containing nanoparticles were collected by magnetic separation and suspended in 500 μL of medium. An AC magnetic field was applied for 20 min using both a 3-turn coil with an outer diameter of 40 mm and an EASYHEAT induction-heating device (Alonics,

Ltd., Tokyo, Japan) operated at an output power of 4.3 kW, an electric current of 569.1 A, and a frequency of 325 kHz, from which the strength of the magnetic field was calculated to be 536 Oe. The change in temperature under the AC magnetic field was monitored with an Anritsu FL-2000 fiber thermometer (Tokyo, Japan). Temperature curves were also obtained for 500 μL of water containing 1 mg of nanoparticles without cells. Cell death mediated by nanoparticles subjected to the AC magnetic field was analyzed by flow cytometry using PI and TO staining.

4.2.2 Characterization of nanoparticles

First of all, establishment of synthetic method for single-domain $CoFe_2O_4$ nanoparticles with high crystalline was discussed. When synthesized by directly applied the synthetic method developed for Fe_3O_4 nanoparticles as described in chapter 1.2.4 and 2.2 except for using Co^{2+} instead of Fe^{2+}, the products did not have magnetism. This could be because Co^{2+} is difficult to occupy B-site than Fe^{2+} in the inverse spinel structure. Then, to active the Co^{2+} behavior, the prepared solution was heated to 90°C. As a result, single-domain $CoFe_2O_4$ nanoparticles with high crystalline and high magnetism were obtained. From this experience, heating was suggested to be useful approach to form MFe_2O_4 with high crystalline.

Fig. 4.1A and 4.1B depict the TEM images of $CoFe_2O_4$ and Fe_3O_4 nanoparticles, respectively, and revealed that both particles were spherical or truncated cubic in shape, with a mean diameter of 9.4 ± 2.4 for $CoFe_2O_4$ and 11.1 ± 2.5 nm for Fe_3O_4. The mean diameter of $CoFe_2O_4$ nanoparticles was calculated from randomly collected 100 particles in its TEM image. Size distribution of $CoFe_2O_4$ nanoparticles is shown in Fig. 4.2. For $CoFe_2O_4$ nanoparticles, the ratio of Co to Fe in an individual particle was analyzed by EDX. It is known that ICP shows a higher precision and lower detection limit than EDX. However, EDX can provide the composition with certain accuracy although that depends on the element to be analyzed. Indeed EDX has been frequently used to determine the chemical composition of materials, for example electrodeposited thin films containing Co and Fe such as alloy films and nanoparticles consisting of Co and Fe. Hence EDX have been chosen in order to discuss not the mean composition of products but the difference in localized areas or in particle-by-particle. The ratio of oxygen could not be precisely determined due to the limitations of the measurement method. The EDX results suggest that the atomic ratio of Co to Fe is 1 to 2, and particles composed of only cobalt or iron were not observed. To discuss the composition of products, the elemental mapping of $CoFe_2O_4$ nanoparticles was also examined as shown in Fig. 4.3. Fe and Co were found to exist uniformly along nanoparticles with the Co:Fe atomic ratio of 1:2. Fig. 4.3C shows XRD patterns for the products synthesized with cobalt(II) chloride and iron(III) chloride (a) and with iron(II) chloride and iron(III) chloride (b). The pattern (a) was matched with the standard pattern of $CoFe_2O_4$ (JCPDS# 22-1086) and the pattern (b) was matched with the standard pattern of Fe_3O_4 (JCPDS# 19-0629). Although both

patterns resembled each other, the positions of diffractions peaks were slightly but certainly different between the patterns (a) and (b). For example, the *d* values of the lattice spacing of (311) was calculated to be 2.526 Å for pattern (a) and 2.529 Å for pattern (b) by using the Bragg equation for the peak observed at $2\theta \sim 41°$, and the slight difference in these values was attributable to the difference between theoretical values of 2.531 Å for $CoFe_2O_4$ (JCPDS# 22-1086) and 2.532 Å for Fe_3O_4 (JCPDS# 19-0629). The crystallite size calculated from XRD by applying Scherrer's formula to the (311) diffraction peak was 8 nm (in diameter) for the both patterns (a) and (b), which is consistent with the TEM results. Thus, products (a) and (b) were identified to be $CoFe_2O_4$ and Fe_3O_4, respectively, with a spinel structure.

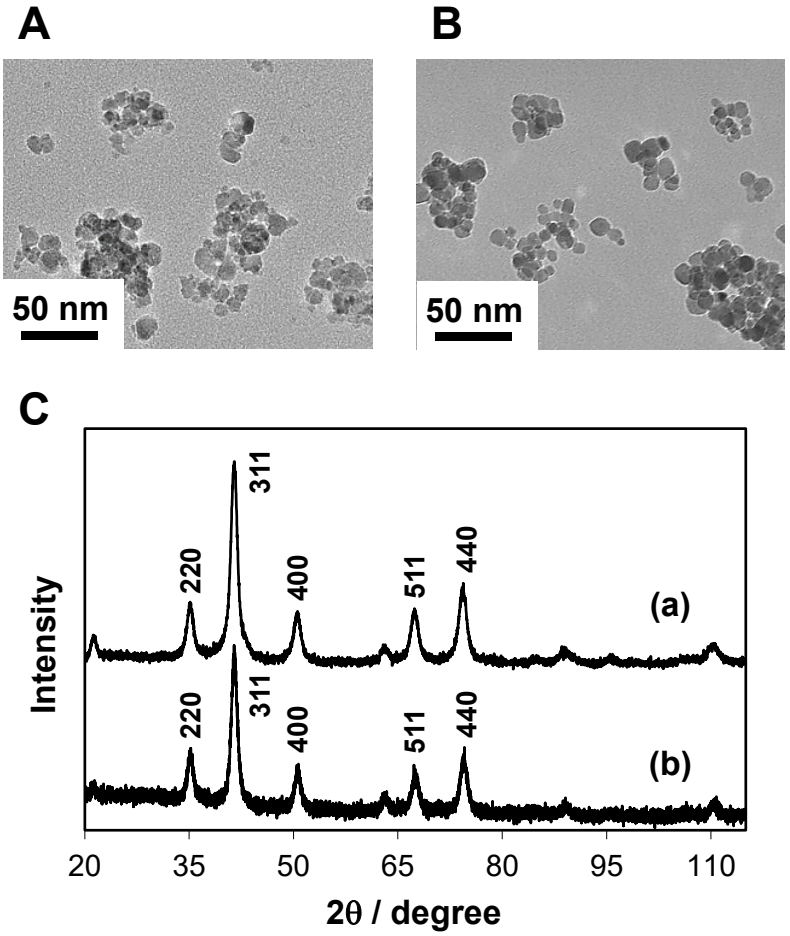

Fig. 4.1 Characterization of $CoFe_2O_4$ and Fe_3O_4 nanoparticles employed in this study. TEM images of $CoFe_2O_4$ nanoparticles (A) and Fe_3O_4 nanoparticles (B), and XRD patterns with Co Kα radiation (C): $CoFe_2O_4$ (a) and Fe_3O_4 (b). Reprinted with permission. Copyright @ 2015 Elsevier B. V.

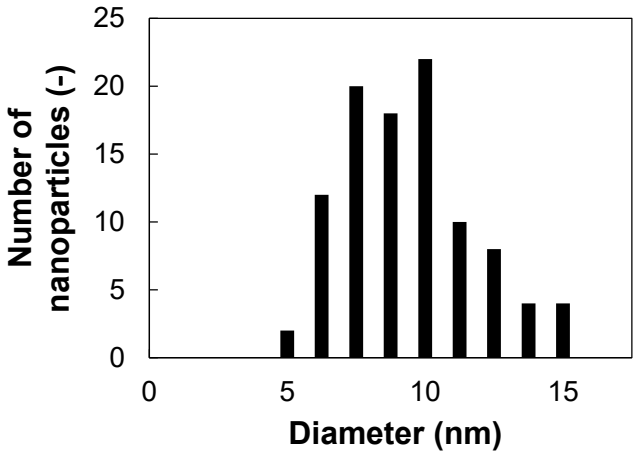

Fig. 4.2 Size distribution of synthesized $CoFe_2O_4$ nanoparticles.

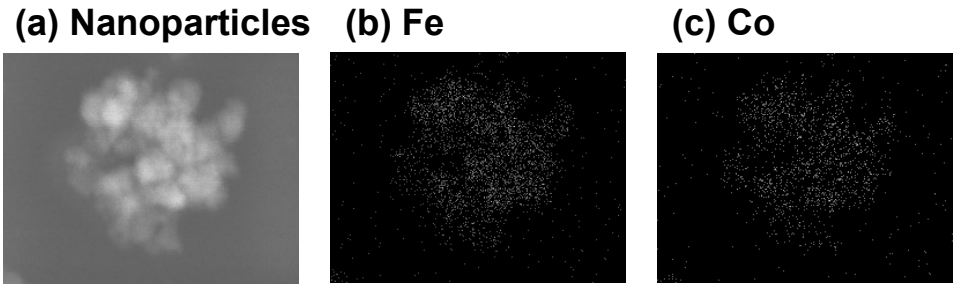

Fig. 4.3 Elemental mapping of the synthesized nanoparticles: the image of nanoparticles (a), Fe mapping (b), and Co mapping (c). Reprinted with permission. Copyright @ 2015 Elsevier B. V.

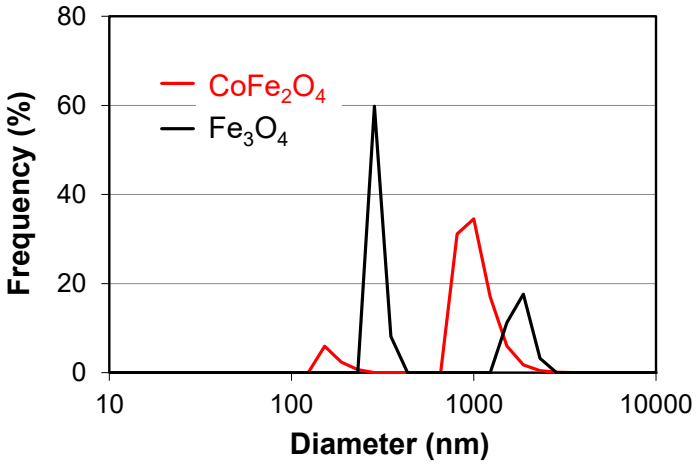

Fig. 4.4 Size distribution of $CoFe_2O_4$ and Fe_3O_4 nanoparticles in water characterized by dynamic light scattering.

The results of TEM, EDX analysis, elemental mapping, and XRD measurements suggest that $CoFe_2O_4$ nanoparticles with a diameter of 10 nm were synthesized without composites of Co_3O_4, Fe_3O_4, and γ-Fe_2O_3. The formation of $CoFe_2O_4$ likely progressed by a generally known co-precipitation reaction represented by the following equation [19]:

$$Co^{2+} + 2Fe^{3+} + 8OH^- \rightarrow CoFe_2O_4 + 4H_2O. \quad (3)$$

The size distribution in water was characterized by dynamic light scattering for the nanoparticles synthesized in this study. As shown in Fig. 4.4, both nanoparticles were stable in water with forming secondary particles with hydrodynamic diameters of approximately 200 nm or 1 μm, similar to the study for Fe_3O_4 nanoparticles described in chapter 2.

Fig. 4.5 shows the magnetization curves of $CoFe_2O_4$ and Fe_3O_4 nanoparticles at 300 K. As depicted in Fig. 4.5, the magnetization value at the 10000 Oe field of both $CoFe_2O_4$ and Fe_3O_4 nanoparticles was found to be 60 $emu \cdot g^{-1}$. The magnetization values observed for the synthesized nanoparticles with a diameter of 10 nm were slightly smaller than those of bulk materials, which could be due to the effect of increased thermal fluctuation near the surface of nanoparticles or that of the magnetically disordered surface formed because of the large surface-to-volume ratio [20]. As also shown in Fig. 4.5, the coercivity of $CoFe_2O_4$ was 200 Oe and that of Fe_3O_4 was less than 10 Oe, suggesting that $CoFe_2O_4$ nanoparticles show a ferromagnetic type of behavior, whereas Fe_3O_4 demonstrate superparamagnetic behavior. Hence, the heat derived from $CoFe_2O_4$ is generated by hysteresis loss, and the heat generated by Fe_3O_4 is largely controlled by Néel and Brown relaxation under the AC magnetic field [2,21-23]. Thus, the substitution of Fe^{2+} with Co^{2+} is likely to result in an increase in coercivity.

Fig. 4.6 shows the temperature curve measured for 500 μL of water containing 1 mg of nanoparticles without cells under an AC magnetic field (569.1 A, 325 kHz) for 20 min using a 3-turn coil with an outer diameter of 40 mm (the strength of magnetic field was theoretically calculated to be 536 Oe). The temperature of $CoFe_2O_4$ nanoparticles was higher than that of Fe_3O_4, whose average temperature measured between 400 and 1200 s was 56°C for $CoFe_2O_4$ and 45°C for Fe_3O_4. From the initial slope of these time-dependent temperature curves in the first 100 s, specific absorption rates (SARs) of 404 and 319 $W \cdot g^{-1}$ was obtained for $CoFe_2O_4$ and Fe_3O_4 nanoparticles, respectively, under this condition by the following equation:

$$\mathrm{SAR} = \frac{\Sigma_i C_{pi} m_i}{m_{NPs}} \cdot \frac{\Delta T}{\Delta t} \quad (4)$$

where C_{pi} and m_i are specific heat capacity and mass for each substance, and m_{NPs} is the mass of nanoparticles.

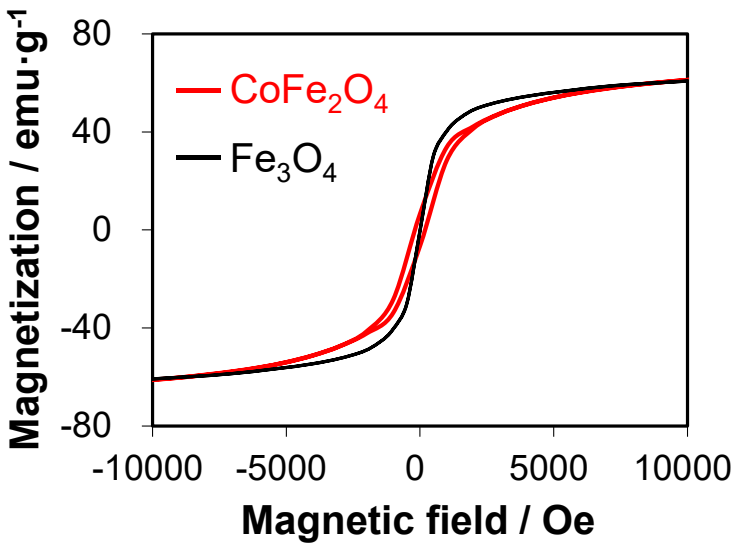

Fig. 4.5 Magnetization curves of $CoFe_2O_4$ and Fe_3O_4 nanoparticles. The curves were measured by SQUID at 300 K between −10000 and 10000 Oe of magnetic field strength. Reprinted with permission. Copyright @ 2015 Elsevier B. V.

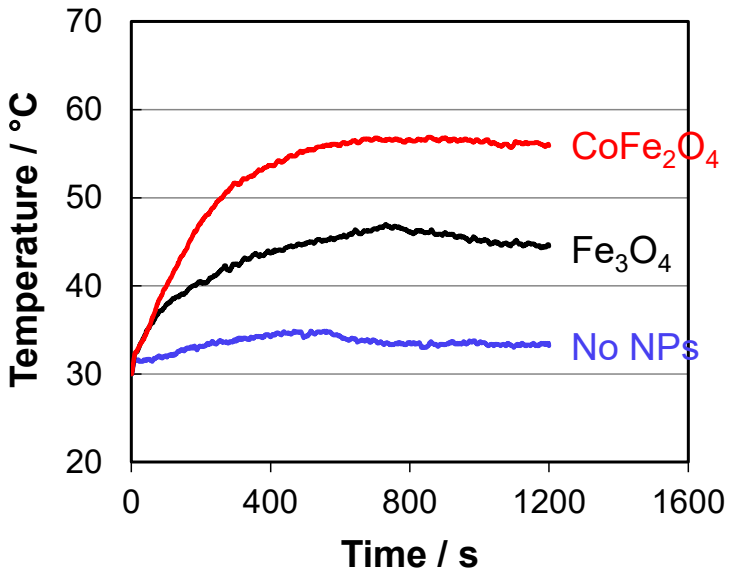

Fig. 4.6 Time dependence of the temperature curve of 1 mg of $CoFe_2O_4$ or Fe_3O_4 nanoparticles in 500 μL of water under an AC magnetic field. Reprinted with permission. Copyright @ 2015 Elsevier B. V.

4.2.3 Evaluation of cellular uptake and cell death

Next, the influence of nanoparticles on human breast cancer MCF-7 cells was investigated. Fig. 4.7 shows the percentage of cells containing nanoparticles (A) and the percentage of non-viable cells (B). As depicted in Fig. 4.7A, the percentage of cells containing nanoparticles tended to increase at the higher doses of both types of particles: at 200 μg, the percentage of cells containing nanoparticles was 50−60% and at 800 μg, the percentage of cells containing nanoparticles was 80%. No more than 10% cell mortality was observed following 24-h incubation with nanoparticles at concentrations from 0 to 800 μg. Neither Fe_3O_4 nor $CoFe_2O_4$ nanoparticles killed MCF-7 cells despite cellular uptake. Although the percentage of MCF-7 cell death observed with $CoFe_2O_4$ nanoparticles seems slightly higher than that for Fe_3O_4 at all doses, it should be noted that this tendency was observed even in the control experiment (without nanoparticles); the cell mortality was constant at the dose range from 0 to 800 μg for both Fe_3O_4 and $CoFe_2O_4$ nanoparticles.

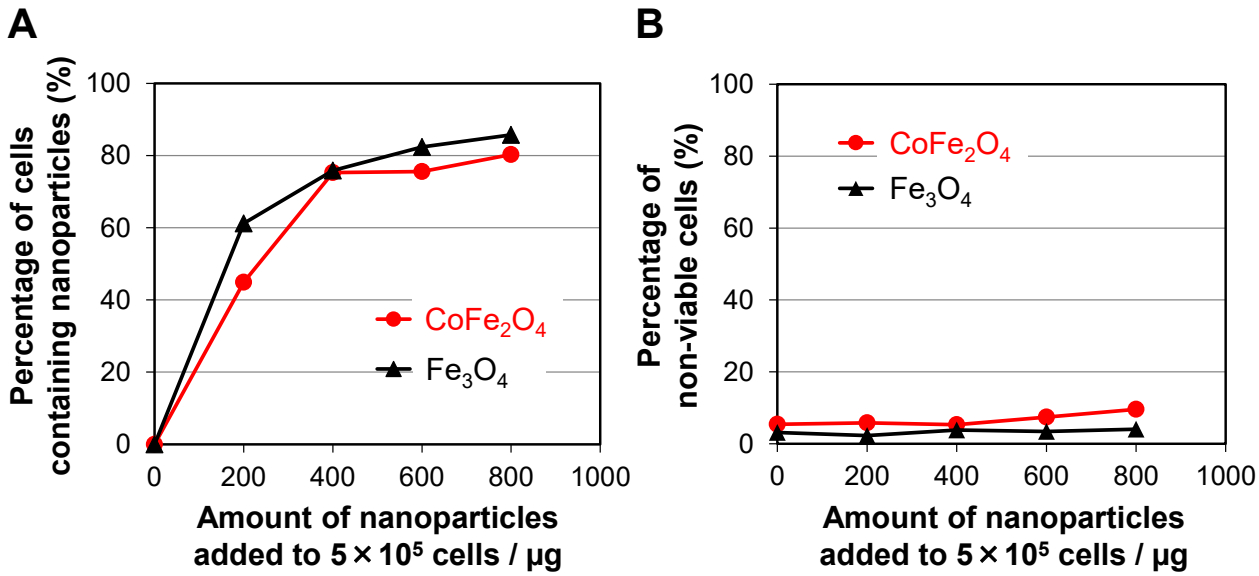

Fig. 4.7 Dependence of the percentage of cells containing nanoparticles (A) and the percentage of non-viable cells (B) on the amount of $CoFe_2O_4$ (circles) or Fe_3O_4 (triangles) nanoparticles added to 5×10^5 MCF-7 cells. Reprinted with permission. Copyright @ 2015 Elsevier B. V.

However, $CoFe_2O_4$ nanoparticles might derive cytotoxicity from Co^{2+} [24,25] eluted from $CoFe_2O_4$. For example, Catelas et al. [24] reported that Co^{2+} induces apoptosis via a caspase-3 pathway. To consider the influence of dissolved Co^{2+}, we examined Co^{2+} elution by ICP-MS under almost identical conditions as those used for the cytotoxicity test: the concentration was 1 mg of $CoFe_2O_4$ nanoparticles per 3 mL of H_2O at 37°C. As shown in Table 4.2, few Co^{2+} were eluted into the water from $CoFe_2O_4$ nanoparticles: the concentration of Co^{2+} in the sample was 0.785 $\mu g \cdot mL^{-1}$ (0.9% of Co was eluted) after a 24-h incubation, and 0.465 $\mu g \cdot mL^{-1}$ (0.6% of Co was eluted) after a 72-h incubation. The decrease of Co^{2+} concentration from 24 h to 72 h seems to be related to the adsorption of Co^{2+} to the surface of the polypropylene tube. Indeed, Kwon et al. [25] investigated the cytotoxicity of Co ions released from Co nanoparticles on RAW263.7 macrophage cells *in vitro*, and reported that Co ions at a concentration of 0.630 $\mu g \cdot mL^{-1}$ show no cytotoxic effect, but 4.777 $\mu g \cdot mL^{-1}$ of Co ions was cytotoxic. Based on this information, we conclude that an extensive elution of Co^{2+} from $CoFe_2O_4$ nanoparticles was not observed in this case, but further surface modification of $CoFe_2O_4$ should be the key when their practical application to magnetic hyperthermia is considered.

Table 4.2 Co^{2+} elution at the concentration of 1 mg of $CoFe_2O_4$ nanoparticles per 3 mL of H_2O. Reprinted with permission. Copyright @ 2015 Elsevier B. V.

	Concentration / $\mu g \cdot mL^{-1}$	Elution percentage (%)
Water	0.00004	0.0
24 h	0.785	0.9
72 h	0.465	0.6

Fig. 4.8 shows the dose dependence of the uptake of $CoFe_2O_4$ and Fe_3O_4 nanoparticles by MCF-7 cells. The $CoFe_2O_4$ nanoparticles were incorporated at a lower concentration than Fe_3O_4 nanoparticles. Approximately 75 pg of both types of nanoparticles was incorporated into each cell at a dose of 200 μg per 5×10^5 cells, and 200 pg (for $CoFe_2O_4$) or 230 pg (for Fe_3O_4) of nanoparticles was incorporated per cell at the dose of 800 μg. Based on the previous finding [26], this slight difference in uptake could be induced less by the composition of the nanoparticles than by their zeta potential. The zeta potential in water at around pH 7 was +2.6 mV for $CoFe_2O_4$

nanoparticles and +9.3 mV for Fe_3O_4 nanoparticles. The positive value of the zeta potential at pH 7 is attributable to the cationic form of amine groups in spermine adsorbed on the surface of nanoparticles [26].

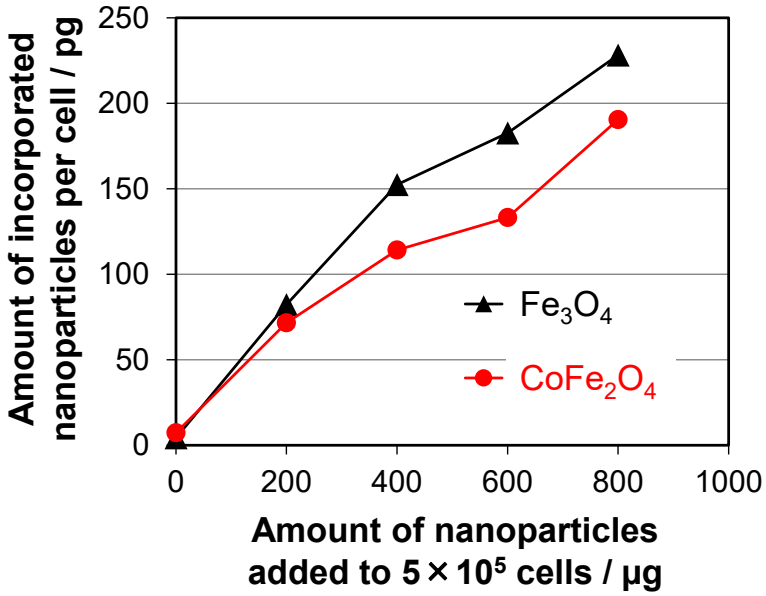

Fig. 4.8 Dependence of the amount of incorporated nanoparticles per cell on the amount of $CoFe_2O_4$ (circles) or Fe_3O_4 (triangles) nanoparticles added to 5×10^5 MCF-7 cells. Reprinted with permission. Copyright @ 2015 Elsevier B. V.

The uptake of nanoparticles into MCF-7 cells was observed with an optical microscope at the dose of 200 μg. In Fig. 4.9, MCF-7 cells were stained red and nanoparticles were stained blue by iron stain. Compared with the image of MCF-7 cells without the dose of nanoparticles (Fig. 4.9A), the incorporation of nanoparticles did not alter the apparent morphology of cells for both $CoFe_2O_4$ (Fig. 4.9B) and Fe_3O_4 (Fig. 4.9C). The nanoparticles were observed within the cytoplasm but not in the nucleus. The ratio of cells containing nanoparticles observed in those optical microscopic images was comparable to that evaluated by flow cytometry (Fig. 4.7). In addition, the amount of incorporated nanoparticles appeared to be similar for both $CoFe_2O_4$ and Fe_3O_4 nanoparticles, which is consistent with the result shown in Fig. 4.8. Therefore, cellular uptake of nanoparticles was evidenced by the results shown in Figs. 4.7, 4.8, and 4.9.

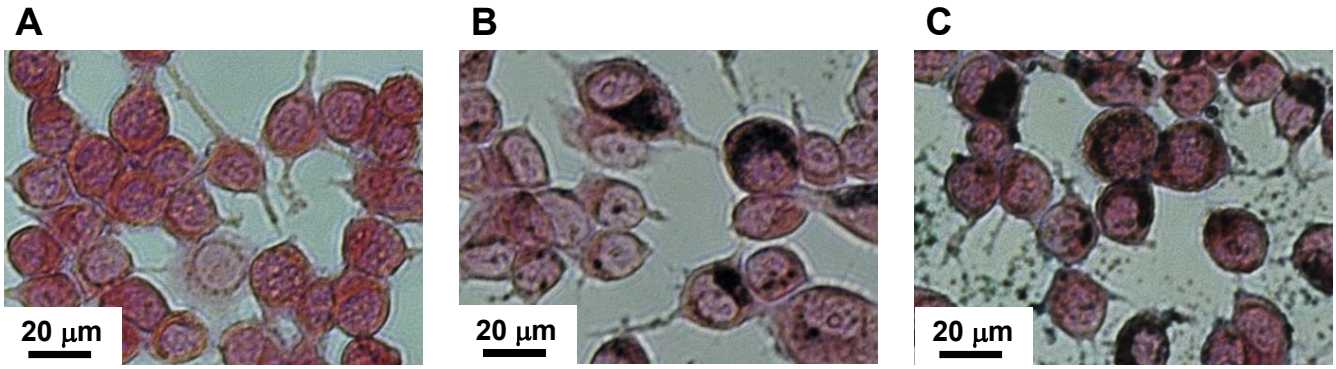

Fig. 4.9 Optical microscopic images of MCF-7 cells without nanoparticles (A), those containing $CoFe_2O_4$ nanoparticles (B), and those containing Fe_3O_4 nanoparticles (C). In these images, cells were stained red whereas nanoparticles were stained blue by iron stain. Reprinted with permission. Copyright @ 2015 Elsevier B. V.

To determine the potential of 10-nm $CoFe_2O_4$ nanoparticles for efficiently inducing cancer cell death, MCF-7 cells with incorporated nanoparticles were subjected to alternating magnetic field (using a 3-turn coil with an outer diameter of 40 mm at 325 kHz and 569.1 A) for 20 min, of which strength was calculated to be 536 Oe. Based on the temperature curves measured for nanoparticles under the AC magnetic field (Fig. 4.10), the temperature of $CoFe_2O_4$ nanoparticles was greater than that of the Fe_3O_4 nanoparticles incubated at the same dose, suggesting that $CoFe_2O_4$ nanoparticles convert the magnetic field into heat more efficiently than did Fe_3O_4 nanoparticles under this condition. Considering the magnetic properties of the nanoparticles (Fig. 4.5) and the amount taken up by the cells (Fig. 4.8), the greater temperature reached by $CoFe_2O_4$ nanoparticles is strongly expected to be attributable to their coercivity, even though the amount of $CoFe_2O_4$ nanoparticles incorporated into a cell was smaller than that of the Fe_3O_4 nanoparticles. Following exposure to the AC magnetic field, the percentage of non-viable MCF-7 cells incubated with every dose of nanoparticles was evaluated by flow cytometry. As shown in Fig. 4.11, 53% cell death could be induced using $CoFe_2O_4$ nanoparticles and the AC magnetic field. On the other hand, Fe_3O_4 nanoparticles did not significantly induce cell death as only 17% of non-viable cells was observed even at the 800 μg dose of nanoparticles. Based on the temperature shown in Fig. 4.11 which is the average temperature measured between 400 and 1200 s in Fig. 4.10, the higher

temperature induced greater cell mortality, which was especially significant when the temperature reached 43°C (critical temperature for cell death). Thus, under the tested conditions, the heat generated by 10-nm $CoFe_2O_4$ nanoparticles under an AC magnetic field was found to be sufficient for human breast cancer cell death.

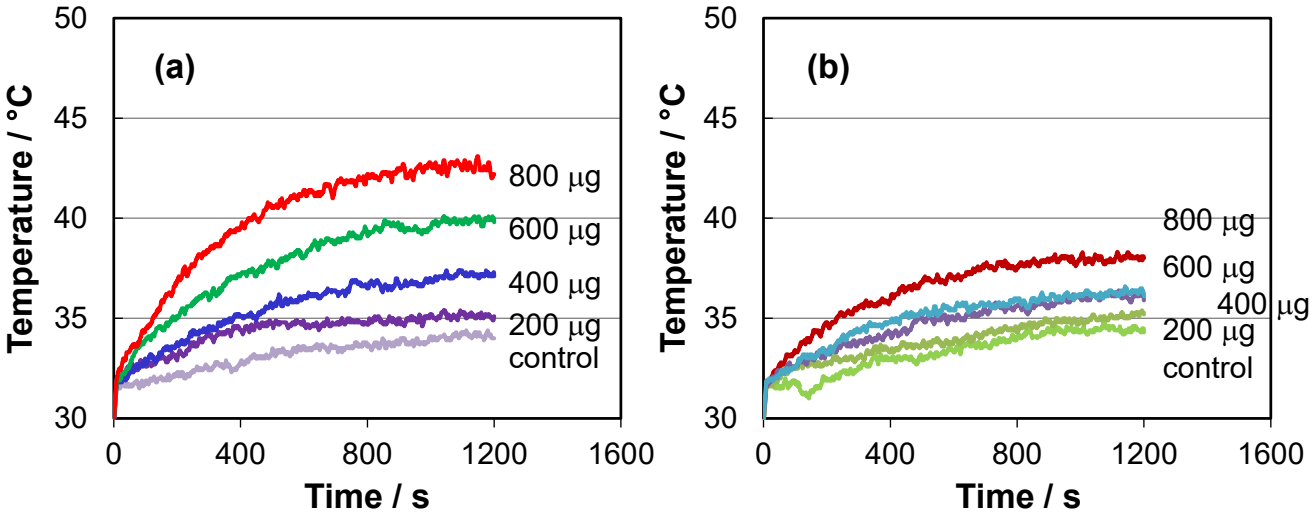

Fig. 4.10 Time dependence of the temperature change in MCF-7 cells containing $CoFe_2O_4$ (a) or Fe_3O_4 (b) nanoparticles under an AC magnetic field (325 kHz, 500 Oe). Control cells were not treated with nanoparticles. The inserted 200, 400, 600, and 800 μg indicate the amount of nanoparticles added to 5×10^5 MCF-7 cells, not the amount of incorporated nanoparticles. Reprinted with permission. Copyright @ 2015 Elsevier B. V.

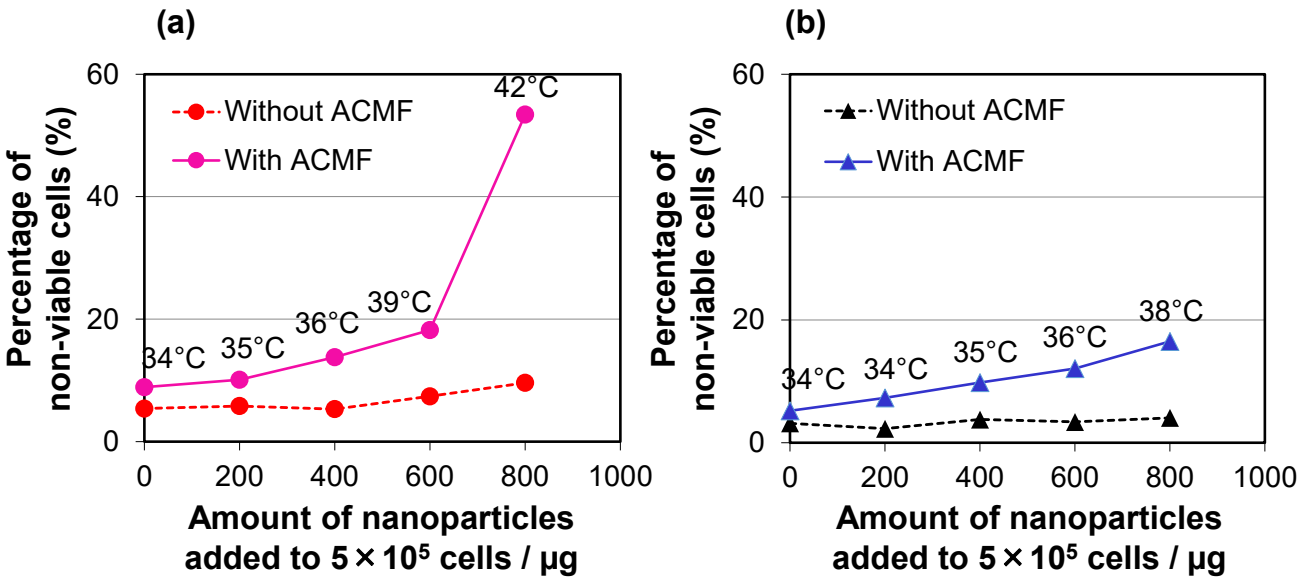

Fig. 4.11 Dependence of the percentage of non-viable MCF-7 cells containing $CoFe_2O_4$ (a) or Fe_3O_4 (b) nanoparticles soon after exposure to AC magnetic field (ACMF; 325 kHz, 500 Oe) for 20 min on the amount of nanoparticles added to 5×10^5 cells. The temperatures indicated are the average temperatures between 400 and 1200 s in Fig. 4.10. Reprinted with permission. Copyright @ 2015 Elsevier B. V.

4.3 $MgFe_2O_4$ nanoparticles

4.3.1 Experimental

Synthesis and characterization of nanoparticles

$MgFe_2O_4$ nanoparticles were synthesized with two steps. In the first step, 24 mL of an aqueous solution containing 0.4 mmol of magnesium chloride ($MgCl_2 \cdot 6H_2O$) and 0.8 mmol of iron chloride ($FeCl_3 \cdot 6H_2O$) was added slowly into a 0.246 M aqueous sodium hydroxide (NaOH) solution (pH 12.4) as a base at room temperature, followed by stirring for 4 h and washing the brown precipitate with water and ethanol. In the second step, the resultant brown powder was annealed at 800°C for 10 min in air with the rate of temperature rise/drop of 20/6 $°C \cdot min^{-1}$ (MFNPs1) or 260/140 $°C \cdot min^{-1}$ (MFNPs2) using an electronic furnance TMF-2200 (Tokyo Rikakikai Co. Ltd., Tokyo, Japan).

$FeCl_3 \cdot 6H_2O$ was purchased from Kanto Chemical Co. Ltd., Tokyo, Japan, $MgCl_2 \cdot 6H_2O$ and NaOH were purchased from Wako Pure Chemical Industries, Ltd., Osaka, Japan.

Characterization of $MgFe_2O_4$ nanoparticles was performed with the same method and procedure described in the previous section 4.2.1, except for using Agilent 5100 ICP-OES (Agilent Technologies, Tokyo, Japan) instead of EDX for the composition analysis of $MgFe_2O_4$ nanoparticles. The mean diameter of nanoparticles was calculated using a equation (2) after counting and measuring diameters (D_n) of fifty nanoparticles in the TEM images.

In vitro *evaluation using MCF-7 cells*

Cell culture, cytotoxicity and cellular uptake study, and evaluation of cell death under AC magnetic field were performed with the same method and procedure described in the previous section 4.2.1, except for the dose amount. In this study, $MgFe_2O_4$ nanoparticles in amounts of 0, 1, 5 mg were added to 5×10^5 MCF-7 cells.

4.3.2 Characterization of nanoparticles

First of all, establishment of synthetic method for single-domain $MgFe_2O_4$ nanoparticles with high crystalline and high magnetism was discussed. When synthesized by directly applied the synthetic method developed for Fe_3O_4 nanoparticles as described in chapter 1.2.4 and 2.2 except for using Mg^{2+} instead of Fe^{2+}, the products was suggested to be a mixture of $Fe(OH)_3$, $Mg(OH)_2$, and $MgFe_2O_4$ with a very small particle size because its XRD pattern showed broad peaks. According to the reports of the synthesis of $MgFe_2O_4$ [12-18], high-temperature treatment is needed to form $MgFe_2O_4$. Hence, to react $Fe(OH)_3$ with $Mg(OH)_2$ (form $MgFe_2O_4$), annealing process was added. In the annealing process, spermine (reactive reagent) was suggested to disrupt the reaction of $Fe(OH)_3$ and $Mg(OH)_2$, NaOH was employed as a base in the co-precipitation method. Annealing temperature and time is also important to obtain the single-domain nanoparticles with high crystalline and without sintering. As a result, 800°C of annealing temperature and 10 min of annealing time were employed in this study.

Fig. 4.12 shows XRD patterns for the products after annealing (MFNPs1 and MFNPs2). The peaks of both particles represent spinel structure and correspond well with the standard pattern of $MgFe_2O_4$ (Cambridge Structural Database (CSD) 9003790). The *d* value of the lattice spacing of (311) was calculated to be 2.531 Å for both samples by using the Bragg equation for the peak observed at $2\theta \sim 41°$, which were similar to the value of commercial $MgFe_2O_4$ (2.526 Å). The formation of Fe_3O_4 or γ-Fe_2O_3 is unlikely as they transform to α-Fe_2O_3 with a corundum structure at 500°C [27]. Although the presence of tiny amount of MgO was suggested for both sample as the MgO was reported to form with the oxidation of $Mg(OH)_2$ at 400°C [28], the formation of MgO seemed smaller for MFNPs2 than for MFNPs1. The formation of MgO is unfavorable but it is not impossible from the aspect of ΔG [29], which suggests that its amount depends on the annealing time. The crystallite size calculated from XRD by applying Scherrer's formula to the (311) diffraction peak was 37 or 39 nm for MFNPs1 or MFNPs2. The composition analysis was investigated by ICP, which indicated the Mg:Fe atomic ratio of 1:2 for both samples.

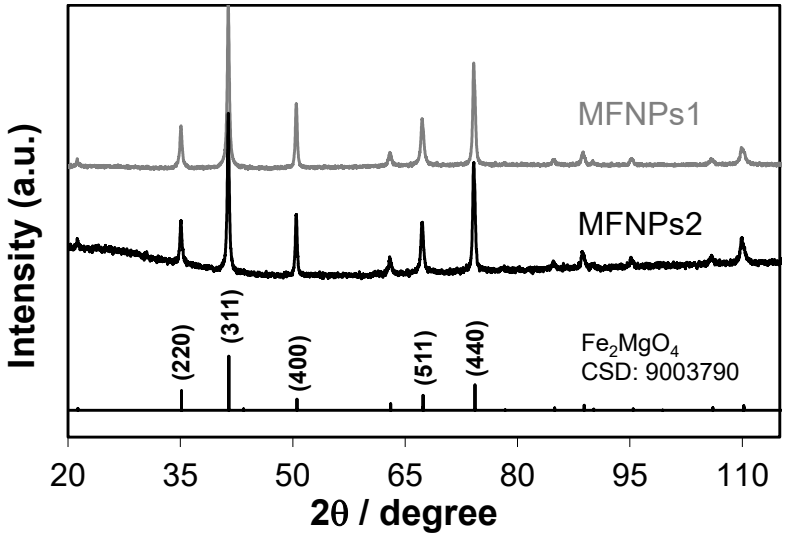

Fig. 4.12 XRD patterns with Co Kα radiation: MFNPs1, MFNPs2, and CSD# 9003790.

Fig. 4.13 shows TEM images of MFNPs1 and MFNPs2, and revealed that both particles were assembled with a shape of spherical or truncated cubic. Fifty nanoparticles were counted to determine their size distribution; the mean particle diameters were 37.0 ± 12.6 nm and 40.8 ± 12.4 nm, shown in Fig. 4.14, respectively. These diameters corresponded to crystallite size calculated from XRD by a Scherrer's formula.

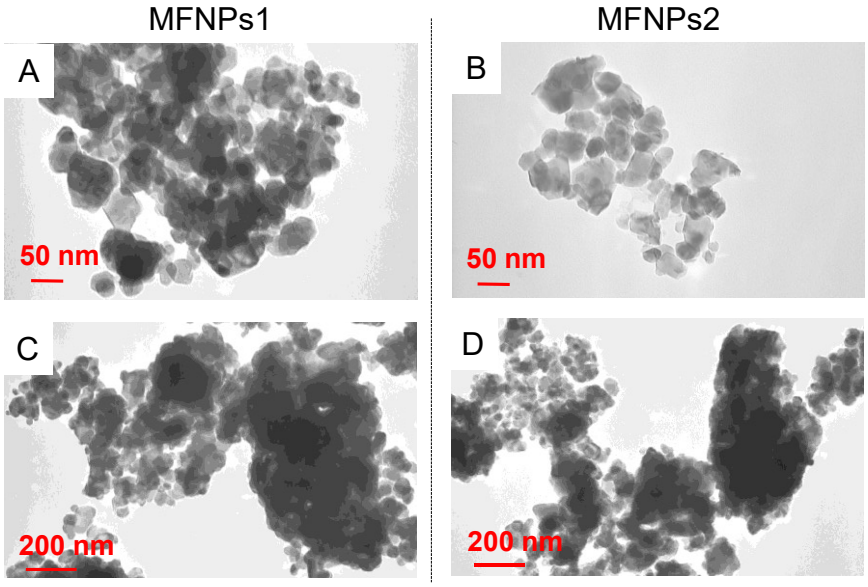

Fig. 4.13 TEM images of MFNPs1 (A,C) and MFNPs2 (B,D). Scale bar: 50 nm (A,B), 200 nm (C,D).

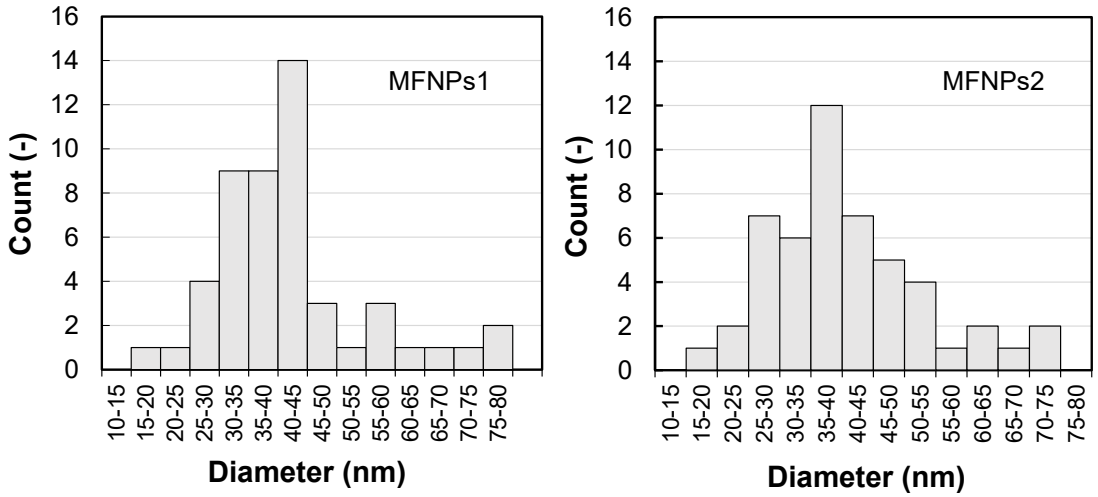

Fig. 4.14 Size distribution of MFNPs1 and MFNPs2.

The size distribution in water was characterized by dynamic light scattering for MFNPs1 and MFNPs2. As shown in Fig. 4.15, MFNPs1 and MFNPs2 were stable in water with forming secondary particles with hydrodynamic diameters of approximately 1000 nm and 100 nm, respectively. Because the zeta potential measured in water at pH 5.8 was -12.6 mV and -6.6 mV for MFNPs1 and MFNPs2, the difference of their dispersity is derived from other interaction forces (not electrostatic repulsive interaction). It is well known that sintering occurs when annealing of particles at high temperature. For MFNPs2, which is annealed with the rapid rate of heating/cooling, the holding time at high temperature is shorter than MFNPs1, suggesting the possibility of the sintering reduction. Hence, this difference of sintering degree may influence the dispersity of $MgFe_2O_4$ nanoparticles.

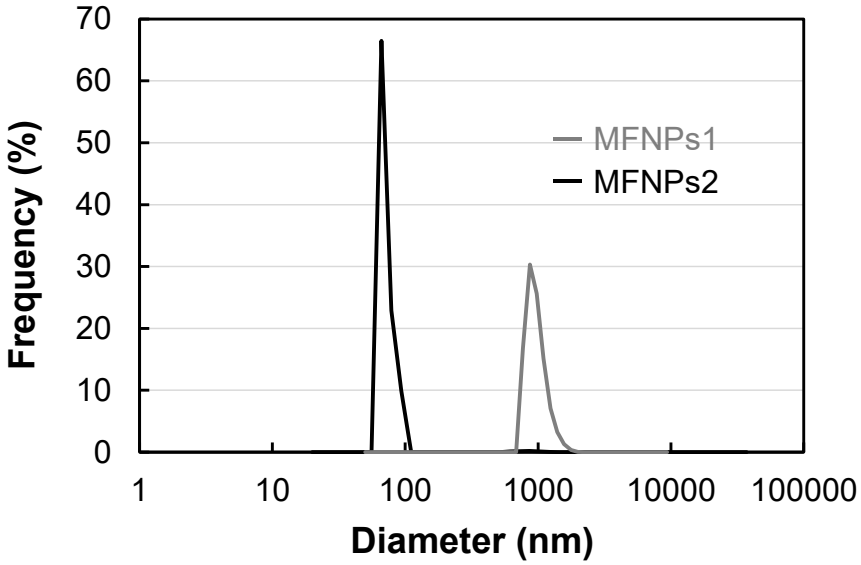

Fig. 4.15 Size distribution of $MgFe_2O_4$ nanoparticles in water characterized by dynamic light scattering.

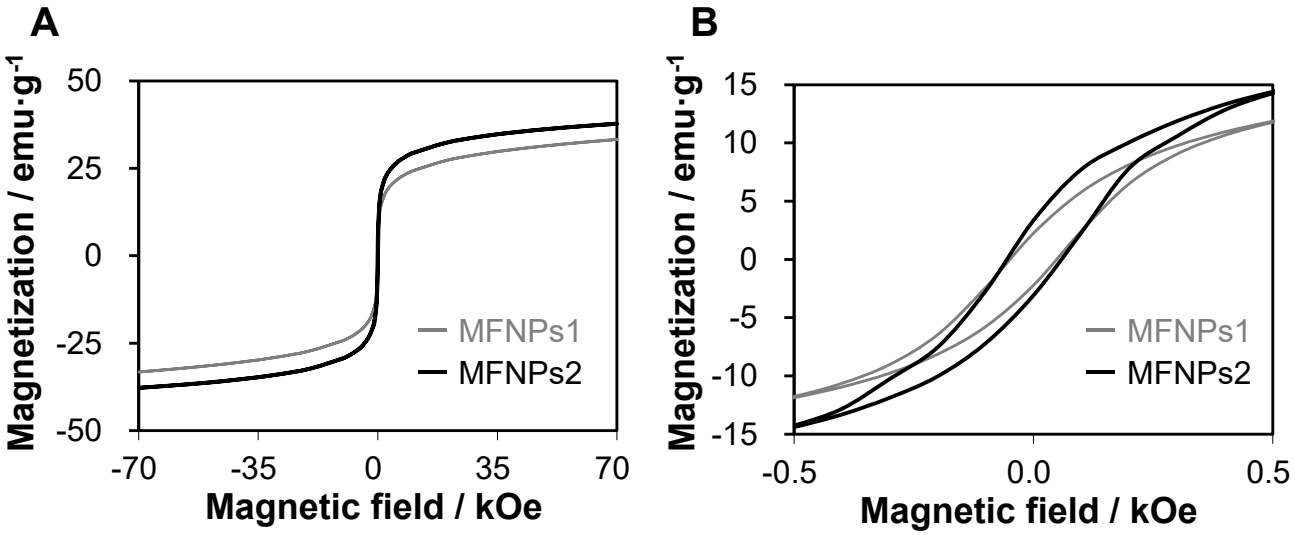

Fig. 4.16 Magnetization curves of $MgFe_2O_4$ nanoparticles. The curves were measured by SQUID at 300 K between -70 kOe and 70 kOe of magnetic field. Curves (B) are extracted from the curves (A) in an applied field range between -500 Oe and 500 Oe.

Fig. 4.16 shows the magnetization curves of MFNPs1 and MFNPs2 at 300 K. As depicted in Fig. 4.16A, the magnetization values at 70 kOe of MFNPs1 and MFNPs2 were found to be 33 and 37 emu/g respectively, which indicated that the rapid rate of heating/cooling increases the saturation magnetization value of $MgFe_2O_4$ nanoparticles due to two supposable reasons. One is the smaller formation of MgO, the other is the increase in the ratio of Mg^{2+} occupied in the A site of spinel structure induced by rapid cooling [30]. Fig. 4.16B is extracted from Fig. 4.16A in an applied field range between -500 Oe and 500 Oe. MFNPs1 and MFNPs2 showed a ferromagnetic behavior with a coercivity of 50 Oe and 60 Oe, respectively. This difference could be influenced by the sintering degree as mentioned above. Overall, the hysteresis area between -500 and 500 Oe for MFNPs2 was approximately 1.5 times greater than that for MFNPs1, as calculated using an Image J software [31].

Fig. 4.17 shows the temperature curve measured for 500 μL of water containing 1 mg of nanoparticles without cells under AC magnetic field (569.1 A, 325 kHz) for 20 min using a 3-turn coil with an outer diameter of 40 mm (the strength of magnetic field was theoretically calculated to be 536 Oe). The temperature of MFNPs2 was higher than MFNPs1, whose average temperature measured between 800 and 1200 s was 39°C and 45°C for MFNPs1 and MFNPs2. From the initial slope of these time-dependent temperature curves in the first 100 s, SARs of 208 and 310 $W \cdot g^{-1}$ was obtained for MFNPs1 and MFNPs2, respectively. The ΔT and SAR of MFNPs2 was about 1.5 times higher than those of MFNPs1, which corresponded the degree of hysteresis-area enhancement as described above.

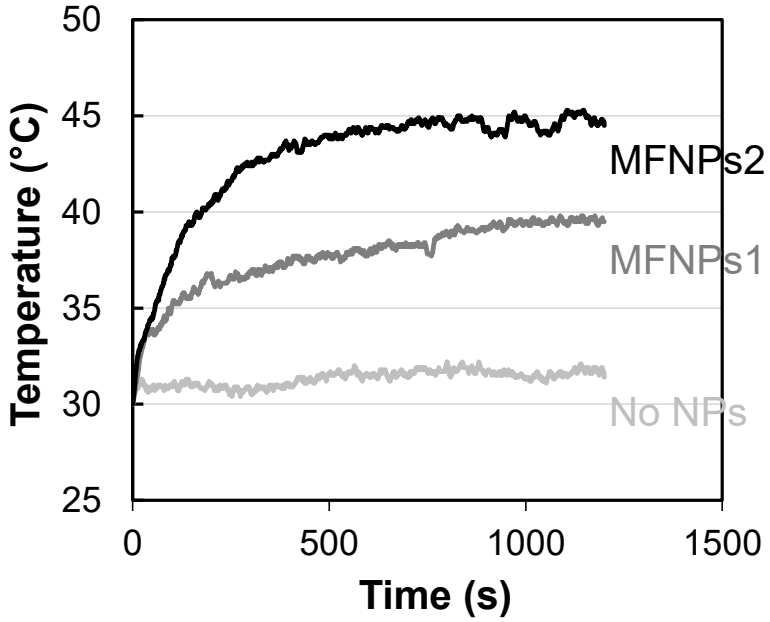

Fig. 4.17 Time dependence of the temperature curve of 1 mg of $MgFe_2O_4$ nanoparticles in 500 μL of water under AC magnetic field (325 kHz, 500 Oe).

4.3.3 Evaluation of cellular uptake and cell death

Using MFNPs2, the influence of nanoparticles on human breast cancer MCF-7 cells. Fig. 4.18 shows the percentage of cells containing nanoparticles (A) and the percentage of non-viable cells (B). As depicted in Fig. 4.18A, the percentage of cells containing nanoparticles tended to increase at the higher doses of both types of particles: 40% of cells incubated with 1 mg reaching 95% of cells incubated with 5 mg. No more than 10% cell mortality was observed following the addition of nanoparticles even at the concentration of 5 mg per 3 mL of medium. For Fe_3O_4 nanoparticles, murine macrophage (J774) cells were induced cell death following incubation with 500 μg/mL of Fe_3O_4 nanoparticles [32]. Therefore, high biocompatibility of $MgFe_2O_4$ nanoparticles was suggested.

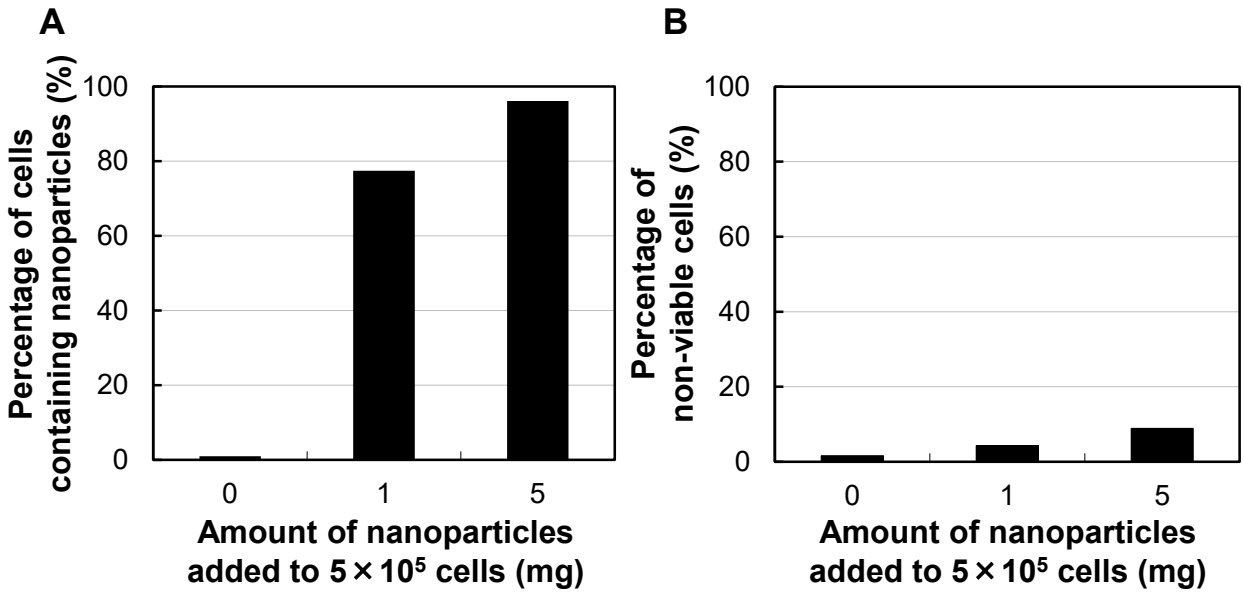

Fig. 4.18 Dependence of the percentage of cells containing nanoparticles (A) and the percentage of non-viable cells (B) on the amount of $MgFe_2O_4$ nanoparticles added to 5×10^5 MCF-7 cells.

Fig. 4.19 shows the dose-dependence of the uptake of $MgFe_2O_4$ nanoparticles by MCF-7 cells. Approximately 1 ng of MFNPs2 was incorporated into a cell at a dose of 1 mg per 5×10^5 cells, and 3 ng of nanoparticles was incorporated per cell at the dose of 5 mg. Compared with other

ferrite nanoparticles, the amount of incorporated nanoparticles for $MgFe_2O_4$ seems to be larger in the range showing high viability.

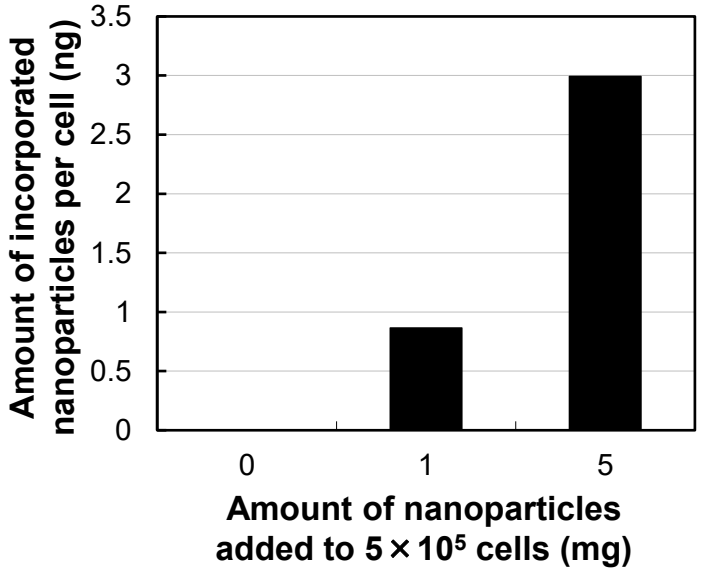

Fig. 4.19 Dependence of the amount of incorporated nanoparticles per cell on the amount of $MgFe_2O_4$ nanoparticles added to 5×10^5 MCF-7 cells.

To determine the potential of $MgFe_2O_4$ nanoparticles for use in magnetic hyperthermia, MCF-7 cells with internalized nanoparticles were subjected to AC magnetic field (325 kHz, 500 Oe) for 20 min. As shown in Fig. 4.20, 90% of cell death could be induced using $MgFe_2O_4$ nanoparticles with a dose of 5 mg and the AC magnetic field. On the other hand, 1 mg of $MgFe_2O_4$ nanoparticles did not significantly induce cell death as 10% of non-viable cells were observed. Based temperature in shown in Fig. 4.20, which is the average temperature measured between 800 and 1200 s in the temperature curves, the higher temperature induced greater cell mortality which was especially significant when the temperature reached >43°C (critical point of cell death). Thus, under the tested conditions, the heat generated by 40 nm $MgFe_2O_4$ nanoparticles annealed with the rapid rate of heating/cooling under AC magnetic field was found to be sufficient for cancer cell death.

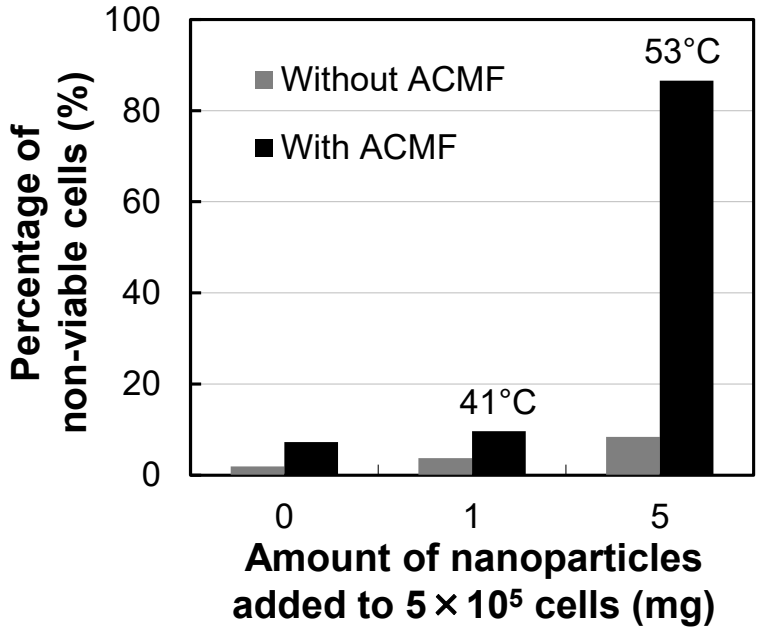

Fig. 4.20 Dependence of the percentage of MCF-7 cells containing $MgFe_2O_4$ nanoparticles soon after 20-min exposure to AC magnetic field (325 kHz, 500 Oe) on the amount of nanoparticles added to 5×10^5 cells. The inserted temperatures are the average temperatures between 800 and 1200 s of samples under AC magnetic field.

4.4 Comparison of heating capacity of MFe_2O_4 nanoparticles

The summary of the characteristics of MFe_2O_4 nanoparticles employed in this thesis is shown in Table 4.3. The AC magnetic field, with a strength of magneticfield of 536 Oe with a frequency of 325 kHz, was applied in this thesis. The concentration of nanoparticles under AC magnetic field was 1 mg of particles dispersed in 500 μL of water.

Table 4.3 Summary of the characteristics of MFe_2O_4 nanoparticles employed in this thesis.

	Fe_3O_4		$CoFe_2O_4$	$MgFe_2O_4$
Size	10 nm	43 nm	9 nm	41 nm
Magnetization (at 10 kOe)	~60 emu/g	~90 emu/g	~60 emu/g	37 emu/g (at 70 kOe)
Coercivity	< 10 Oe	~200 Oe	~200 Oe	~60 Oe
Reached temperature	45°C	63°C	56°C	45°C
SAR (at 100 s)	319 W/g	792 W/g	404 W/g	310 W/g

*Reached temperature was shown as the average temperature between 400-800 s for 10-nm Fe_3O_4 and 9-nm $CoFe_2O_4$, 800-1200 s for 43 nm Fe_3O_4 and 39-nm $MgFe_2O_4$ of their temperature curves under AC magnetic field.

From Table 4.3, it was understood that larger hysteresis area induced higher reached temperature and higher SAR. Hence, although it is difficult to estimate of heating amount exactly because it is affected by the treated environmental conditions etc., the most important characteristics for effective magnetic hyperthermia is suggested to have larger magnetization and larger coercivity in the range of applied magnetic field. This is the reason for showing the highest heating efficacy of 40-nm Fe_3O_4 nanoparticles. However in fact, it was found by *in vitro* evaluation of the interaction of particles and cells that other factors should be also considered. For example, considering to cellular uptake amount and percentage of cells containing nanoparticles, $MgFe_2O_4$ may be more favorable as shown in section 4.3 related to their high biocompatibility.

On the other hand, there is a concern of toxicity in $CoFe_2O_4$ nanoparticles although showing the higher heating efficacy than the same diameter of Fe_3O_4 nanoparticles. <10-nm sized nanoparticles have an advantage of "stealth" effect for phagocytosis by macrophage stayed in the human body.

As mentioned above, determining the most feasible ferrite nanoparticles is difficult due to the involvement of many factors for effective hyperthermia. However, the control of the occupation of the A- and B-sites by transition metal cations (M^{2+} and Fe^{3+}) in spinel structure is suggested to be significant as a future technology to achieve more effective magnetic hyperthermia

4.5 Conclusion

In this chapter, magnetic property of ferrite nanoparticles was controlled in order to increase their heating efficiency and induce cell death effectively under AC magnetic field.

First, synthesis and *in vitro* evaluation of $CoFe_2O_4$ nanoparticles were described. Because they have larger magneto-crystalline anisotropy than Fe_3O_4 nanoparticles, high heating efficacy derived from high coercivity is expected under AC magnetic field. As a consequence, $CoFe_2O_4$ nanoparticles synthesized exhibit greater coercivity than Fe_3O_4 nanoparticles with almost the same diameter. An enhancement of hysteresis area derived from increase in the coercivity was confirmed to cause a higher heating efficiency of nanoparticles under an AC magnetic field. It was also demonstrated that cell death attributable to heat not to cytotoxicity was observed rapidly following exposure to AC magnetic field in MCF-7 cells containing $CoFe_2O_4$ nanoparticles with a diameter of 10 nm, whereas MCF-7 cell death was not induced using 10-nm MNPs under the same conditions.

Second, from the aspect of frequency-dependence of heating efficiency, synthesis and *in vitro* evaluation of $MgFe_2O_4$ nanoparticles were described. Around 300 kHz, which corresponds to the frequency generally used for magnetic hyperthermia, the temperature rise of $MgFe_2O_4$ powder was literature-reported to be highest among other kinds of ferrite powder. As a result, 40-nm $MgFe_2O_4$ nanoparticles with a ferromagnetic property were obtained. Then, MCF-7 cells internalized large amount of $MgFe_2O_4$ nanoparticles, and the temperature rise and 90% of cell mortality was observed when subjected to AC magnetic field, with high biocompatibility.

These results will assist in the design of magnetic nanoparticles as heat elements for magnetic hyperthermia, although further investigation including surface modifications of prevent Co^{2+} elution or improvement of magnetic property of $MgFe_2O_4$ will be necessary. Furthermore, increase in magnetization value of ferrite nanoparticles is also considered to be an effective approach as a method of enhancement of hysteresis area. $MnFe_2O_4$ and $Mn_{0.5}Zn_{0.5}Fe_2O_4$ are candidate to show higher magnetization than Fe_3O_4 nanoparticles from the aspect of amount of magnetic moment. In this situation, considering to biocompatibility of nanoparticles, a study of

$Cu_{0.5}Zn_{0.5}Fe_2O_4$ nanoparticles is now in progress because their saturation magnetization value estimated is also expected to be higher than other ferrite nanoparticles such as Fe_3O_4, $CoFe_2O_4$, and $MgFe_2O_4$.

Controlling magnetic properties of ferrite nanoparticles appropriate to application types is suggested to be important because the remarkable advantage is different among the kinds of ferrite nanoparticles. For increase in heating capacity, the strategy of enhancement of hysteresis area of nanoparticles is feasible. However, there may be a concern that the death of normal cells are also induced even when they internalized a little amount of nanoparticles having a large hysteresis area such as $CoFe_2O_4$. Using nanoparticles with a moderate hysteresis area such as $MgFe_2O_4$, mild hyperthermia can be achieved. Taking advantage of higher coercivity of $CoFe_2O_4$ nanoparticles, effective cell separation is expected. On the other hand, taking advantage of larger amount of internalization with an excellent biocompatibility, effective biotechnology such as internalization of vaccine into dendritic cells enough to activate immune responses (vaccine delivery) [33] is expected.

Overall, although determining the most feasible ferrite nanoparticles is difficult due to the involvement of many factors for effective hyperthermia, control of magnetic properties by the control of the occupation of the A- and B-sites by transition metal cations (M^{2+} and Fe^{3+}) in spinel structure should be significant for increase in therapeutic effect of magnetic hyperthermia.

References

[1] S. Bae et al., "AC Magnetic-Field-Induced Heating and Physical Properties of Ferrite Nanoparticles for a Hyperthermia Agent in Medicine", *IEEE Trans. Nanotechnol.*, 8, 86 (2009).

[2] E. Mazario et al., "Magnetic hyperthermia properties of electrosynthesized cobalt ferrite nanoparticles", *J. Phys. Chem. C*, 117, 11405 (2013).

[3] Y. Oh et al., "*In vitro* study on apoptotic cell death by effective magnetic hyperthermia with chitosan-coated $MnFe_2O_4$", *Nanotechnology*, 27, 115101 (2016).

[4] S. Ayyappan et al., "Effect of digestion time on size and magnetic properties of spinel $CoFe_2O_4$ nanoparticles", *J. Phys. Chem. C*, 113, 590 (2009).

[5] J. Carrey et al., "Simple models for dynamic hysteresis loop calculations of magnetic single-domain nanoparticles: Application to magnetic hyperthermia optimization", *J. Appl. Phys.*, 109, 083921 (2011).

[6] M. R. Phadatare et al., "Enhancement of specific absorption rate by exchange coupling of the core–shell structure of magnetic nanoparticles for magnetic hyperthermia", *J. Phys. D: Appl. Phys.*, 49 095004 (2016).

[7] R. Ghosh et al., "Induction heating studies of Fe_3O_4 magnetic nanoparticles capped with oleic acid and polyethylene glycol for hyperthermia", *J. Mater. Chem.*, 21, 13388 (2011).

[8] J. de Vicente et al., "Stability of cobalt ferrite colloidal particles. Effect of pH and applied magnetic fields", *Langmuir*, 16, 7954 (2000).

[9] K. Konishi et al., "Heating ferrite powder with AC magnetic field for thermal coagulation therapy", *J. Magn. Magn. Mater.*, 272-276, 2428 (2004).

[10] S. H. Pawar et al., "Induction heating studies of combustion synthesized $MgFe_2O_4$ nanoparticles for hyperthermia applications", *J. Magn. Magn. Mater.*, 332, 48 (2013).

[11] M. Suto et al., Heat dissipation mechanism of magnetite nanoparticles in magnetic fluid hyperthermia, *J. Magn. Magn. Mater.*, 321, 1493 (2009).

[12] V. M. Khot et al., "Induction heating studies of dextran coated $MgFe_2O_4$ nanoparticles for magnetic hyperthermia", *Dalton Trans.*, 42, 1249 (2013).

[13] Q. Chen et al., "Synthesis of superparamagnetic $MgFe_2O_4$ nanoparticles by coprecipitation", *J. Magn. Magn. Mater.*, 194, 1 (1999).

[14] C. Liu et al., "Chemical Control of Superparamagnetic Properties of Magnesium and Cobalt

Spinel Ferrite Nanoparticles through Atomic Level Magnetic Couplings", *J. Am. Chem. Soc.*, 122, 6263 (2000).

[15] C.-P. Liu et al., "Comparative study of magnesium ferrite nanocrystallites prepared by sol–gel and coprecipitation methods", *J. Mater. Sci.*, 42, 6133 (2007).

[16] V. M. Khot et al., "Formation, microstructure and magnetic properties of nanocrystalline $MgFe_2O_4$", *Mater. Chem. Phys.*, 132, 782 (2012).

[17] S. Verma et al., "Synthesis of nanosized $MgFe_2O_4$ powders by microwave hydrothermal method", *Mater. Lett.*, 58, 1092 (2004).

[18] D. Chen et al., "Preparation of magnesium ferrite nanoparticles by ultrasonic wave-assisted aqueous solution ball milling", *Ultrasonics Sonochem*., 20, 1337 (2013).

[19] Z. Zi et al., "Synthesis and magnetic properties of $CoFe_2O_4$ ferrite nanoparticles", *J. Magn. Magn. Mater.*, 321, 1251 (2009).

[20] H. Iida et al., "Synthesis of Fe_3O_4 nanoparticles with various sizes and magnetic properties by controlled hydrolysis", *J. Colloid Interface Sci.*, 314, 274 (2007).

[21] R. Hergt et al., "Physical limits of hyperthermia using magnetite fine particles", *IEEE Trans. Magn.*, 34, 3745 (1998).

[22] R. E. Rosensweig, "Heating magnetic fluid with alternating magnetic field", *J. Magn. Magn. Mater.*, 252, 370 (2002).

[23] M. Ma et al., "Size dependence of specific power absorption of Fe_3O_4 particles in AC magnetic field", *J. Magn. Magn. Mater.*, 268, 33 (2004).

[24] I. Catelas et al., "Cytotoxic and apoptotic effects of cobalt and chromium ions on J774 macrophages - Implication of caspase-3 in the apoptotic pathway", *J. Mater. Sci. Mater. Med.*, 12, 949 (2001).

[25] Y.-M. Kwon et al., "Dose-dependent cytotoxicity of clinically relevant cobalt nanoparticles and ions on macrophages *in vitro*", *Biomed. Mater.*, 4, 025018 (2009).

[26] T. Osaka et al., "Effect of surface charge of magnetite nanoparticles on their internalization into breast cancer and umbilical vein endothelial cells", *Colloids Surf. B Biointerfaces*, 71, 325 (2009).

[27] T. Kikuchi et al., "Fine Iron Oxide Powder as a Raw Material of Soft Ferrites", *JFE Technical Report*, 8, 26 (2005).

[28] V. K. Díez et al., "Effect of MgO activation conditions on its catalytic properties for base-

catalyzed reactions", *Catal. Today.*, 173, 21 (2011).

[29] Z. Yan et al., "Hydrothermal synthesis and structure evolution of metal-doped magnesium ferrite from saprolite laterite", *RSC Adv.*, 5, 92778 (2015).

[30] Y. Ichiyanagi et al., Magnetic properties of Mg-ferrite nanoparticles, *J. Magn. Magn. Mater.*, 310, 2378 (2007).

[31] W. S. Rasband, ImageJ, U. S. National Institutes of Health. Bethesda, Maryland, USA. http://rsb.info.nih.gov/ij/ (1997-2014).

[32] S. Naqvi et al., "Concentration-dependent toxicity of iron oxide nanoparticles mediated by increased oxidative stress", *Int. J. Nanomed.*, 5, 983 (2010).

[33] Q. Liu et al., "pH-Responsive Poly(D,L‐lactic-*co*-glycolic acid) Nanoparticles with Rapid Antigen Release Behavior Promote Immune Response", *ACS Nano*, 9, 4925 (2015).

Chapter 5

Application of Fe_3O_4 nanoparticles to cell-separation technology using microalgae

5.1 Introduction

As an example of applications of ferrite nanoparticles, magnetic cell separation was discussed in this chapter. As described in chapter 1, ferromagnetic nanoparticles are required for effective cell separation. Hence, 40-nm Fe_3O_4 nanoparticles were employed in this chapter. The motivations of this chapter are (i) to recover cells from the mixture magnetically (to form flocs of nanoparticles and cells) and (ii) to remove nanoparticles from the flocs. In this study, (i) and (ii) were carried out using microalgae.

Microalgae are a diverse group of unicellular, aquatic, photosynthetic organisms [1]. They have attracted intensive research and development for the production of high-value added products such as biofuels, animal feedstock, recombinant proteins, drugs and chemicals, through solar energy harvesting and carbon dioxide fixation [1-10]. For example of recent research, gene delivery into microalgae using hollow microneedle array was demonstrated [11], which will contribute to future strategy of algae-based industry. However, the high cost associated with the platforms for microalgal biomass production is a significant obstacle for practical commercialization [12]. Harvesting is one of the key elements of microalgal technology that has yet to be optimized for improved economics and efficiency [13]. Various approaches are used for harvesting microalgae, such as centrifugation, flocculation, filtration and flotation [14,15]. Of these approaches, flocculation is a unique method that can be combined easily with other approaches to enhance the speed and efficiency of separation [16,17]. This is especially appealing for microalgal harvesting, where the low cell concentration (few grams per liter) and the small cell size (typically in the order of a few μm) present a serious challenge for effective separation [18].

Flocculation is generally achieved by adding flocculants (or coagulants) that disrupt the repulsive force between particles and allow binding to occur to form flocs [19]. For microalgal cells the repulsive force is electrostatic, due to the surface charge of microalgal cells that are typically negative at physiological conditions [16]. Recently, magnetic nanoparticles (NPs) with positive surface charge have attracted interest as promising flocculants that rapidly adsorb onto the microalgal surfaces, form flocs, and enable rapid, efficient microalgal harvesting through an external magnetic field [14,20].

Important to the success of this magnetic nanoparticle technology is an effective and efficient method for removing the nanoparticles from the microalgae after harvesting, to prevent contamination of the biomass product [19,21]. However, limited studies have been reported to date on the approaches to remove NPs from microalgal flocs. This includes dissolution of the nanoparticles with acid [22], mechanical detachment by ultrasonication or stirring [23,24], and alteration of the electrostatic force by changing the solution pH [25]. An elegant approach was recently reported by Lee et al. and Ge et al. that applies differences in the surface tension of the NPs and microalgae cell surface to adsorb/desorb the NPs from the cell at will [26,27]. Although effective, these methods require complex/expensive steps and/or apply toxic chemicals that can increase the economic cost of the process and raise environmental concerns.

To overcome the issues, this chapter focused on a simple, one-step procedure that applies sedimentation-force through a high-density solution to separate NPs from microalgae after flocculation. The concept is demonstrated for the first time using a model system, where *Chlamydomonas reinhardtii* (*C. reinhardtii*) wild-type cells were flocculated with as-prepared Fe_3O_4 NPs. Also, NPs adsorption to microalgae is described. To adsorb/desorb effectively, ~40-nm Fe_3O_4 NPs and spermine were employed as magnetic NPs and as a coating molecule of NPs. A commercially available, high-density solution (Percoll®) was applied to induce the separation during sedimentation. NP separation was investigated under different solution pH using either centrifugal or magnetic force, and the cell viability after each procedure was assessed with a fluorescence-based assay.

5.2 Experimental

Synthesis of magnetite nanoparticles

Fe_3O_4 NPs with a diameter of 40 nm were synthesized by the same method described in the chapter 2. Briefly, 50 mL of aqueous solution containing 0.125 M of spermine (Sigma-Aldrich Japan, Japan) was prepared as base and protective reagent for NP synthesis. 50 mL of 0.05 M of $FeCl_2 \cdot 4H_2O$ (Kanto Chemical Co. Ltd., Japan) aqueous solution was added to the spermine solution and stirred for 4 h at room temperature. The resulting black precipitate of Fe_3O_4 NPs was collected, washed with water and ethanol, and dried before use.

Microalgae cultivation

CC124 cells, a catalogue for the wild-type strain of *C. reinhardtii* microalgae, were obtained from the Chlamydomonas Resource Center at the University of Minnesota. All chemicals were used as received from Fisher Scientific, unless stated otherwise. CC124 cells were grown in 10 mL of TAP media that was rocked in 50 mL Erlenmeyer flasks under moderate light [28]. The cells were collected during exponential growth phase, and when the concentration reached 5.0×10^6 cells/mL. Cell counting was performed using a TC20 cell counter (Bio-Rad, USA).

Zeta potential measurement and NP adsorption to CC124 cells

NPs or CC124 cells were dispersed in TAP media for the zeta potential measurement. Approximately 2 mL of the NP or CC124 suspension was assessed with electrophoretic light scattering, using a 90 Plus Zeta Particle Size Analyzer (Brookhaven Instruments Corporation, USA). Zeta potential was calculated using the properties for aqueous solution pre-recorded in the instrument software: *i.e.,* 0.890 cP, 1.330, and 78.54 for the viscosity, reflective index and dielectric constant, respectively.

To adsorb the NPs to CC124 cells, 1 mg of NPs and 7.5×10^6 of CC124 cells were mixed in 5 mL of TAP culture media and stirred at 1000 rpm for 15 min. The cells were used immediately after NP adsorption.

For all experiments, the pH of the TAP media was adjusted as needed using 0.5 M HCl or 0.5 M KOH.

Cell sedimentation

Percoll® (GE Healthcare, USA) was diluted to 35 vol% or 50 vol% with TAP media. From the manufacturer's specification, the as-received Percoll® has a density of 1.130 ± 0.005 g/mL. Assuming the density of TAP media to be about 1 g/mL, the final density of Percoll® after dilution to 35 and 50 vol% is calculated to be 1.046 and 1.065 g/mL, respectively. The viscosity of TAP media and the diluted Percoll® solution was measured using a Cannon-Fenske Routine Viscometer (Cannon instrument company, USA). 1 mL of the TAP media containing 1.5×10^6 of CC124 cells (with or without NP adsorption) was layered carefully onto 1 mL of 35 or 50 vol% Percoll®. The layered solution was then either centrifuged at 1500 × g or 2000 × g for 5 min, or placed on a ferrite magnet for 10 min to allow sedimentation. The average magnetic field of the magnet was measured to be 1500 Oe using a 6010 model Gaussmeter (Bell Technologies Inc., USA). After sedimentation, the sample was used immediately for image analysis.

Cell viability assay

Fluorescein diacetate (FDA) and propidium iodide (PI) were purchased from MP Biomedicals Inc. and Alfa Aesar, respectively. The dye solution, which is 1 μL of 10 mg/mL FDA in dimethyl sulfoxide and 10 μL of 1 mg/mL PI in water, was added into 1 mL of TAP media containing 1.5×10^6 of CC124 cells (with or without NP adsorption), and incubated for 20 min. After incubation, the cells were imaged immediately with a fluorescence microscope to assess their viability.

Image analysis

The samples were imaged with an epifluorescence microscope (Axio Imager M2m Motorized Microscope, Carl Zeiss, Germany). ImageJ software from NIH was used to analyze the obtained images [29]. One hundred particles (either individual cells, flocs or background contamination) were investigated to assess the distribution of particle size and the relative adsorption quantity,

Q_{rel}, which we define here as:

Equation 1 $$Q_{\mathrm{rel}} = \left(A_{\mathrm{projected}} - A_{\mathrm{red}}\right)/A_{\mathrm{red}}$$

where $A_{\mathrm{projected}}$ is the projected area of an arbitrary particle, and A_{red} is the projected area of red fluorescence observed within that particle. Histogram data was fitted to a Gaussian distribution using Origin software (OriginLab Corporation, USA).

5.3 Flocculation of nanoparticles and microalgae

Flocculation is induced by four major mechanisms: double-layer compression, sweep flocculation (or colloid entrapment), adsorption-induced charge neutralization, and adsorption-induced interparticle bridging [30]. Double-layer compression is a function of the ionic concentration of the solution. Since the ionic concentrations of the solution between our samples are comparable, the effect of double-layer compression is expected to be minimal. Sweep flocculation is also not expected due to the absence of chemical precipitation, and hence the two adsorption-induced mechanisms are the dominant mechanisms of flocculation in this study's system.

Adsorption of NPs to CC124 cells can occur through concurrent contributions of van der Waals, dielectric, and electrostatic forces [31]. In particular, it has been shown that electrostatic force is the major force that determines the interaction between the cells and freshwater microalgae (*e.g.,* CC124) and NPs [32]. Electrostatically-controlled flocculation is commonly accomplished by changing the zeta potential of NPs, ζ_{NP}, and microalgae, ζ_{algae}, with solution pH [20]. Flocculation of NP-adsorbed CC124 cells is expected to be the most significant when attractive electrostatic force is at maximum (*i.e.,* sum of the magnitude of the zeta potential, $\sum|\zeta|$, is maximum at $\zeta_{\mathrm{NP}}\zeta_{\mathrm{algae}} < 0$), and the least effective when repulsive electrostatic force is maximum (*i.e.,* maximum $\sum|\zeta|$ at $\zeta_{\mathrm{NP}}\zeta_{\mathrm{algae}} > 0$).

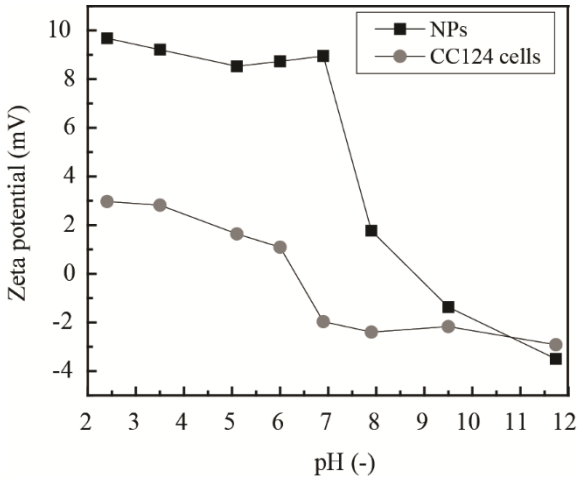

Fig. 5.1 Effect of pH on zeta potential of Fe_3O_4 NPs and CC124 cells. Reprinted with permission. Copyright @ 2016 Elsevier B. V.

Fig. 5.1 plots the zeta potential of NPs and CC124 cells as a function of solution pH. ζ_{NP} was generally more positive than ζ_{algae}. The positive ζ_{NP} observed below the isoelectric point (IEP) of pH 8.8 is attributed to the protonation of amine groups from spermine molecules coating the NPs. The negative ζ_{NP} above IEP have been attributed to the formation of FeO–O^- groups [22,33]. pH has also been reported to effect the protonation of the functional groups on microalgal cell surface and thereby change ζ_{algae} [22,34]. Indeed we observed change in ζ_{algae} with pH with IEP at pH 6.3. Based on Fig. 5.1, the strongest NP-CC124 adsorption is expected to occur at pH 7.0, and the weakest at pH 2.4.

Optical microscope images were taken to assess the effect of electrostatic force on NP-CC124 flocculation (Fig. 5.2). Figure 5.2a are images from CC124 cell solution containing no NPs (control). The top row shows auto-fluorescence (colored red) from the chlorophyll of CC124 cells. The chlorophyll is also observed in the transmitted light image as dark grey particles (Fig. 5.2a, second row). The grey particle that does not overlap with a red fluorescence (highlighted with a circle) is an artifact, and in the control sample, it depicts the background impurity inherent to the experiment.

Fig 5.2b and c are images of CC124 cells after stirring in NP-containing TAP media, at pH 2.4 (weak binding) and 7.0 (strong binding), respectively. In the transmitted light images, the opaque NPs form sub-micron sized aggregates, and are observed as black particulates with no fluorescence. It is confirmed from the transmitted light images that, in contrast to Fig. 5.2a, the CC124 cells in Figure 2b and c are coated by black NP aggregates, and forming flocs bigger than the naked CC124 cells. In particular, the larger flocs at pH 7.0 showed multiple CC124 clusters embedded within a matrix of NPs, indicating significant interparticle-bridging between negatively-charged CC124 cells and positively-charged NPs.

To gain a quantitative measure of this observation, a histogram of the projected area of each particle, $A_{\mathrm{projected}}$, was prepared from the transmitted light image (Fig. 5.2, bottom row). These histograms delineate the effect of electrostatic force between the NPs and the CC124 cells on floc formation. The peak of the histogram, A_{peak}, and the full width at half maximum of the peak (FWHM) were obtained by fitting the histograms to a Gaussian distribution.

The A_{peak} and FWHM of the control sample (naked CC124 cells) were 127 μm^2 and 78 μm^2, respectively. When NP-CC124 flocculation was induced at pH 2.4 and pH 7.0, A_{peak} increased to

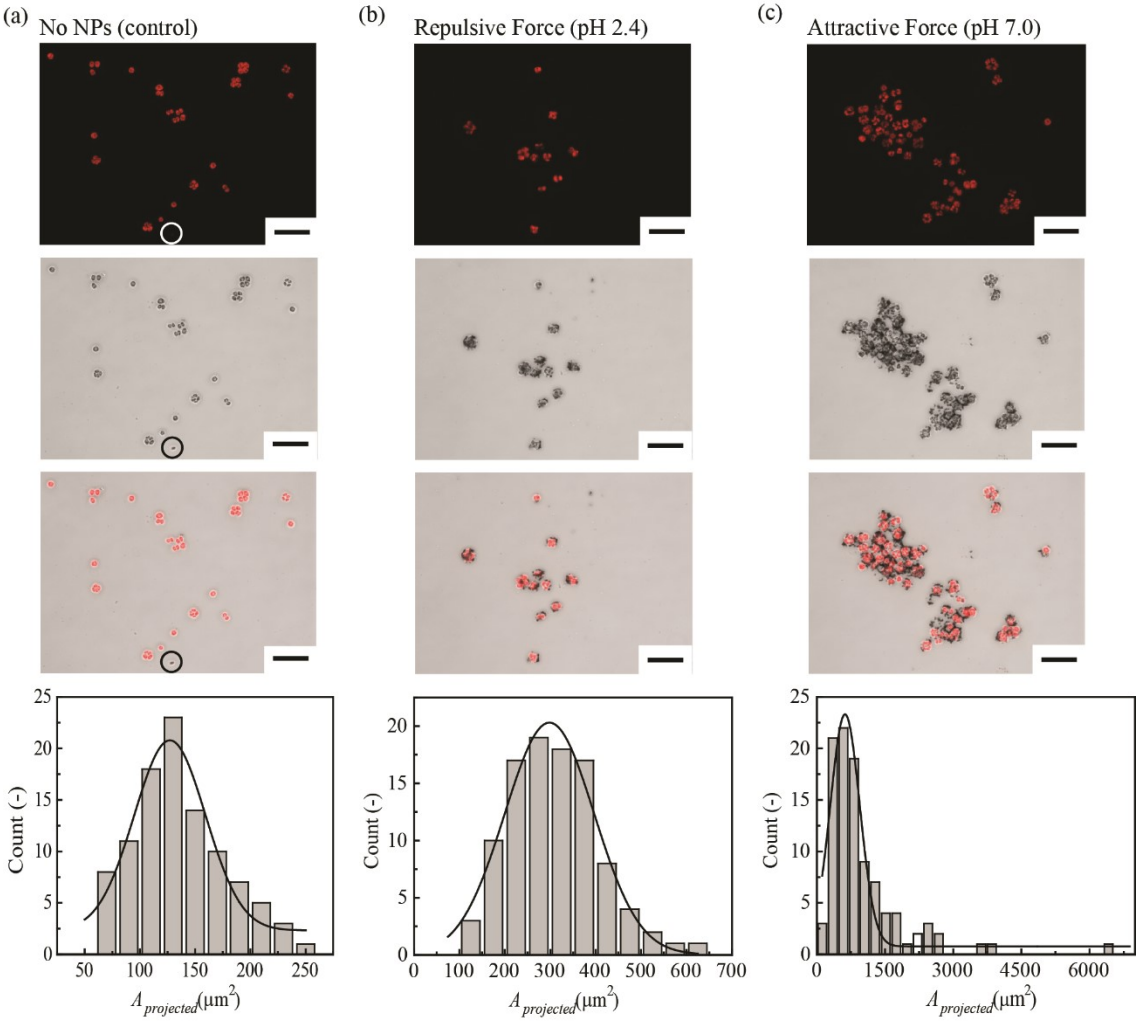

Fig. 5.2 Optical micrograph images and histogram of NP-CC124 flocculation. (a) CC124 in TAP media without NPs (control), (b) with NPs at pH 2.4 and (c) at pH 7.0. The first, second and third rows are images taken at the same location showing fluorescence, transmitted light, and fluorescence superimposed on transmitted light, respectively. The circles in Fig. 5.2a highlight an example of an artifact (particle with no fluorescence). All scale bars in the figure represent 50 μm. The histograms in the bottom row show the size distribution of the imaged particles. Solid lines indicate the Gaussian distribution fit for each histogram. Reprinted with permission. Copyright @ 2016 Elsevier B. V.

298 and 619 μm^2, respectively, as expected from the images of the flocs in Fig. 5.2b and c. A

significant increase in FWHM values (232 and 767 for pH 2.4 and pH 7.0, respectively) was also confirmed, which indicates the polydispersity of the floc size.

The relative quantity of NPs contained within individual flocs was assessed by calculating Q_{rel} from fluorescence images (Equation 1). The Q_{rel} values were 0.0 ± 0.1, 0.7 ± 0.5 and 1.9 ± 0.8 for the control, pH 2.4 and pH 7.0 images, respectively. A Q_{rel} value of zero is equivalent to all flocs containing no NPs, as expected for the control sample. Values of Q_{rel} for pH 2.4 and pH 7.0 are significantly larger than that of the control, indicating significant adsorption of NPs onto CC124 cells. The Q_{rel} of pH 7.0 was the largest, indicating the effective increase in NP content within the flocs, again depicting the occurrence of adsorption-induced interparticle bridging mechanism under attractive electrostatic force.

5.4 Removing nanoparticles from microalgae

Forces that act on centrifuged spherical particles are buoyancy force, F_B, drag force, F_D, and centrifugal force, F_C [16,35]:

Equation 2. $$F_B = V_p \rho_s \times RCF$$

Equation 3. $$F_D = 6\pi r \eta v$$

Equation 4. $$F_C = m_p \times RCF$$

where V_p is the volume of the particle, ρ_s is the density of solution, RCF is the relative centrifugal force, r is the radius of the particle, η is the viscosity of the solution, v is the velocity of the particle, and m_p is the mass of the particle. In this study, the NPs are aggregated and move faster than CC124 cells. This is attributed to the smaller size of the NP aggregates that result in smaller F_B and smaller F_D, allowing the NPs to move through the solution with less hindrance compared to the CC124 cells.

Within a NP-CC124 flocculate, the differences in the net forces between NPs and CC124 cells during centrifugal sedimentation will induce a tensile force between the NPs and CC124 cells. We hypothesized that such tensile force can be used to separate NPs from adsorption-induced NP-CC124 flocs, offering a simple avenue to recover NPs from the microalgal flocs.

To test this hypothesis, a simple bi-layer setup was prepared as illustrated in Fig. 5.3a. TAP media containing green CC124 cells (with or without NPs) is layered above an aliquot of transparent Percoll®. Percoll® is a solution containing colloidal silica coated with polyvinylpyrrolidone and is commonly used for biological centrifugal separation. Here, it was used as a representative high-density solution where ρ_s is ~1.046 g/mL (see section 5.2). η was also higher than the TAP media (1.02 and 1.16 cP for TAP media and 35 vol% Percoll®, respectively). As depicted in Equation 2 and Equation 3, higher ρ_s increases F_B and higher η increases F_D. Hence centrifugal sedimentation of particles through 35 vol% Percoll® will be more hindered compared to similar sedimentation through the TAP media.

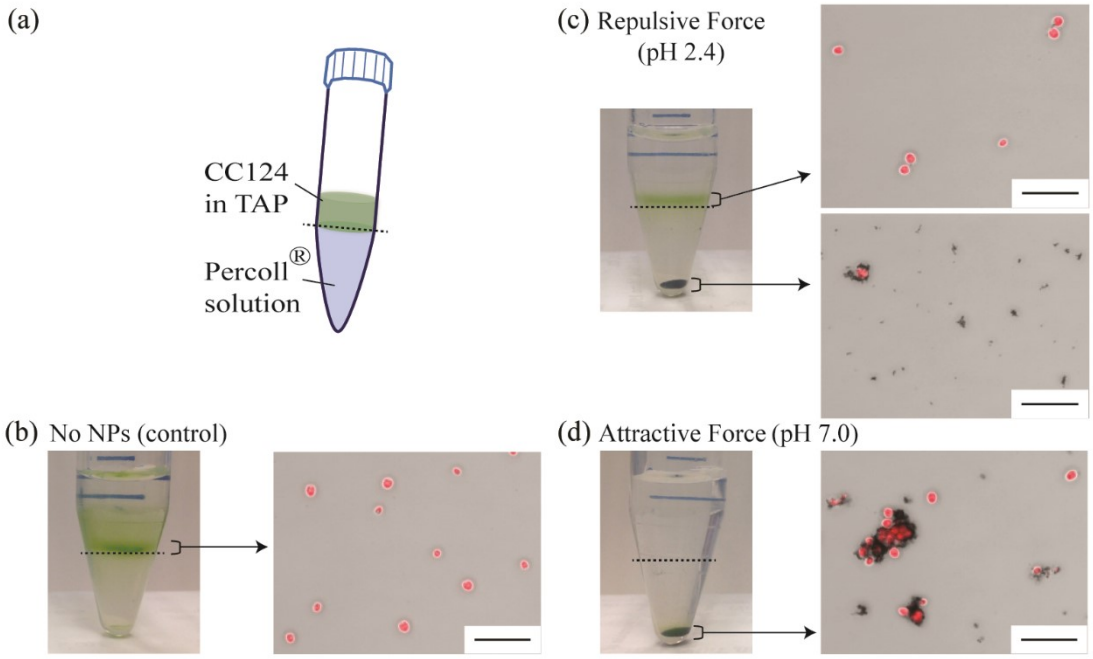

Fig. 5.3 Effect of centrifugal sedimentation on cell sedimentation with and without NPs. The samples were centrifuged at 1500 × g with 35 vol% Percoll® for 5 min. (a) Illustration of the bi-layer setup. (b) Images of the CC124 cells with no NPs (control), (c) NPs adsorbed to CC124 at pH 2.4, and (d) at pH 7.0. The right panels of (b), (c) and (d) are fluorescence images superimposed onto transmitted light images. All scale bars represent 50 µm. Reprinted with permission. Copyright @ 2016 Elsevier B. V.

Fig. 5.3b shows the result from the control experiment, where NPs were not present. A distinct green band is observed at the interface between the TAP media and Percoll® (depicted by the dotted line), and microscopy images confirm the CC124 cells dispersed in this band. This indicates that the sum of F_D and F_B of the naked CC124 cells in the Percoll® layer are comparable or equal to F_C, effectively hindering or preventing the CC124-cell sedimentation through the Percoll® layer.

When CC124 cells with NPs adsorbed at pH 2.4 was centrifuged under the same condition (Fig. 5.3c), we found a black pellet at the bottom of the centrifugal tube, and a green band around the TAP/Percoll® interface. Fluorescent and transparent light imaging confirmed that the black pellet was NP aggregates with a few red (fluorescent) CC124 cells, and the green band consisted

only of naked CC124 cells. This result demonstrates that NPs can sediment through the Percoll® layer, despite the increased F_D and F_B, while the naked CC124 cells cannot. Furthermore, it indicates that the adsorption force was smaller than the tensile force induced between the NPs and the CC124 cells, resulting in the separation of NPs from the microalgal flocs. Indeed, Q_{rel} of the algae in the green layer was 0.0 ± 0.2, indicating that NPs were effectively removed from all the CC124 cells in the green layer using this sedimentation process.

On the other hand, when NPs were adsorbed at pH 7.0, no green/transparent interface was observed, and instead a green-tinted black pellet was found at the bottom of the tube (Fig. 5.3d). This suggests that the adsorption force was larger than the tensile force, allowing the NPs to drag the CC124 cells through the dense Percoll® layer without disintegration (or desorption). Microscopy imaging of the pellet also supports this case, showing large aggregates with clusters of CC124 cells embedded within the NP matrix with a Q_{rel} of 1.5 ± 0.9. The difference in Q_{rel} before and after centrifugation indicates a decrease of about 20% in NP adsorption per floc. This may be attributed to the separation of NPs that were part of the floc but were located relatively far from the CC124 cells, and hence experienced less electrostatic attractive force with the cells.

The key to successful NP removal from microalgae using the sedimentation-based approach is to induce a sufficient difference in the net force between the NPs and the CC124 cells. One way to achieve this is to increase the η and ρ_s of the bottom (*i.e.,* Percoll®) layer. Due to the larger radius of CC124 cells, the effect of increased η and ρ_s on F_B and F_D are more significant than the NPs (see Equation 2 and Equation 3). Therefore, the CC124 cells are subjected to a larger increase in resistance for moving in the direction of F_C, and as a result, a larger tensile strength between the NPs and the CC124 cells is expected to be induced.

To demonstrate this aspect, an experiment similar to the one depicted in Fig 5.3 was performed, but using 2 mL of Percoll® with an increased concentration of 50 vol%. The higher concentration results in higher ρ_s and η of 1.065 g/mL and 1.244 cP, respectively. RCF was also increased from 1500 to 2000 × g to enhance the rate of separation. As expected, the control sample without NPs resulted in a formation of green band around the TAP/Percoll® interface, indicating that CC124 cells were unable to pellet down under the applied condition (Fig. 5.4a). At pH 2.4, where

the electrostatic force between the NPs and CC124 cells was strongly repulsive, we saw separation of NPs from the microalgal floc (Fig. 5.4b), consistent with what was observed for 35 vol% Percoll® at 1500 × g (Fig. 5.3c). However, in this modified experiment separation was also confirmed from the flocculation that was strongly bound by the electrostatic attractive force at pH 7.0 (Fig. 5.4c). This confirms that sedimentation-induced tensile force through high-density, high-viscosity solution is an effective approach to recover the ferromagnetic NPs from microalgal flocs, even under the physiological condition that causes strong electrostatic attraction.

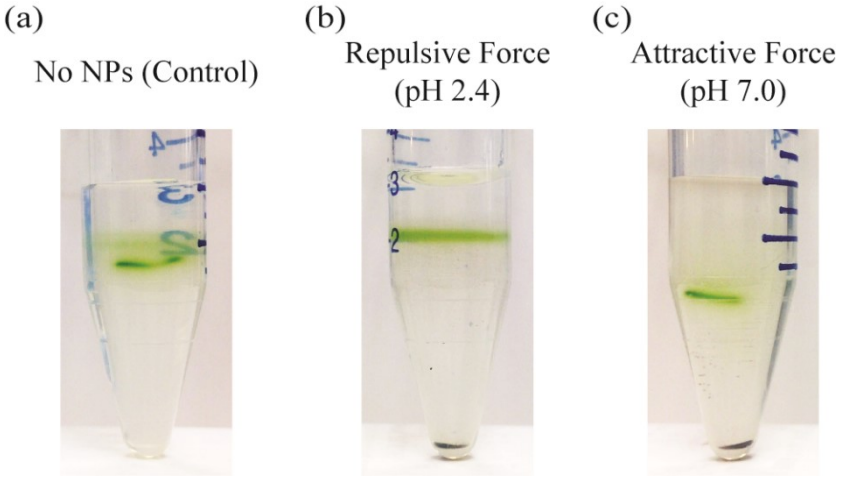

Fig. 5.4 Effect of centrifugal sedimentation on NP-CC124 flocs at 2000 × g with 50 vol% Percoll® for 5 min. (a) Images of the CC124 cells with no NPs (control), (c) NPs adsorbed to CC124 at pH 2.4, and (d) at pH 7.0. Reprinted with permission. Copyright @ 2016 Elsevier B. V.

A similar mechanism can applied for recovering NPs from microalgal flocs using magnetic-field-based sedimentation, which is economically more desirable for large-scale production than centrifugation-based sedimentation [20,36]. For the magnetic-field-based sedimentation, Equation 4 will be substituted by the magnetic force experienced by the particles, F_M [37,38]:

Equation 5. $$F_M = 4/3 \times V_M(\vec{M} \cdot \vec{\nabla})\overrightarrow{B_0}$$

where V_M is the magnetic volume of the particle, $\vec{M}$ is the magnetization of the particle per unit

volume, and $\overrightarrow{B_0}$ is the externally-applied magnetic field.

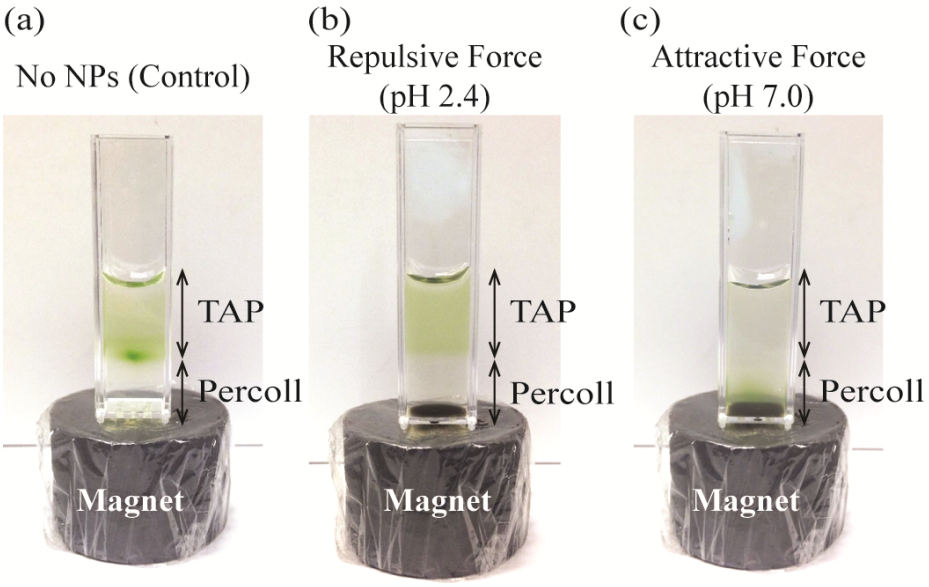

Fig. 5.5 Effect of magnetic force on separation of NPs from microalgal flocs. (a) Images of the CC124 cells with no NPs (control), (b) NPs adsorbed to CC124 at pH 2.4, and (c) at pH 7.0. Reprinted with permission. Copyright @ 2016 Elsevier B. V.

Fig. 5.5 are images of cuvettes containing the TAP/Percoll® bi-layer and CC124 cells with and without NPs. The cuvette was placed on a ferrite magnet to induce magnetic sedimentation. The results were comparable with the centrifugal-sedimentation studies described above (Fig. 5.3). The control sample formed a distinctive green/transparent interface at the surface of the Percoll® layer, indicating little penetration of green CC124 cells into the Percoll® (Fig. 5.5a). NP-CC124 flocs formed at pH 2.4 were disintegrated into a green layer above Percoll® and a black precipitate at the bottom of the vial. This confirms that magnetically-induced tensile force is also an effective approach to recover the ferromagnetic NPs from the microalgal flocs. However, a green TAP/Percoll® interface was not observed at pH 7.0, and the majority of the green cells were magnetically pulled down to the bottom of the vial. This may be attributed to the smaller F_M relative to the F_C applied in Fig. 5.4, and could be circumvented by using a different magnet with

higher F_M, or further increasing the ρ_s and η of the high-density layer solution.

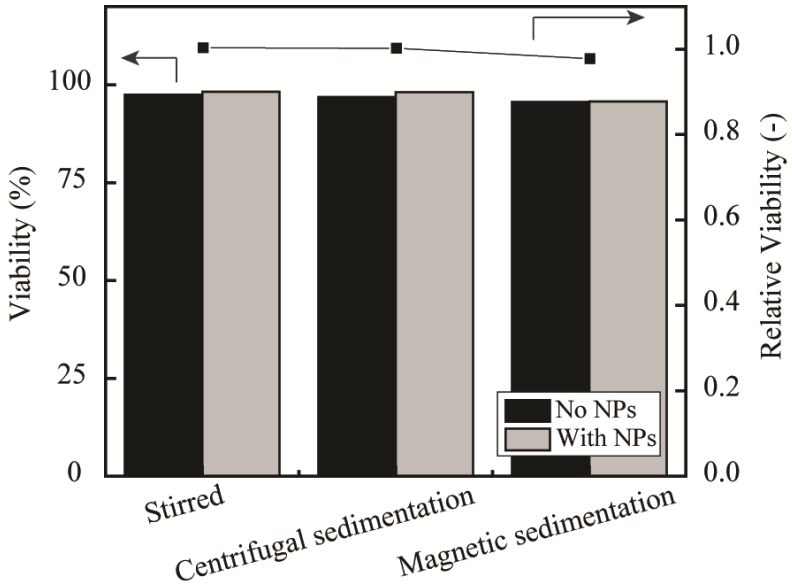

Fig. 5.6 Effect of NPs and sedimentation treatments on CC124 cell viability (pH 7.0). Reprinted with permission. Copyright @ 2016 Elsevier B. V.

Finally, we investigated the effect of NP adsorption and Percoll®-layered sedimentation on CC124 cell viability using the well-established FDA/PI dual fluorescence assay (Fig. 5.6) [11]. Briefly, FDA fluoresces when exposed to viable cells, and PI fluoresces when exposed to dead cells. The column in Fig. 5.6 correspond to the left ordinate and indicate the percentage of cells that showed fluorescence from FDA and not from PI (Equation 6).

Equation 6.

$$\text{Viability (\%)} = \frac{\text{Number of FDA positive and PI negative cells}}{\text{Number of total cells}} \times 100$$

The points in Fig. 5.6 correspond to the right ordinate and indicates the ratio between the initial viability (before exposure to NPs) and the viability after the step indicated in the abscissa (Equation 7).

Equation 7.

$$\text{Relative viability } (-) = \frac{\text{Viability after specified step}}{\text{Viability before NP exposure}}$$

where the viability before NP exposure was 98%. From the figure, it is confirmed that the cytotoxicity of NP adsorption, centrifugal and magnetic sedimentation, and exposure to the Percoll® was minimal (viability > 96%) and the majority of the cells stayed viable throughout the whole process.

5.5 Conclusion

This research demonstrates that sedimentation through a higher-density, higher-viscosity solution than cell media enables effective removal of Fe_3O_4 NPs from microalgal flocs. First, the flocs of nanoparticles and cells were successfully formed using an attractive electrostatic interaction between them. The larger-sized CC124 cells experience larger drag and buoyancy force than the smaller-sized NPs, which induces tensile force between the NPs and CC124 cells. When the tensile force overcomes the attractive forces forming the floc, NPs detach and form pellets at the bottom of the solution, while CC124 cells float as a green band mid-way in the solution. Sedimentation by both centrifugal and magnetic (just at pH 2.4) forces achieved NP removal, and the cytotoxicity of this procedure on CC124 cells was below 4%.

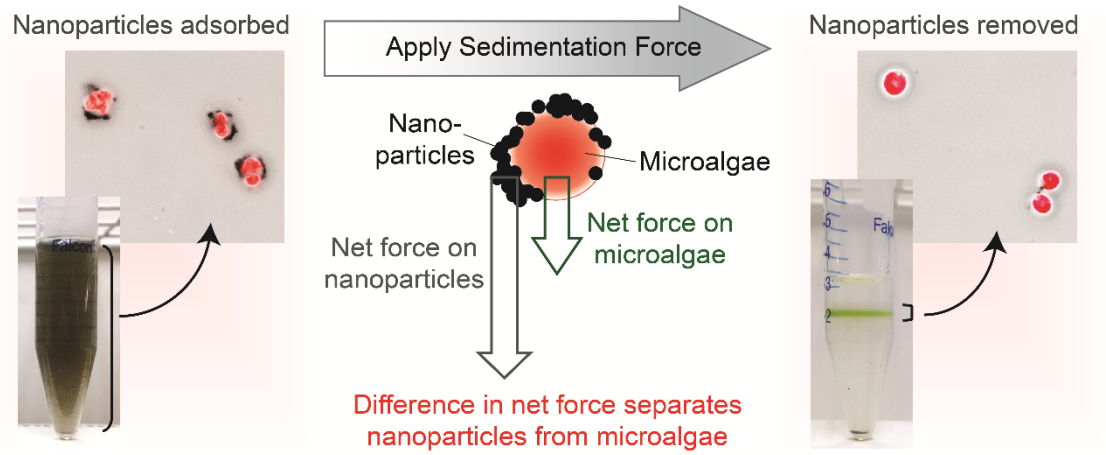

Fig. 5.7 Figure conclusion in chapter 5. Reprinted with permission. Copyright @ 2016 Elsevier B. V.

Figure conclusion was shown in Fig. 5.7. This approach offers significant opportunity for purifying microalgal biomass after nanoparticle-flocculation-based harvesting, and for decreasing the cost of microalgal biotechnology. This may also find avenues in other applications that applies flocculation; such as algal biofilm formation in photobioreactors and wastewater treatment. As a future work, separation of NPs from microalgal flocs by magnetic force at pH 7 should be achieved. Of which, using a magnet with stronger magnetic properties and using NPs with a higher coercivity such as $CoFe_2O_4$ instead of Fe_3O_4 may be effective approaches.

References

[1] A. Hallmann, "Algal Transgenics and Biotechnology", *Transgenic Plant J.*, 1, 81 (2007).

[2] S. P. Mayfield et al., "Advances in microalgae engineering and synthetic biology applications for biofuel production", *Curr Opin Chem Biol.*, 17, 489 (2013).

[3] A. K. Davis et al., "Metabolic and cellular organization in evolutionarily diverse microalgae as related to biofuels production", *Curr Opin Chem Biol.*, 17, 506 (2013).

[4] R. H. Wijffels and M. J. Barbosa, "An Outlook on Microalgal Biofuels". *Science*, 329, 796 (2010).

[5] H. Gao et al., "Microalgae as platforms for production of recombinant proteins and valuable compounds: progress and prospects", *J Ind Microbiol Biotechnol.*, 38, 1879 (2011).

[6] J. A. Gregory and S. P. Mayfield, "Developing inexpensive malaria vaccines from plants and algae", *Appl Microbiol Biotechnol.*, 98, 1983 (2014).

[7] J.-S. Chang et al., "Perspectives on microalgal CO_2-emission mitigation systems - A review", *Biotechnol Adv.*, 29, 189 (2011).

[8] E. Molina Grima et al., "Photobioreactors for the production of microalgae", *Rev Environ Sci Bio/Technol.*, 12, 131 (2013).

[9] L. Christenson, R. Sims et al., "Production and harvesting of microalgae for wastewater treatment, biofuels, and bioproducts", *Biotechnol. Adv.*, 29, 686 (2011).

[10] R. H. Wijffels et al., "Potential of industrial biotechnology with cyanobacteria and eukaryotic microalgae", *Curr. Opin. Biotechnol.*, 24, 405 (2013).

[11] H. Mukaibo et al., "Template-synthesized gold microneedle arrays for gene delivery to the Chlamydomonas reinhardtii chloroplast", *Mater. Lett.*, 141, 76 (2015).

[12] D. R. Georgianna and S. P. Mayfield, "Exploiting diversity and synthetic biology for the production of algal biofuels", *Nature*, 488, 329 (2012).

[13] Y. Chisti, "Constraints to commercialization of algal fuels", *J. Biotechnol.*, 167, 201 (2013).

[14] J. Kim et al., "Methods of downstream processing for the production of biodiesel from microalgae", *Biotechnol. Adv.*, 31, 862 (2013).

[15] M. K. Lam and K. T. Lee, "Microalgae biofuels: A critical review of issues, problems and the way forward", *Biotechnol. Adv.*, 30, 673 (2012).

[16] H. C. Greenwell et al., "Placing microalgae on the biofuels priority list: a review of the technological challenges", *J. R. Soc. Interface*, 7, 703 (2010).

[17] A. Schlesinger et al., "Inexpensive non-toxic flocculation of microalgae contradicts theories; overcoming a major hurdle to bulk algal production", *Biotechnol. Adv.*, 30, 1023 (2012).

[18] D. Vandamme et al., "Flocculation as a low-cost method for harvesting microalgae for bulk biomass production", *Trends Biotechnol.*, 31, 233 (2013).

[19] C. Wan et al., "Current progress and future prospect of microalgal biomass harvest using various flocculation technologies", *Bioresour. Technol.*, 184, 251 (2015).

[20] Y.-C. Lee et al., "Recent nanoparticle engineering advances in microalgal cultivation and harvesting processes of biodiesel production: A review", *Bioresour. Technol.*, 184, 63 (2015).

[21] M. Cerff et al., "Harvesting fresh water and marine algae by magnetic separation: Screening of separation parameters and high gradient magnetic filtration", *Bioresour. Technol.*, 118, 289 (2012).

[22] L. Xu et al., "A simple and rapid harvesting method for microalgae by in situ magnetic separation", *Bioresour. Technol.*, 102, 10047 (2011).

[23] S. Ge et al., "Heteroaggregation between PEI-Coated Magnetic Nanoparticles and Algae: Effect of Particle Size on Algal Harvesting Efficiency", *ACS Appl. Mater. Interfaces*, 7, 6102 (2015).

[24] G. Prochazkova et al., "Physicochemical approach to freshwater microalgae harvesting with magnetic particles", *Colloids Surf., B*, 112, 213 (2013).

[25] J. Y. Seo et al., "Effect of barium ferrite particle size on detachment efficiency in magnetophoretic harvesting of oleaginous *Chlorella* sp", *Bioresour. Technol.*, 152, 562 (2014).

[26] S. Ge et al., "Recovering Magnetic Fe_3O_4-ZnO Nanocomposites from Algal Biomass Based on Hydrophobicity Shift under UV Irradiation", *ACS Appl Mater Interfaces*, 7, 11677 (2015).

[27] K. Lee et al., "Magnetic-Nanoflocculant-Assisted Water-Nonpolar Solvent Interface Sieve for Microalgae Harvesting", *ACS Appl. Mater. Interfaces*, 7, 18336 (2015).

[28] E. H. Harris, "The Chlamydomonas sourcebook : a comprehensive guide to biology and laboratory use, first ed", *Academic Press*, San Diego (1989).

[29] W. S. Rasband, ImageJ, U. S. National Institutes of Health. Bethesda, Maryland, USA. http://rsb.info.nih.gov/ij/ (1997-2014).

[30] S. M. Miller et al., "Toward Understanding the Efficacy and Mechanism of *Opuntia* spp. as a Natural Coagulant for Potential Application in Water Treatment", *Environ. Sci. Technol.*,

42, 4274 (2008).

[31] A. Ozkan and H. Berberoglu, "Cell to substratum and cell to cell interactions of microalgae", *Colloids Surf., B*, 112, 302 (2013).

[32] P. Y. Toh et al., "The role of particle-to-cell interactions in dictating nanoparticle aided magnetophoretic separation of microalgal cells", *Nanoscale*, 6, 12838 (2014).

[33] X. Q. Xu, et al., "The colloidal stability and core-shell structure of magnetite nanoparticles coated with alginate", *Appl. Surf. Sci.*, 253, 2158 (2006).

[34] C. Banerjee et al., "Study of algal biomass harvesting through cationic cassia gum, a natural plant based biopolymer", *Bioresour. Technol.*, 151, 6 (2014).

[35] M. Rhodes, "Introduction to Particle Technology", *Wiley*, GB (2013).

[36] I. Rawat et al., "Biodiesel from microalgae: A critical evaluation from laboratory to large scale production", *Appl. Energy*, 103, 444 (2013).

[37] G. Friedman and B. Yellen, "Magnetic separation, manipulation and assembly of solid phase in fluids", *Curr. Opin. Colloid Interface Sci.*, 10, 158 (2005).

[38] J. K. Lim et al., "Rapid Magnetophoretic Separation of Microalgae", *Small*, 8, 1683 (2012).

Chapter 6

General Conclusion

The motivation and results of this thesis are summarized below. The schematic illustration of my approach in this thesis is shown in Fig. 6.1.

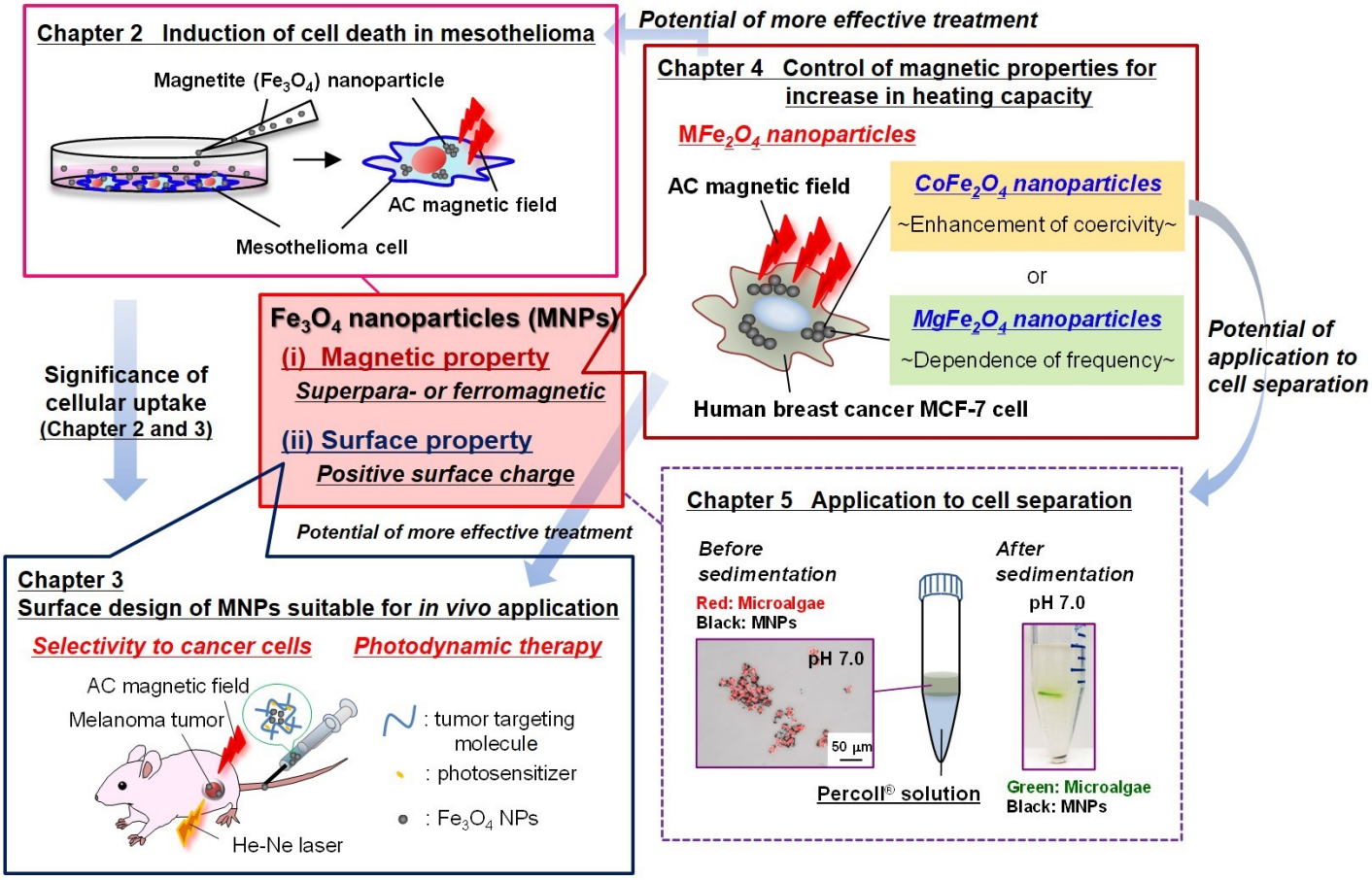

Fig. 6.1 Schematic diagram of this thesis

In chapter 1, the background of this thesis research was described. The objective of this thesis is design of ferrite nanoparticles suitable for magnetic hyperthermia. Iron oxides such as γ-Fe_2O_3

or Fe_3O_4 nanoparticles (MNPs) are used as heat generators as they have the advantages of high biocompatibility and relatively large magnetization but commercially-used particles does not generate sufficient heat for cancer cell death. To overcome the issue, taking advantages of the previous findings of T. Osaka and his group, this thesis focused on two important points in the design of ferrite nanoparticles for effective magnetic hyperthermia. One is to understand the interactions of nanoparticles and cells. The other is to control magnetic and surface properties of nanoparticles. Furthermore, as an example of applications of ferrite nanoparticles, the control of magnetic properties appropriate to cell separation was also discussed in this thesis.

In chapter 2, to understand the effect of nanoparticles on cells, induction of cell death by synthesized MNPs was investigated in mesothelioma cells. Mesothelioma was targeted since there is little effective treatment for mesothelioma. From this chapter, there are three novel findings in the interaction of MNPs and mesothelioma cells, which are that (i) the specific apoptotic effect of MNPs on biphasic mesothelioma MSTO-211H cells was observed without AC magnetic field, (ii) high degree of cell mortality in all three major histological subtypes of mesothelioma was induced with AC magnetic field, and (iii) cellular uptake of MNPs was suggested to be important to induce cell death effectively under AC magnetic field.

In the first of chapter 3, as a part of the approach of understanding the interaction in detail between MNPs and cells, cell damage induced by cellular uptake of MNPs was discussed in human breast cancer cells. In the second of chapter 3, design of surface property of MNPs associated with selectivity to cancer cells and combination with photodynamic therapy for *in vivo* application was discussed. Control of their magnetic property appropriate to the applied condition of AC magnetic field was also considered. As a result, the designed MNPs showed high potential of desirable approach for successful application of MNPs to magnetic hyperthermia, from *in vivo* experiments using melanoma.

In chapter 4, as a design of nanoparticles for effective magnetic hyperthermia, control of magnetic properties of MFe_2O_4 nanoparticles for increase in heating efficacy was focused. Synthesis and characterization of $CoFe_2O_4$ and $MgFe_2O_4$ nanoparticles was examined. Through

the comparison of heating efficacy of each ferrite nanoparticles, the significance of showing larger magnetization and larger coercivity in the range of applied magnetic field was suggested. Furthermore, the *in vitro* evaluation of interactions between $CoFe_2O_4$ and $MgFe_2O_4$ nanoparticles and breast cancer cells was discussed. Although many factors such as cellular uptake and biocompatibility were also involved for achieving effective magnetic hyperthermia, the control of the occupation of the A- and B-sites by transition metal cations (M^{2+} and Fe^{3+}) in spinel structure should be a key for further design in future.

In chapter 5, for practical use of microalgae which produce biofuels, sedimentation-induced detachment of MNPs from microalgal flocs using a dense/viscous solution (Percoll®) was discussed. Through this study, ferromagnetic ferrite nanoparticles synthesized in this thesis was suggested to have high potential for applying to cell separation technology.

Through all chapters, the significance of control of magnetic and surface properties of ferrite nanoparticles for their successful bio-application was examined and discussed. Especially, controlling of magnetic properties of ferrite nanoparticles appropriate to the applied condition of AC magnetic field and evaluation of the effect of nanoparticles on cells were focused. As a result, design of ferrite nanoparticles with considering (1) showing larger magnetization and larger coercivity in the range of applied magnetic field, (2) combination with other effects such as specific-cytotoxicity and photodynamic therapy, and (3) increase in cellular uptake specific to cancer cells, will help to achieve effective magnetic hyperthermia in future.

Considering to the association of each chapters of this thesis as shown in Fig. 6.1, the study of their combination is very interesting. As future works, mesothelioma and melanoma therapy using MFe_2O_4 nanoparticles with larger magnetization and larger coercivity in the range of applied magnetic field are ones of candidates.

List of Achievements

1. Original articles

Sedimentation-induced detachment of magnetite nanoparticles from microalgal flocs
Bioresource Technology, **200**, 914-920, (2016)
S. Matsuda, A. R. Durney, L. He, H. Mukaibo

Induction of cell death in mesothelioma cells by magnetite nanoparticles
ACS Biomaterials Science & Engineering, **1**, 632-638, (2015)
S. Matsuda, A. Hitsuji, T. Nakanishi, H. Zhang, A. Tanaka, H. Matsuda, T. Osaka

Synthesis of cobalt ferrite nanoparticles using spermine and their effect on death in human breast cancer cells under an alternating magnetic field
Electrochimica Acta, **183**, 153-159, (2015)
S. Matsuda, T. Nakanishi, K. Kaneko, T. Osaka

Stimuli-responsive magnetic nanoparticles for tumor-targeted bimodal imaging and photodynamic/hyperthermia combination therapy
Nanoscale, **8**, 11625-11634, (2016)
K. S. Kim, J. Y. Kim, J. Y. Lee, S. Matsuda, S. Hideshima, Y. Mori, T. Osaka, K. Na

2. International conferences

Effect of heating with magnetite nanoparticles on death of human breast cancer MCF-7 cells
3rd *DGIST-WASEDA Workshop on Electrochemistry*, Tokyo, Japan, (December 2015)
K. Kaneko, S. Matsuda, T. Nakanishi, H. Zhang, T. Osaka

Cytotoxic effect of magnetite nanoparticles on mesothelioma cells
The 6th NIMS/MANA-Waseda University International Symposium, Tokyo, Japan, (July 2015)
S. Matsuda, T. Nakanishi, E. Nakajima, H. Zhang, A. Tanaka, H. Matsuda, T. Osaka

Effect of heating with magnetite nanoparticles outside and inside of cells on death of human breast cancer MCF-7 cells
Conference for BioSignal and Medicine 2015 (CBSM2015), Fukushima, Japan, (July 2015)
K. Kaneko, S. Matsuda, T. Nakanishi, E. Nakajima, H. Zhang, T. Osaka

Synthesis and characterization of $CoFe_2O_4$ nanoparticles for application to magnetic hyperthermia
10th International Symposium on Electrochemical Micro & Nanosystem Technology, Okinawa, Japan, (November 2014)
S. Matsuda, T. Nakanishi, T. Osaka

Comparison of heat generation between $CoFe_2O_4$ and Fe_3O_4 nanoparticles under AC magnetic field
2nd *DGIST-WASEDA Workshop on Electrochemistry*, Deagu, Korea, (August 2014)
S. Matsuda, T. Nakanishi, T. Osaka

Cytotoxicity of magnetite nanoparticles on mesothelioma cells
The 6th International Workshop on Advanced Electrochemical Power Sources, Tianjin, China, (December 2013)
S. Matsuda, T. Nakanishi, H. Zhang, A. Tanaka, H. Matsuda, T. Osaka

Cellular Uptake of Magnetite Nanoparticles and Induction of Cell Death in Mesothelioma Cells
*The 64th Annual Meeting of the International Society of Electrochemistr*y, Querétaro, Mexico, (September 2013)
S. Matsuda, T. Nakanishi, H. Zhang, A. Tanaka, H. Matsuda, T. Osaka

Induction of Cell Death and Uptake in Mesothelioma Cells by Magnetite Nanoparticles
The 11th International Conference on Ferrites (ICF-11), Okinawa, Japan, (April 2013)
S. Matsuda, H. Zhang, T. Nakanishi, A. Tanaka, H. Matsuda, T. Osaka

3. Domestic conferences

上皮型及び混合型中皮腫細胞にマグネタイトナノ粒子の取り込みと交流磁場印加が及ぼす影響
第 38 回日本分子生物学会年会，神戸，2015 年 12 月
中嶋恵里，松田翔風，中西卓也，張弘，田中あかね，松田浩珍，逢坂哲彌

細胞内および細胞外に存在するマグネタイト粒子の発熱がヒト乳がん細胞に与える死滅効果
第 38 回日本分子生物学会年会，神戸，2015 年 12 月
金子恭彩子，松田翔風，中西卓也，張弘，逢坂哲彌

マグネタイトナノ粒子を取り込んだ中皮腫細胞への交流磁場照射が細胞死に与える影響
第 37 回日本分子生物学会年会，横浜，2014 年 11 月
日辻愛理，松田翔風，中西卓也，張弘，逢坂哲彌

マグネタイトナノ粒子の発熱がヒト乳がん細胞 MCF-7 の生存率に及ぼす影響の *in vitro* 評価
第 37 回日本分子生物学会年会，横浜，2014 年 11 月
金子恭彩子，松田翔風，中西卓也，張弘，逢坂哲彌

マグネタイトナノ粒子の中皮腫細胞への取り込みとその発熱による細胞死の評価
第 36 回日本分子生物学会年会，神戸，2013 年 12 月
日辻愛理，松田翔風，中西卓也，張弘，田中あかね，松田浩珍，逢坂哲彌

中皮腫細胞に対するマグネタイトナノ粒子のアポトーシス効果
12th Conference for BioSignal and Medicine (CBSM) 2013，山梨，2013 年 7 月
松田翔風，中西卓也，張弘，田中あかね，松田浩珍，逢坂哲彌

マグネタイトナノ粒子の中皮腫細胞への取り込みとその交流磁場下での発熱による細胞死滅効果
12th Conference for BioSignal and Medicine (CBSM) 2013，山梨，2013 年 7 月
日辻愛理，松田翔風，中西卓也，張弘，田中あかね，松田浩珍，逢坂哲彌

中皮腫細胞へのマグネタイトナノ粒子の取り込みとその交流磁場下での発熱による細胞死の評価
電気化学会第 80 回大会，宮城，2013 年 3 月
日辻愛理，松田翔風，中西卓也，張弘，田中あかね，松田浩珍，逢坂哲彌

中皮腫細胞へのマグネタイトナノ粒子の取り込みと細胞毒性作用
第 35 回日本分子生物学会年会，博多，2012 年 12 月
松田翔風，張弘，中西卓也，田中あかね，松田浩珍，逢坂哲彌

マグネタイトナノ粒子の中皮腫細胞への取り込み及び殺傷効果の評価
電気化学会第 79 回大会，浜松，2012 年 3 月
松田翔風，馬場大輔，張弘，中西卓也，田中あかね，松田浩珍，逢坂哲彌

4. Award

ICF 11 Yamazaki Yohtaro Memorial Student Award
The 11th International Conference on Ferrites (ICF-11), Okinawa, Japan, (April 2013)
S. Matsuda

Key Bioenergy Article
Renewable Energy Global Innovations, (May 2016)
https://reginnovations.org
“Sedimentation-induced detachment of magnetite nanoparticles from microalgal flocs”
S. Matsuda, A. R. Durney, L. He, H. Mukaibo

Acknowledgments

I wish to extend my sincere appreciation to Prof. Tetsuya Osaka and Prof. Toshiyuki Momma for giving me an environment to do the research of ferrite nanoparticles for application to magnetic hyperthermia. I am appreciative to Prof. Toru Asahi, Prof. Takayuki Homma, Prof. Takuya Nakanishi, Prof. Yoshinori Nishikitani, and Prof. Kazuaki Utsumi for the referee of my thesis and giving me valuable advices to improve the thesis. Also Prof. Nakanishi always gave me many advices on my research and taught me how to give a presentation and how to make a document. Thank you totally for his supports.

I would like to express my appreciation to Assistant Prof. Hitomi Mukaibo in University of Rochester for giving me an opportunity to do the research of application of ferrite nanoparticles to cell-separation technology.

I would like to acknowledge Prof. Hiroshi Matsuda and Prof. Akane Tanaka in Tokyo University of Agriculture and Technology for their useful discussion and advices on my research. I also acknowledge Prof. Kun Na group in Catholic University of Korea for our collaboration research.

I deeply thanks to Prof. Keishi Ohashi, Prof. Yasurou Mori, Prof. Hong Zhang, Associate Prof. Shigeki Kuroiwa, Dr. Sho Hideshima, Mr. Daisuke Baba, Ms. Chigusa Shundo, Mr. Yasuhiro Seiko, Ms. Nanako Tsutsui, Ms. Airi Hitsuji, Ms. Rina Noguchi, Ms. Kisako Kaneko, Ms. Eri Nakajima, Mr. Kodai Miyazaki, Ms. Maho Kanazu, and Ms. Yuka Kashimata for their help and assistance on my research.

I am grateful to all members in the Applied Physical Chemistry Laboratory in Waseda University.

I would like to acknowledge the Leading Graduate Program in Science and Engineering in Waseda University for giving me many valuable experiences.

Acknowledgments

Finally, I am deeply appreciative of my family for their support to concentrate on my research. Thank you very much totally for their cooperation.

June, 2016

Shofu Matsuda